

**Thermal and Flow Characteristics of an
Electrohydrodynamically Enhanced
Capillary Evaporator**

Thermal and flow characteristics of an electrohydrodynamically enhanced capillary evaporator

By

Behrooz Komeili, B.Eng. (Electrical Engineering- McMaster University)

A Thesis Submitted to the School of Graduate Studies
in Partial Fulfilment of the Requirements
for the Degree
Masters of Applied Science in Engineering Physics

McMaster University
Hamilton, Ontario, Canada

© Copyright by
Behrooz Komeili, 2007

MASTER OF APPLIED SCIENCE (2007)
(Engineering Physics)

McMASTER UNIVERSITY
Hamilton, Ontario, Canada

TITLE: Thermal and flow characteristics of an
electrohydrodynamically enhanced capillary evaporator

AUTHOR: Behrooz Komeili

SUPERVISORS: Dr. J-S Chang and Dr. Glenn Harvel

NUMBER OF PAGES: xiv, 121

ABSTRACT

Experimental investigations have been conducted for an Electrohydrodynamically enhanced capillary evaporator (EHD-ECE) for enhancement of liquid evaporation, hence the flow rate. A capillary evaporator has a liquid channel inlet and a vapour channel exit. Inside the evaporator is a porous media that separates the liquid and vapour, which is also responsible for the capillary action. When an external electric field is applied inside the liquid side of the evaporator, the capillary action may be enhanced due to external body forces. Voltage was applied to the 3.1mm electrode, in the centre axis of the evaporator liquid channel. The environmentally friendly HFC-134a is used as the working fluid. The coaxial cylindrical evaporator centre is liquid filled and surrounded by a porous polyethylene wick, where the vapour channels are located on the other side of the wick. Heat is applied to the outer diameter of the evaporator. Experiments were conducted for applied heat loads from 0 to 80W and applied electric fields of dc voltages from 0 to -5kV and 5kV, as well as frequencies ranging from 5-200Hz with applied pulse voltages of -10kV and 5kV. Thermal temperatures of the liquid inlet, vapour exit, and evaporator wall, pressure difference across the evaporator, system pressure and liquid flow rates are measured and analysed.

The experimental results show that the vapour flow rate increases with increasing applied voltages and enhancement up to a maximum of 202% was achieved when 5kV dc was applied with a heat input of 80W. The polarity of the applied voltage had only a slight effect as slightly higher flow rate enhancements were observed. The vapour flow

rate was also enhanced for applied pulse voltage, where the vapour flow rate increased with increasing frequencies between 50Hz to 200Hz.

With the application of dc and pulsed electric fields, the vapour flow rate due to the external body forces acting on the liquid-vapour interface are enhanced. Future work is required to fully understand the phenomena and more optimization studies are required for the EHD-CPL.

Acknowledgements

The author would like to express his sincere gratitude to Dr. J-S Chang and Dr. G.D. Harvel for their guidance, support and patience throughout this work. The author deeply appreciates their tireless reading of many drafts and their valuable input to this thesis.

I am also grateful for the help and support of Drazena Brocilo, Anas Khaial, Cécile Ayrault, Steve Shelestynsky, Dr. Tsubone, Dr. C.Y. Ching and Dr. Ewing with whom I have had many helpful discussions in the stages of my work. Thank you Bontadi for teaching me about *life-smarts*.

Thanks to all my friends that I have not been able to see as much but have still stuck by me through this time; especially Rihard and Tom.

Mom and dad, thank you for your love, support and interest. I will always be grateful for all that you have done for me. Amir and Armin, I have always looked up to the both of you and I am truly grateful to have you both. You all believed in me and I am truly lucky to have you.

Finally I would like to thank Rund for her continuing support, encouragement and patience throughout my complete studies; I truly believe that this would not be possible without you. You have been my motivator and more importantly you have been my best friend. You inspire me to be great and I dedicate this to you.

Nomenclature

A = Surface area

B = Magnetic flux

C_p = Heat capacity

D = Diffusion coefficient

E = Electric field

e = Elementary charge

F = Force

g = Gravitational constant

H = Magnetic field strength

I = Current

κ = Boltzmann constant or thermal conductivity

L = Characteristic length

N = Number density

P = Pressure

T = Temperature

t = Time

U = Velocity

V = Voltage

ρ = Density

ν = Kinematic viscosity

μ_i = Mobility

μ_g = Viscosity

ϵ_s = Dielectric constant ($\epsilon_s = \epsilon / \epsilon_0$)

ϵ_o = permittivity of free charge

($\epsilon_o = 8.854 \times 10^{-12} \text{ N/V}^2$)

λ_D = Debye length

β = Thermal expansion coefficient

Subscripts

e = electron

f = fluid

i = ion

s = reference value

T = temperature

$+$ = positive ions

$-$ = negative ions

Other symbols are defined in text

Table of Contents

Abstract	iii
Acknowledgements	v
Nomenclatures	vi
List of tables	x
List of figures	xi
Chapter 1 Introduction	1
1.1 Thermal and fluid managements of electronics and electric apparatus	1
1.2 Heat transfer enhancement method.....	2
1.2.1 EHD fluid flow	4
1.2.2 Electrohydrodynamically enhanced heat transfer	5
1.3 Objective of this work.....	6
Chapter 2 Literature Review	7
2.1 Natural circulation and capillary pump loops	7
2.2 Capillary evaporator.....	9
2.3 EHD pumps.....	11
2.3.1 Single-Phase Flow Ion Drag and Pure Conduction Pump	12
2.3.2 Single Phase Induction Pump	13
2.3.3 Two-Phase Flow Traveling Wave Dielectrophoretic Pump	14
2.3.4 EHD Two-Phase Capillary Pump	15
Chapter 3 Electrohydrodynamic Flow	19
3.1 Electrohydrodynamic	19
3.2 Conservation equations for EHD single-phase flow.....	20
3.3 Single-phase gas and liquid EHD flow	24
3.4 EHD in liquid-vapour interface	28

Chapter 6	Conclusions and Recommendations	84
	6.1 Conclusions.....	84
	6.2 Recommendations.....	87
References		88
Appendix A		93
	A.1 Transit time thermal, pressure difference, system pressure liquid and liquid reservoir characteristics of capillary pump without condensate collection tank water cooling	93
	A.2 Transit time thermal, pressure difference, system pressure liquid and liquid reservoir characteristics of capillary pump with condensate collection tank water cooling	97
	A.3 Transit time thermal, pressure difference, system pressure liquid and liquid reservoir characteristics of capillary pump with condensate collection tank water cooling with dc voltage	101
	A.4 Transit time thermal, pressure difference, system pressure liquid and liquid reservoir characteristics of capillary pump with condensate collection tank water cooling with pulse voltage with frequency range 50-200Hz	105
Appendix B		109
	B.1: Current-voltage characteristics applied dc voltage	111
	B.2: Typical pulse waveform for EHD-ECE	112
Appendix C		114
	C.1: Modelling of electric field inside the CE and evaluation of dimensionless parameters	119

LIST OF TABLES

Table 2-1: Review of EHD pump research (after Shelestynsky, 2007).....	17
Table 2-2: Review of EHD pump research continued.	18
Table 3-1: Relative Importance of EHD terms (Chang, 1998).....	23
Table 4-1: Test matrix for the EHD-ECE experiment.	53

LIST OF FIGURES

Figure 1-1: a) Schematic of a generic capillary pumped loop and b) Cross-section of the evaporator redrawn from a) (Cao and Faghri, 1994) and b) (Shelestynsky, 2007)	3
Figure 2-1: Pressure losses in the capillary pump redrawn from Wulz and Mayinger (1993) where $q =$ Heat flux.....	11
Figure 3-1: Electroconvective motion of carbon tetrachloride and kerosene mixture with polyethylene particles, 5kV dc field redrawn from (Peters, et. al. 1980a) ...	20
Figure 3-2: EHD instability on the vapour-liquid interface for a) stratified vapour-liquid b) stratified liquid-vapour c) droplets and d) bubble under wire-plate electrodes	30
Figure 4-1: Schematic of test loop and location of measurement instruments $T_{inlet}, T_{wall}, T_{exit}$: Thermocouples, dP: Pressure transducer, P: Pressure gage ST: Sight tube	32
Figure 4-2: EHD-ECE test layout.....	34
Figure 4-3: Schematic of experimental evaporator.....	35
Figure 4-4: Schematic of EHD enhanced capillary evaporator with high voltage electrode	35
Figure 4-5: Condensate collection tank.	38
Figure 4-6: Ultrasonic Panametric instrumentation a) Pulser receiver and b) 10MHz ultrasonic transducer	42
Figure 4-7: Typical ultrasonic waveform signal analysis a) raw signal b) rectified signal and c) envelope signal.....	42
Figure 4-8: Glassman high voltage for dc applications	44
Figure 4-9: Schematic of 555-timer type pulse power supply.....	44
Figure 4-10: Schematic of the MOSFET driven type pulse power supply.....	44
Figure 4-11: Typical power loss and heat generation across the MOSFET due to switching losses	46
Figure 4-12: EHD gas pump used to test pulse power supply.....	46
Figure 4-13: Schematic of EHD gas pump.....	46

Figure 4-14: Effect of polarity on central axis velocity at the pump exit with applied power for $L=12.6$, $D=20\text{mm}$, $D_g=3.1\text{mm}$ and $d_w=0.24\text{mm}$ for dc case	49
Figure 4-15: Primary and secondary side waveforms of the 555-timer circuit under 20Hz frequency.....	49
Figure 4-16: Primary and secondary side waveforms of the MOSFET driven circuit for 20Hz frequency	50
Figure 4-17: Efficiency test with respect to frequency for the two comparing pulse power supplies	51
Figure 5-1: Typical transient behavior of liquid, vapour, wall-temperature and pressure difference/ECE device for EHD-ECE for no water cooling on condensate collection tank for heat input= 40W at $V=0$	57
Figure 5-2: Steady state liquid, vapour and wall-temperature for EHD-ECE for no water cooling on condensate collection tank as a function of heat inputs at $V=0$. ..	57
Figure 5-3: Steady state pressure difference, liquid flow rate and system pressure measurements for EHD-ECE for no water cooling on condensate collection tank as a function of heat inputs at $V=0$	58
Figure 5-4: Steady state vapour flow rate measurements for EHD-ECE for no water cooling on condensate collection tank as a function of heat inputs at $V=0$. ..	58
Figure 5-5: Typical transient behavior of liquid, vapour, wall-temperature and pressure difference/ECE device for EHD-ECE for water cooling on condensate collection tank for heat input= 40W at $V=0$	62
Figure 5-6: Steady state liquid, vapour and wall-temperature for EHD-ECE for water cooling on condensate collection tank as a function of heat inputs at $V=0$. ..	62
Figure 5-7: Steady state pressure difference, liquid flow rate and system pressure measurements for EHD-ECE for water cooling on condensate collection tank as a function of heat inputs at $V=0$	63
Figure 5-8: Steady state vapour flow rate measurements for EHD-ECE for water cooling on condensate collection tank as a function of heat inputs at $V=0$	63
Figure 5-9: Typical transient behavior of liquid, vapour, wall-temperature and pressure difference for EHD-ECE for water cooling on condensate collection tank for heat input= 60W at dc voltage applied	67
Figure 5-10: Typical variation in behavior of liquid flow rate averaged over 5 mm for EHD-ECE for water cooling on condensate collection tank for heat input= 60W at dc voltage applied	67

Figure 5-11: Steady state liquid, vapour and wall-temperature for EHD-ECE for water cooling on condensate collection tank as a function of heat inputs at V= -2.5kV. The room temperature was 20-22°C and inlet cooling water 15-16°C..	68
Figure 5-12: Steady state pressure difference, liquid flow rate and system pressure measurements for EHD-ECE for water cooling on condensate collection tank as a function of heat inputs at V=-2.5kV	69
Figure 5-13: Average flow rate in ECE with water cooling on condensate collection tank for various heat inputs comparing -2.5kV applied voltage and 0V. The room Temperature was 20°C-23°C and cooling water average temperature was 14°C-16.5°C.	70
Figure 5-14: Steady state liquid, vapour and wall-temperature for EHD-ECE for water cooling on condensate collection tank as a function of heat inputs at V= -5kV. The room temperature was 20-23°C and inlet cooling water 14-16.5°C.	70
Figure 5-15: Steady state pressure difference, liquid flow rate and system pressure measurements for EHD-ECE for water cooling on condensate collection tank as a function of heat inputs at V=-5kV	71
Figure 5-16: Average flow rate in ECE with water cooling on condensate collection tank for various heat inputs comparing -5kV applied voltage and 0V. The room average temperature was 20°C-23°C, and average cooling water temperature=14°C-16.5°C	72
Figure 5-17: Steady state liquid, vapour, wall-temperature for EHD-ECE for water cooling on condensate collection tank as a function of heat inputs at V= 5kV. The room temperature was 20-22°C and inlet cooling water 15-16°C.	72
Figure 5-18: Steady state pressure difference, liquid flow rate and system pressure measurements for EHD-ECE with water cooling on condensate collection tank for various heat inputs comparing 5kV applied voltage and 0V. The room average temperature was 20°C-23°C, and average cooling water temperature was 14°C-16.5°C	73
Figure 5-19: Average flow rate in ECE with water cooling on condensate collection tank for various heat inputs comparing 5kV applied voltage and 0V. The room average temperature was 20°C-23°C, and average cooling water temperature was 14°C- 16.5°C	74
Figure 5-20: Vapour flow rate enhancement percentage in ECE with water cooling condensate collection tank for various heat inputs comparing applied voltages	74

Figure 5-21: Typical transient behavior of liquid, vapour, wall-temperature and pressure difference for EHD-ECE for water cooling on condensate collection tank for heat input=40W	77
Figure 5-22: Steady state liquid, vapour and wall-temperature for EHD-ECE for water cooling on condensate collection tank as a function of heat inputs at V= -10kV for various frequencies of 5Hz, 50Hz and 200Hz. The average room temperature was 20-22°C and inlet cooling water 10-12.5°C.	77
Figure 5-23: Steady state pressure difference, liquid flow rate and system pressure measurements for EHD-ECE for water cooling on condensate collection tank as a function of heat inputs at V= -10kV for various frequencies of 5Hz, 50Hz and 200Hz. . The average room temperature was 20-22°C and inlet cooling water 10-12.5°C.	78
Figure 5-24: Average flow rate in EHD-ECE for water cooling on condensate collection tank as a function of heat inputs at V= -10kV for various frequencies of 5Hz, 50Hz and 200Hz. . The average room temperature was 20-22°C and inlet cooling water 10-12.5°C.	79
Figure 5-25: Steady state liquid, vapour and wall-temperature for EHD-ECE for water cooling on condensate collection tank as a function of heat inputs at V= 5kV for various frequencies of 5Hz, 50Hz and 200Hz. The average room temperature was 20-22°C and inlet cooling water 10-12.5°C	80
Figure 5-26: Steady state pressure difference, liquid flow rate and system pressure measurements for EHD-ECE for water cooling on condensate collection tank as a function of heat inputs at V= 5kV for various frequencies of 5Hz, 50Hz and 200Hz. . The average room temperature was 20-22°C and inlet cooling water 10-12.5°C	81
Figure 5-27: Average flow rate in EHD-ECE for water cooling on condensate collection tank as a function of heat inputs at V= 5kV for various frequencies of 5Hz, 50Hz and 200Hz. . The average room temperature was 20-22°C and inlet cooling water 10-12.5°C.	82
Figure 5-28: Vapour presence at the wick-fin interface.	83

Chapter 1

INTRODUCTION

1.1 Thermal and Fluid Managements of Electronics and Electric Apparatus

When the density of electronic circuits increases in electronic and electric equipment; a more effective method for thermal management and packaging are required. This need arises not only in the context of high speed computers but also, for example, in the next generation of portable/mobile electronics, biomedical devices, and automotive applications, etc.

Cooling systems for electronic equipment are becoming more important as the surface heat fluxes of bipolar chips are projected to reach 10^3 W/cm^2 by 2010 (Pollack, 1999), which is one order of magnitude less than the heat flux on the surface of the sun. For another comparison purpose, a steam iron has a heat flux of 5 W/cm^2 (Chu, 2003). Cooling technologies using single-phase natural and forced convection is limited by a heat transfer coefficient of less than $1 \text{ W/cm}^2\text{C}$ (Chu, 2003). Hence, currently two-phase systems are actively being used in many applications such as spacecrafts, where space is at a premium and heat is generated in confined areas. One such method of heat removal, which will be discussed in the latter sections, is by Capillary Pumped Loops (CPL). This method has demonstrated heat transport capabilities ranging up to 25kW over a distance of 10 meters, (Butler and McIntosh, 1990), while keeping the size of the CPL to only $0.36 \times 0.36 \times 0.10 \text{ m}^3$.

1.2 Heat transfer enhancement for CPL

The evolution of heat transfer enhancement technology in the past half century has been readily observed by the level of activity in the technical literature as well as patent literature as shown by Webb et. al. (1983b) and Bergles et. al. (1991).

There are numerous different methods of both active and passive enhanced heat transport methods as discussed by Webb (1994), however the two of interest to the scope of this work will be briefly discussed;

Passive methods

Surface tension devices use surface tension forces created by the wicking or grooving surfaces to direct flow of liquid in boiling and condensation. Heat pipes often use the capillary wicking to transport liquid from the condenser to the evaporator.

The subject of heat transfer enhancement has been an active topic in order to increase the efficiency of current heat exchanging devices; CPL systems are one method of heat transport. CPLs involve two-phase capillary driven heat pipes (HP) and loop heat pipes (LHP) and are operated by capillary forces generated on a porous material in the evaporator. For space applications, where the absence of gravity is now a factor, the desired method of enhanced heat exchangers is limited to the method of capillary action (Stenger, 1966) or electrohydrodynamic actions (Shelestynsky, 2007).

An example of a typical CPL system is shown in Figure 1.1a) and consists of an evaporator, a condenser, a two-phase reservoir and connecting plumbing. The evaporator design is crucial and a cross-section of the capillary evaporator is shown in Figure 1.1b), more details of the evaporator will be given in the latter chapters.

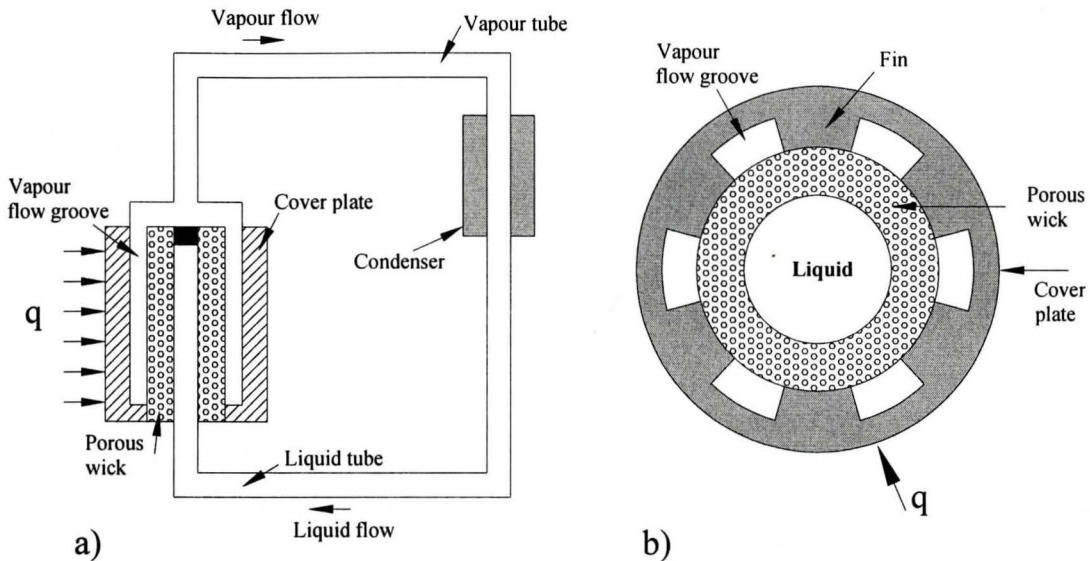


Figure 1.1: a) Schematic of a generic capillary pumped loop and b) Cross-section of the evaporator redrawn from a) (Cao and Faghri, 1994) and b) (Shelestynsky, 2007)

In CPLs, the heat is transferred at the evaporator through a fin structure to a porous media saturated with a working fluid that is supplied from a liquid reservoir. The vapour generated at the evaporator then travels through the vapour line to a condenser where the latent heat is then released. The liquid is returned to the evaporator by the capillary action at the wick in the evaporator. In conventional heat pipes the wick is present over the entire length and the vapour flow from the evaporator to the condenser is counter-current to the liquid flow.

CPLs have separated vapour and liquid flow, which allow the vapour to be slightly superheated and the liquid to be subcooled which increases the transport capacity of the system due to the absence of liquid and vapour counterflow. In addition to this, having a wickless transport line also provides a greater heat-transport distance as well as more flexibility of installation compared to that of HPs (Mo et. al., 2000).

Active methods

Electrostatic fields are applied to both single and two-phase dielectric fluid flow to add a secondary motion in the fluid to increase bulk mixing and disturb the thermal boundary layer near the surface. The electric field may also create forced convection through electrohydrodynamic (EHD) pumping.

The addition of EHD has advantages for heat transfer enhancement as well as reducing costs, reducing pumping requirements and possibly increasing the flow rate of the fluid transport as will be discussed further in sections 1.2.1 and 1.2.2.

1.2.1 EHD fluid flow

Electrohydrodynamic (EHD) pumping is generated by the interaction of electrical fields and free charges in a dielectric fluid medium. Pumping is produced when electrical fields drag charges through the fluid in a given direction. Therefore, the EHD pumping has two basic requirements. First, the dielectric fluid must contain free charges. Second, electrical fields must be present to interact with the free charges in the fluid medium.

One method of creating free charges in the dielectric fluid is based on the establishment of an electrical conductivity gradient perpendicular to the desired direction of fluid motion, giving an induction EHD pump. In the induction EHD pump, the charges in the fluid come from dissociation of molecules into positive and negative ions. As a result, the net electrical charge is zero when averaged over the entire pump; there are local regions of positive or negative charge, however, that tend to return to equilibrium in an amount of time on the order of the electrical relaxation time of the liquid. This differs

from the ion-drag pump, which will be discussed in chapter two and has a net charge imbalance caused by injection of carriers from an electrode.

1.2.2 Electrohydrodynamically enhanced heat transfer

The concept of electrohydrodynamic enhancement of heat transfer rates was first discussed by Chubb (1916) on liquid heating improvement methods and apparatus. The subject of EHD for this purpose did not however receive much practice until after the 1980's where more work was done to design practical heat exchangers.

Enhancement of single-phase forced convective heat transfer using various dielectric fluids such as transformer oil, silicon oil, hexane, aviation fuel and air were all experimented with early on. Some significant enhancements are reported, up to a few thousand percent, with minor pressure drop penalties (Fernandez and Poulter, 1987). However enhancement rarely occurs much above the laminar regime, as the induced secondary flow becomes negligible compared to the strength of the turbulent eddies. Therefore the focus has shifted to applications relating to phase change since the electrical properties of the liquid and vapour phase of the dielectric fluid can be significantly different. Meaning that the application of an electric field in two-phase applications can contribute additional body forces not present in single-phase applications. Both experimental and theoretical research has shown that these forces may lead to a reduction in the thermal boundary layer thickness, increased convection, enhanced boiling dynamics, interfacial instabilities or phase migration that can result in flow pattern redistribution. (Cotton, 2005)

1.3 Objective of this work

The purpose of this work is to investigate enhancement to the flow rate and hence the heat transfer in an electrohydrodynamic enhanced capillary evaporator (EHD-ECE) with applied voltage. A secondary objective is to study flow rate enhancement due to various parameters of dc voltage as well as pulse applied voltage.

A pulse power supply is necessary to generate a stable and reproducible pulsed voltage based on a precision trigger pulse circuit and an ignition coil driven by low voltage dc power supply. Modifications of a conventional ignition coil type high voltage pulse power supply will be made in order to increase the power supply efficiency. This is achieved by load impedance matching as well as increasing the switching time over the MOSFET in order to increase the rise and fall time of the generated pulse.

This thesis consists of six chapters. A literature review is given in chapter two, which discusses natural circulation and conventional CPLs as well as the importance of the evaporator. Chapter three provides the theory regarding the addition of EHD to single and two-phase flow that will be helpful in understanding the current work. The details of the experimental approach as well as the experiment procedure are given in chapter four. The results and discussions of the experiment are given in chapter five and finally the conclusion and recommendation is given in chapter six.

Chapter 2

LITERATURE REVIEW

This chapter will review the understanding of capillary pumped loops and the effect of natural circulation without capillary action. The capillary evaporator is the most crucial device in the experiment and will require a detail discussion since the capillary forces occur in this section, which is responsible for the pumping of the fluid. A better understanding of the EHD-enhanced capillary evaporator (ECE) will be required through a brief review of different EHD pumps, with different pump types, electrode design, and flow regimes.

2.1 Natural circulation and capillary pumped loops

Most materials that are fluid at common temperatures expand when they are heated, becoming less dense. Correspondingly, they become denser when they are cooled. At the heat source of a system of natural circulation, the heated fluid becomes lighter than the fluid surrounding it, and thus rises. At the heat sink, the nearby fluid becomes denser as it cools, and is drawn downward by gravity. Together, these effects create a flow of fluid from the heat source to the heat sink and back again.

In a single-phase natural circulation loop (NCL), the circulating fluid removes heat from a source and transports it to a heat sink, the circulation being the result of the buoyancy force caused by the thermally induced density difference in a body force field (Vijayan, 2002). The circulation is passive in nature and can continue as long as the heat

source and heat sink are maintained without the use of any moving parts. Due to this fact, NCLs can be applicable in many industrial fields. Notable among these are nuclear reactor core cooling, transformer cooling, solar water heaters, gas turbine blade cooling, computer cooling, etc. In both Vijayan (2002) and Zvirin (1981) the steady state behavior of uniform and non-uniform diameter loops was expressed by a non-dimensional parameter for single-phase and showed a flow rate correlated with applied heat load as a power law ($Q \propto W^n$) with $\frac{1}{3} < n < \frac{1}{2}$. However two-phase NCLs are more complex as shown by Jeng and Pan (1999) as they actually have flow reversal at higher heat loads under certain system pressures.

The first work of CPLs was proposed by Stenger (1966) in order to transport heat over large distances. The working principal of a CPL discussed by Wulz and Mayinger (1993) is as follows;

1. The capillary pump contains a porous wick in which the subcooled working fluid is stored. Heat is produced and flows to the surface of the porous wick;
2. This heat evaporates the working fluid and releases vapour into the vapour channel line;
3. The vapour travels through the vapour line and transports the heat to the condenser;
4. The vapour condenses and the heat of condensation is rejected from the system;
5. The subcooled working fluid travels back via the liquid line and enters the wick again to repeat the same process.

2.2 Capillary evaporator

At steady state the capillary effective pumping pressure developed by the evaporator and the pressure drop in the loop are in equilibrium. To be able to drive the system the pressure generation through capillary action in the evaporator must overcome the pressure losses in the rest of the loop as discussed by Shelestynsky (2007).

Heat flux is applied through the fin to the wick and the liquid as shown in Figure 1.1b). The applied thermal loading to the wick causes evaporation at the wick surface and the formation of a meniscus at the interface. The capillary force due to the meniscus drives the liquid flow in the wick and is the driving force of the CPL. The working fluid flows through the wick and evaporates at the outer surface. The pressure generated by the capillary force drives the vapour through the grooves between the fins downstream to the condenser.

Another method of characterizing the performance of a CPL is through thermal analysis. Plots of heat flux versus superheats or temperature difference across the system will yield a heat transfer coefficient, which is the effectiveness of the system to remove heat. It is possible by a similar analysis to be able to analyze thermal resistances between the evaporator and the condenser and the heat input q is determined by Shelestynsky (2007);

$$q = \frac{T_{wall}^{evap} - T_{wall}^{cond}}{R_T} \quad 2.1$$

, and
$$R_T = R_{wall}^{evap} + R_{wick}^{evap} + R_{vapour} + R_{wall}^{cond} \quad 2.2$$

, where q is the heat input (W), T_{wall}^{evap} is the temperature of the evaporator wall, T_{wall}^{cond} is the temperature at the condenser wall, R_{wall}^{evap} is the capillary evaporator thermal resistance, R_{wick}^{evap} is the wick thermal resistance in the evaporator, R_{vapour} is the vapour line thermal resistance, and R_{wall}^{cond} is the condenser thermal resistance.

This is the sum of the thermal resistances for the heat transfer process between the evaporator wall and the condenser wall. The largest resistance will determine the maximum heat transported by the loop and is typically R_{vapour} , which is the superheating of the vapour as discussed by Shelestynsky (2007).

The maximum pressure developed by the evaporator is given by Cao and Faghri (1994) and Wulz and Mayinger (1993);

$$\Delta P_{evp} = \frac{2\sigma \cos \theta}{r_{eff}} - \Delta P_{int} \quad 2.3$$

, where σ is the surface tension of the working fluid, r_{eff} is the effective pore radius of the wick, and θ is the meniscus contact angle the liquid makes. The first term on the right hand side of equation 2.3 is the capillary limit and the second term is the internal pressure loss in the evaporator and is given by;

$$\Delta P_{int} = \Delta P_{lin} + \Delta P_{lw} + \Delta P_{vw} + \Delta P_{vgr} \quad 2.4$$

, where ΔP_{lin} is the pressure loss of the liquid flow in the inlet feeding the wick between position 4 and 5 in Figure 2.1, ΔP_{lw} is the pressure loss due to the movement of the liquid flow in the liquid region of the wick structure between position 5 and 6, ΔP_{vw} is the pressure loss caused by the vapour flow in the vapour zone of the wick structure between

position 1 and 2, and ΔP_{vgr} is the pressure loss of the vapour in the grooved evaporation channel and in the vapour line between position 2 and 3 given by Wulz and Mayinger (1993). Position 4 and 3 are essentially the inlet and exit of the evaporator.

The dominating pressure drop in equation 2.4 is due to the liquid flow in the wick structure (ΔP_{lw}).

2.3 EHD pumps

EHD enhanced fluid flow in thermal transport loops have been mentioned in review articles by Chang (1998). There are several different types of EHD pumps that have been investigated.

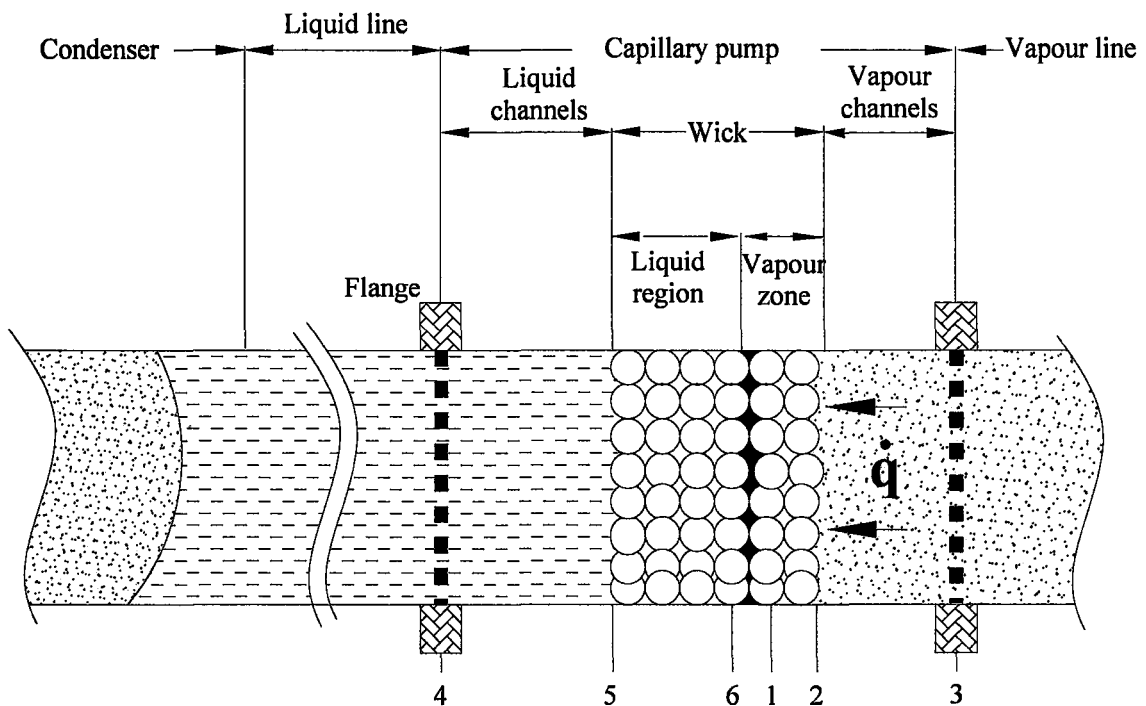


Figure 2.1: Pressure losses in the capillary pump redrawn from Wulz and Mayinger (1993) where \dot{q} = Heat flux.

These include: (a) single-phase ion drag or conduction EHD pumps, where pumping is achieved through an injection of ions to produce electrophoretic forces; (b) single-phase induction EHD pumping through an energized electrode array with temperature gradients that produces dielectrophoretic (DEP) forces on the working fluid and; (c) two-phase non-uniform travelling-wave dielectrophoresis (TWDEP). Optimizing the design of the electrode is usually achieved by modifying the electrode shape, width and pitch and by adjusting the voltage waveform, phase, frequency and amplitude. The fundamental understanding of the effect of EHD forces on fluid flow is still lacking and the design of optimized geometries of electrode arrays for moving dielectric fluids requires further investigation since electrode design is a critical criteria in effecting the fluid. Tables 2.1 and Table 2.2 give a summary of EHD pumps. It is important to be familiar with the different types of EHD pumps since the application of the EHD pumps may have an enhancement in the flow rate and thus the system of the CPL.

2.3.1 Single-Phase Flow Ion Drag and Pure Conduction Pump

Ion-drag pumping was first analyzed in by Stuetzer (1958) when he investigated the electromechanics of unipolar ion conduction between parallel plate electrodes with a DC applied voltage in an insulating liquid. Recirculatory (secondary) flow patterns were obtained with velocities up to 210 cm/s with a DC voltage of 23kV. Krawinkel (1968) later obtained fluid velocities as high as 780 cm/s with a DC voltage of 2.4 kV using an ion-drag pump with seven-stage ring electrode pairs. Sharbaugh and Walker (1985) developed an ion-drag pump using charge injection from a wire-mesh electrode placed in

the flow channel and then later attempted to show the relationship between pressure generation and flow rate of EHD pumps. The drawback of this design is that the wire mesh electrode produces a significant pressure drop (Bryan and Seyed-Yagoobi, 1992). Bryan & Seyed-Yagoobi (1992) proposed the use of emitter-ring electrodes with needles projecting into the flow from the wall of a circular channel and collector electrodes flush with the wall to reduce the pressure loss. They were not able to detect the effect of the EHD forces on the pipe core flow. Thus, even though the electrode was designed to minimize restrictions to the flow, it provided little additional bulk velocity to the flow. Hence, there are a number of competing factors that must be considered when designing the electrodes, as is typical in all EHD pumping applications.

2.3.2 Single Phase Induction Pump

The concept of an induction EHD pump or travelling-wave induced Electroconvection was introduced by Melcher (1966). A wave of imposed potential travels in the direction of flow and perpendicular to a gradient in the fluid conductivity. Conductivity gradients exist at vapour-liquid interfaces and across temperature and concentration gradients. It has been shown, however, that ionic conduction in dielectric liquids varies with temperature at high electric field values. Velocities up to 49 cm/s were obtained with 12 kV AC 3-phase TW by Bohinsky et al., (1990) and Seyed-Yagoobi et al. (1994). Crowley et al (1990) conducted experiments in order to plot the electric field against the velocity, and the upper limits that could be achieved using a single phase traveling wave pump were given.

2.3.3 Two-Phase Flow Traveling Wave Dielectrophoretic Pump

Another mechanism of EHD pumping is the use of Traveling Wave Dielectrophoretic (TWDEP) forces. The TWDEP forces can be generated from an embedded array of electrodes that act to convey a polyphase electric field down the length of the device referred to as Masuda panels. The manipulation of vapour bubbles using Masuda panels can be most useful in a microgravity environment due to the absence of the buoyancy forces. Masuda et al (1973) performed extensive analytical and experimental investigations of the traveling wave potential between an array of electrodes, which lead to a better understanding of this phenomenon and the design of these Masuda electric curtain flatbed panels. Aoyama et al (1977) investigated 6-phase TWDEP on a Masuda panel by levitating particles in air and obtained velocities upwards of 8 cm/s in air.

Chang et al. (1985) used a novel approach to obtain three different modes of operation (three-phase TW applied to the upper and lower electrodes individually and two-phase on both electrodes) on an electric curtain with a 150 Hz pulsed power supply. More recently, Morgan et al. (1997) used 4-phase TWD to manipulate blood cells and concluded that the linear force exerted on a particle is dependent on its size and also the conductivity of the particle. No relation between the diameter and electrode pitch could be established. However, traveling wave EHD pumps show a much higher performance over single-phase flow pumps. The initial work on the effect of DEP on bubbles was performed by Jones (1977), where he levitated nitrogen gas bubbles in corn oil. Campeau et al. (1986) investigated TWD effects on vapour bubbles in transformer oil and

concluded the acceleration/deceleration motion of bubbles through an inclined electric curtain channel, whereas Ogata et al. (1985) showed that DC electric fields can disrupt and disperse vapour bubbles.

2.3.4 EHD Two-Phase Capillary Pump

EHD enhanced heat pipes were originally proposed by Jones (1972). Mo et. al. (2000) developed an EHD enhanced CPL that incorporates a spring electrode inserted in the liquid line at the wicking structure of the evaporator. It is claimed that the electrode acts to push the liquid further into the evaporator so as to wet the wick. Applied voltages of up to 18 kV were used in a CPL filled with R134a to “reprime” the evaporator. Shelestynsky et. al. (2007) showed that an ion-drag type EHD pump could be used in a natural circulation loop to enhance the single-phase flow rate. In the absence of gravity, vapour will not move from the liquid to the condenser, a TWDEP pump on the liquid return line will act as a filtering mechanism for bubbles in the liquid line and since the bubbles will be directed away from the evaporator then the possibility of dryout is greatly diminished since the bubbly flow can even return to the condenser.

Dryout may occur as discussed in detail by Shelestynsky (2007), when bubbles are observed in the liquid line and since in microgravity buoyancy is not present the vapour may not return to the vapour line and may prevent liquid feeding into the evaporator. Another failure mode can occur due to the existence of a small gap between the fin-wick interface and with boiling will push a large vapour bubble from the surface of the fin, through the wick and into the vapour line. Dryout occurs here when the vapour

bubble becomes large enough that the liquid cannot feed into the fin-wick interface and again due to the absence of gravity the bubbles may not enter the vapor line and thus will end flow circulation in the CPL

Some background was given in this chapter in order to familiarize the reader with the CPL system. Discussions about the evaporator were made since it is responsible for the driving force of the CPL. Details of how this capillary force is generated by applying heat to the evaporator was shown and discussed. Introduction to different types of EHD pumps were discussed, as different types will have different effects on the fluid; this will help the reader in the latter chapters. Now that an introduction to the mechanisms of the evaporator in the CPL and EHD pumping are given, chapter three will discuss the EHD flow background as well as the effect it has in the evaporator of current interest.

Table 2.1: Review of EHD pump research (after Shelestynsky, 2007)

Reference	Steutzer (1959)	Krawinkel (1968)	Sharbaugh & Walker (1985)	Bryan & Seyed-Yagoobi (1992)	Melcher (1966)	Bohinsky & Seyed-Yagoobi (1990)	Margo & Seyed-Yagoobi (1994)	Hemstreet (1985)
Pump Type	Ion-Drag (Horizontal Plates)	Ion-Drag	Ion-Drag (Horizontal Mesh Electrodes)	Ion-Drag (Vertical Ring Electrodes w/ needles)	Induction Travelling wave potential (Horizontal)	Induction - Travelling wave potential (Vertical)	Induction - Travelling wave potential (Vertical)	TWD Microhandling of particulates
Fluid	Kerosene	Acetone	Shell Oil	Dodecylbenzine	Arcolor	Hexane	Hexane	Air
E (kV)	23 DC	3 DC	20 AC	25 DC	23	12 (3-phase AC) @ 6 Hz	12 (3-phase AC) @ 8 Hz	5 kV(4-phase AC)@ 60 Hz
U (cm/s)	210	780	5	23	3	35	49	200
Efficiency	20	30	N/A	5.5	N/A	N/A	N/A	N/A
Flow Regime	Turbulent/ Single Phase	Turbulent/ Single Phase	Turbulent/ Single Phase	Laminar/ Single Phase	Turbulent/ Single Phase	Turbulent/ Single Phase	Turbulent/ Single Phase	
Significant Contribution	EHD phenomena	Electrode design	Electrode design	Electrode design	Travelling Wave EHD	Electrode design	Electrode design	Electrode design

Table 2.2: Review of EHD pump research continued

Reference	Aoyama & Masuda (1977)	Moesner et al (1999)	Aoyama et al (1993)	Campeau et. al (1986)	Mo, Ohadi, Dessiatoun & Wren (2000)	Bryan & Seyed-Yagoobi (1997)	Babin, Peterson & Seyed-Yagoobi (1993)	Ohyama, Watson & Chang
Pump Type	TWD Microhandling of particulates	Electric tube micro-pump	TWD control of air bubbles	TWD control of air bubbles	EHD assisted CPL Evaporator	EHD pumping in a monogrove heat pipe	Ion-Drag assisted CPL	Interfacial Shear
Fluid	Air	Air & corn oil	Air & Kerosene	Air & Mineral Oil	R134a	R134a	R134a	Mineral Oil
E (kV)	20 kV (6-phase) @ 50 Hz	1 kV(6-phase) @ 3.5 Hz	15 kV (3-phase)	5 kV (3-phase)	18	20		
u (cm/s)	8	0.1	10		N/A	N/A	N/A	
Efficiency	N/A	N/A	N/A	N/A	N/A	N/A	N/A	
Flow Regime		Single Phase		Bubbles in a Stagnant liquid	Two Phase	Two Phase	Two Phase	Two-phase
Significant Contribution	Fundamental Understanding of non-uniform electrical potential fields	Electrode design -	Control of bubbles against buoyancy force ($F_{dep} = F_{buoyancy}$)	Acceleration/ deceleration motion observed on bubbles moving through inclined Electric curtain channel	EHD enhanced Capillary action	Ion drag assisted capillary action	Heat pipe repriming	

Chapter 3

ELECTROHYDRODYNAMIC FLOW

This chapter will explain what occurs when a voltage is applied to an electrode submerged in liquid fluid. The conservation equations will be presented first for EHD flow. Then a discussion of the EHD applied to single-phase fluids is made to assist in understanding the main scope of this work; EHD in two-phase flow.

3.1 Electrohydrodynamic

Electrohydrodynamic forces can be generated by applying high-voltage electric field and coupling this with a flow field of a dielectric fluid to generate an external body force that induces fluid motion. The high voltage is usually applied between a charged electrode and a grounded electrode. Hydrodynamic effects resulting from this applied voltage such as turbulence and flow eddies have been experimentally observed by Avsec (1937) and Pickard (1965) for single-phase liquid flow. This flow motion is essentially induced by the Coulomb force and has two basic driving mechanisms for single-phase flow as shown in Figure 3.1 by Peters (1980a), the first dominates low-field motion; which is the diffuse charge in the liquid close to the wall is swept away by the tangential components of the field. The second is manifest at high field strengths and is caused by the injection of free charges from the electrodes not shown in Figure 3.1. An externally applied dc electric field across a plane layer of a dielectric liquid cause's instability in the layer that is sometimes also called electroconvection (Chang, 1995).

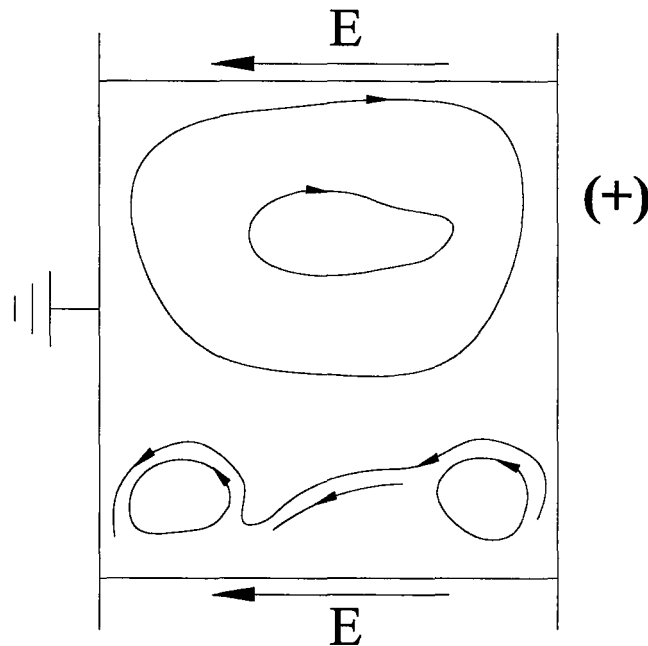


Figure 3.1: Electroconvective motion of carbon tetrachloride and kerosene mixture with polyethylene particles, 5kV dc field redrawn from (Peters, et. al. 1980a)

Electroconvection may enhance convective heat transfer, especially in low Reynolds number flow through narrow spaces, where the application of any convective passive enhancement method is neither easy nor effective. However in order to understand this induced flow physical mechanism and heat transfer enhancement phenomena, the theory of EHD as well as the EHD phenomena for single-phase and liquid-vapour interface will be reviewed.

3.2 Conservation equations for EHD single-phase flow

The mass, momentum, and energy conservation equations of a fluid under corona discharges can be approximately expressed for laminar flow as follows (Chang and Watson, 1994):

Mass conservation

$$\frac{\partial \rho}{\partial t} + \nabla \cdot (\rho \vec{U}) = 0 \quad 3.1$$

Momentum conservation

$$\rho \frac{\partial \vec{U}}{\partial t} + \rho (\vec{U} \cdot \nabla) \vec{U} = -\rho g \beta (T - T_s) - \nabla P + \mu_g \nabla^2 \vec{U} + \vec{F}_{EB} \quad 3.2$$

Energy conservation

$$\frac{\partial T}{\partial t} + \vec{U} \cdot \nabla T = \frac{\kappa}{\rho C_p} \nabla^2 T + Q_{EB} \quad 3.3$$

Ion transport

$$\frac{\partial N_i}{\partial t} = \vec{U} \cdot \nabla N_i \pm \mu_i \nabla \cdot (N \nabla V) - D_i \nabla^2 N_i \quad 3.4$$

Poisson equation

$$\nabla^2 V = \frac{-e N_i}{\epsilon} \quad 3.5$$

, where \vec{F}_{EB} is the momentum and energy change due to the presence of electric fields and Q_{EB} is the Joule heating.

The free charge, the electric dipole and the magnetic dipole interactions contribute to the force in equation 3.2, hence the force density changes due to the electric field is as follows:

$$\begin{aligned} \vec{F}_{EB} &= \rho_{ie} \vec{E} + J_x \vec{B} - \frac{1}{2} E^2 \nabla \epsilon - \frac{1}{2} H^2 \nabla \mu + \nabla \left[\frac{1}{2} \rho E^2 \left(\frac{\partial \epsilon}{\partial \rho} \right)_T + \frac{1}{2} \rho H^2 \left(\frac{\partial \mu}{\partial \rho} \right)_T \right] \\ \vec{F}_{EB} &= \vec{F}_1 + \vec{F}_2 - \vec{F}_3 - \vec{F}_4 + \vec{F}_5 \end{aligned} \quad 3.6$$

The force density in the fluid consists of the terms:

1. Term $F_1 = \rho_{ie} \vec{E}$ is the force density due to the space charge
2. Term $F_2 = J_x \vec{B}$ is the force density due to the charged particle motion
3. Term $F_3 = \frac{1}{2} E^2 \nabla \epsilon$ is the force density due to the dielectric property change
4. Term $F_4 = \frac{1}{2} H^2 \nabla \mu$ is the force density due to the fluid permeability changes
5. Term $F_5 = \nabla \left[\frac{1}{2} \rho E^2 \left(\frac{\partial \epsilon}{\partial \rho} \right)_T + \frac{1}{2} \rho H^2 \left(\frac{\partial \mu}{\partial \rho} \right)_T \right]$ is the force density change due to the electrostriction and magnetostriction effects

The additional energy terms due to the electromagnetic field can also be obtained as:

$$Q_{EB} = (\vec{J} - \rho_{ie}\vec{U})(\vec{E} + \vec{U} \times \vec{B}) + \nabla \cdot [(\vec{E} + \vec{U} \times \vec{B}) \times (\vec{H} - \vec{U} \times \vec{D})] + \left[\vec{E} \frac{d}{dt} \left(\frac{\vec{D}}{\rho} \right) + \vec{H} \frac{d}{dt} \left(\frac{\vec{B}}{\rho} \right) \right] \rho$$

3.7

, where the first term is the heat generation due to flow of charged particles, such as ohmic heating, the second term is the energy due to the polarization such as electromagnetic hysteresis loss and the third term is the energy due to the displacement current and time varying magnetic fields, such as energy storage in an electromagnetic system.

The importance of each term in equation 3.6 and 3.7 depends on the working fluid (Chang, 1998 in table 3.1).

The electrohydrodynamic applications are generally high voltage and low current electric fields. Due to this low current flux, the generated magnetic field can be neglected and therefore the electric field will be the dominant factor in equation 3.6 and can therefore be simplified to;

$$\vec{F}_{EB} = \rho_{ie}\vec{E} - \frac{1}{2}E^2\nabla\epsilon + \nabla\left[\frac{1}{2}\rho E^2\left(\frac{\partial\epsilon}{\partial\rho}\right)_T\right]$$

3.8

Table 3.1: Relative Importance of EHD terms (Chang, 1998)

Type of Fluid		Momentum terms due to EMF: f_{eB}	Energy terms due to EMF: q_{eB}^m	Comments
Non-Conducting Fluids ($I \rightarrow \text{small}$)	Gas Single Phase	$1/2 \epsilon_0 (\epsilon_s - 1) \nabla E^2 + 1/2 \mu_0 (\mu_s - 1) \nabla H^2$	$\nabla \cdot (\bar{E} \times \bar{H}) + [\bar{E} \cdot d(\bar{D}/\rho)/dt + \bar{H} \cdot d(\bar{B}/\rho)/dt] \rho$	$\mu_s = 1, \epsilon_s = 1$ $\nabla \epsilon \nabla \mu \rightarrow \text{small}$
	Liquid Single Phase	$1/2 E^2 (\partial \epsilon / \partial T) \rho \nabla T$	(same as for gas)	$\rho \partial \epsilon / \partial \rho, \rho \partial \mu / \partial \rho$ $\nabla \mu \rightarrow \text{small}$
	Gas-Liquid Two-Phase	$-1/2 E^2 \nabla \epsilon - 1/2 H^2 \nabla \mu$ (for each phase) $+ \nabla \left(1/2 E^2 \rho \partial \epsilon / \partial \rho + 1/2 \rho H^2 \partial \mu / \partial \rho \right)$	(same as for gas but for each phase)	$\rho_w = \alpha_v \rho_v + (1 - \alpha_v) \rho_l$ $\epsilon_l, \mu_l \gg \epsilon_v \mu_v$
Conducting Fluids ($I \neq 0$)	Gas Single Phase	$\rho_e \bar{E} + \bar{J} \times \bar{B}$ $+ \nabla \left(1/2 E^2 \partial \epsilon / \partial \rho + 1/2 \rho H^2 \partial \mu / \partial \rho \right)$	$\bar{J} \cdot \bar{E} + \nabla \cdot (\bar{E} \times \bar{H}) + [\bar{E} \cdot d(\bar{D}/\rho)/dt + \bar{H} \cdot d(\bar{B}/\rho)/dt] \rho$	$\rho_e \neq 0, \nabla \epsilon, \nabla \mu \rightarrow 0$ $\bar{J} = \bar{u} n \pm \mu' n \bar{E} - D \bar{\nabla} n$
	Liquid Metal Single Phase	$\bar{J} \times \bar{B}$	$\bar{J}^2 / \sigma_e + \nabla \cdot (\bar{E} \times \bar{H}) + \rho \bar{H} \cdot d(\bar{B}/\rho)/dt$	$\rho \partial \epsilon / \partial \rho, \rho \partial \mu / \partial \rho \rightarrow 0$ $\bar{J} = \mu \bar{E}, \rho_e = 0$ $\nabla \epsilon, \nabla \mu \rightarrow 0$
	Liquid Single Phase	$\rho_e \bar{E} + \bar{J} \times \bar{B} + 1/2 E^2 (\partial \epsilon / \partial T) \rho \nabla T$	(same as for gas)	$\nabla \mu, \rho \partial \epsilon / \partial \rho, \rho \partial \mu / \partial \rho \rightarrow 0$ $\rho_e = \rho_+ - \rho_-$
	Gas-Liquid Two-Phase	$-1/2 E^2 \nabla \epsilon - 1/2 H^2 \nabla \mu + \nabla \left(1/2 \rho E^2 \partial \epsilon / \partial \rho + 1/2 \rho H^2 \partial \mu / \partial \rho \right) + \bar{J} \times \bar{B} + \rho_e \bar{E}$ (for each phase)	(same as for gas but for each phase)	$\bar{J}^* = \sigma \bar{E}^*$ $\bar{E}^* = \bar{E} + \bar{U} \times \bar{B}$ $\bar{H}^* = \bar{H} - \bar{U} \times \bar{D}$

The three terms in equation 3.8 are the electrophoretic, dielectrophoretic and electrostrictive components of the force, respectively. The physical significance of each term is summarized as follows: (Cotton et. al, 2005)

- i) The *electrophoretic* force results from the net free charge within the fluid or injected from the electrodes. The interactions within the individual phases are typically associated with this component.

- ii) The *dielectrophoretic* force is a consequence of inhomogeneity or spatial change in the permittivity of the dielectric fluid due to non-uniform electric fields, temperature gradients, and phase differences.
- iii) The *electrostrictive* force is caused by an inhomogeneous electric field strength and the variation in dielectric constant with temperature and density.

The importance of these three terms will be discussed in the following sections of this chapter.

The energy terms are also reduced in equation 3.7 to;

$$Q_{EB} = \sigma_e E^2 \quad 3.9$$

in a similar manner, however the energy term is considered negligible when applied to a dielectric fluid, since the conductivity (σ_e) in typical dielectrics range from 10^{-10} to $10^{-16} \Omega^{-1}m^{-1}$ as reported by Cotton et. al (2005).

3.3 Single-phase gas and liquid EHD flow

It is possible to simplify the electrohydrodynamic equations presented by dimensionless conservation equations for a laminar EHD gas flow without temperature gradient as follows; (Chang and Watson, 1995)

- i) Mass conservation
$$\nabla \cdot (\vec{u}) = 0 \quad 3.10$$

- ii) Momentum conservation
$$\vec{u} \cdot \nabla \vec{u} = -\nabla p + \frac{Ehd}{Re^2} n \vec{\eta} + \frac{1}{Re} \nabla^2 \vec{u} \quad 3.11$$

iii) Ion transport

$$\frac{\text{ReSc}\bar{u}}{2} \cdot \nabla n \pm F_E \nabla \cdot (n\bar{\eta}) - \nabla^2 n = 0 \quad 3.12$$

iv) Poisson equation

$$\nabla^2 \phi = -(D_b)^2 (n_+ - n_-) = \nabla \cdot \bar{\eta} \quad 3.13$$

or

$$D_b^2 n = F_E \nabla \cdot \bar{\eta}$$

,where the nondimensional variable are

$$n = \frac{N}{N_s}; \quad \phi = \frac{eV}{kT}; \quad \text{Sc} = \frac{\nu}{D}; \quad \bar{\eta} = \frac{E}{E_s}; \quad F_E = \frac{\mu_i V_s}{D_i}; \quad \text{Re} = \frac{U_s L}{\nu_f}; \quad \text{Ehd} = \frac{I_T L^3}{Ap_f \nu_f^2 \mu_i};$$

$$D_b = \left(\frac{L}{\lambda_D} \right)^2; \quad p = \frac{P}{\rho_f U_s}$$

where F_E is the electric field number, Sc is the Schmidt number, Ehd is the EHD number, D_b is the Debye number and Re is the Reynolds number.

The specific dielectric constant is almost constant for most of the gas mixtures without significant temperature gradients and hence it can lead to the elimination of the second and third term in equation 3.8. Assuming no temperature gradient in the system, the dominating force for single phase will result from the interaction of the electric field with free space-charges or simply the Coulomb force (electrophoresis term) as follows;

$$F'_E = \rho_{ie} \bar{E} \quad 3.14$$

This single phase EHD effect is referred to as corona discharge for gas phase and electroconvection for dielectric liquids as noted in the works of Chang and Watson (1994), Bryan and Sayed-Yagoobi (2000) and Yabe (1995).

The liquid-vapour interface phase change is the main focus of heat transfer enhancement. It has been reported by Velkoff and Miller (1965), Chang (1998), and Sayed-Yagoobi (2000) that the dominating force in equation 3.8 are the dielectrophoretic

and electrostrictive forces due to the difference in permittivity between the liquid-vapour interface and the equation 3.8 is reduced to.

$$\vec{F}_{EB} = -\frac{1}{2} E^2 \nabla \varepsilon + \nabla \left[\frac{1}{2} \rho_f E^2 \left(\frac{\partial \varepsilon_f}{\partial \rho_f} \right)_T \right] \quad 3.15$$

The dimensionless numbers in order to show the effects of the electric field is represented by the following dimensionless number based on term 1 in equation 3.8 (IEEE-DEIS-EHD Technical Committee 2003) as follows;

$$Ehd = \frac{I_s L^3}{A \rho_f \nu_f^2 \mu_i} \quad 3.16$$

is the EHD number or conductive Rayleigh number which is a comparison of the electrophoretic force to the viscous forces and based on term 1 in equation 3.15 (IEEE-DEIS EHD Technical Committee 2003) as follows;

$$Md = \frac{\varepsilon_o E_s^2 L^2}{\rho_f \nu_f^2} \quad 3.17$$

is the Masuda number or dielectric Rayleigh number which is a ratio of the dielectrophoretic force to the viscous force. Based on term 2 in equation 3.15, the electrostriction number (IEEE-DEIS EHD Technical Committee 2003) is given by;

$$Es_E = \frac{\varepsilon_o E_s^2 L^2}{\beta \Delta T_o \rho_f \nu_f^2} \quad 3.18$$

The Grashof number is given by

$$Gr_L = \frac{g \beta \Delta T_s L^3}{\nu_f^2} \quad 3.19$$

which is a comparison of the thermal buoyancy force to the viscous force. By scaling arguments the forced convection is dominant over natural convection, when $Gr/Re^2 < 1$.

From Chang and Watson (1994) and Cotton et. al. (2005), the analogy of free convective flows, the combined effects of electric and forced convection must be considered when $\frac{Ehd}{Re^2} \sim 1$ and/or $\frac{Md}{Re^2} \sim 1$. These dimensionless numbers will clarify

which external body force is dominant. The electrophoretic force is dominant over inertia when $\frac{Ehd}{Re} > 1$ and similarly the dielectrophoretic force is dominant over inertia when

$$\frac{Md}{Re^2} > 1.$$

For this work the dielectrophoretic forces may be the dominant force based on these dimensionless numbers since $\epsilon_1 = 9.5$ for liquid Refrigerant HFC-R134a compared to $\epsilon_2 = 1.09$ for vapour in two-phase flow. It is important to discuss the EHD phenomena in liquid-vapour since the experiment in interest will have a two-phase flow inside the evaporator. (see Appendix C)

3.4 EHD in liquid-vapour interface

Since there is a phase change inside the evaporator, the surface instability due to the electric fields and the various EHD convection phenomena in liquids are an important part of the enhancement. Based on the model of Pohl (1958) and Chang (1998) a figure is drawn to show the effect of the electric field on the interface of vapour-liquid, droplets and bubble have on the fluid motion. There are four different phases occurring or a combination of phases inside the evaporator as shown separately by figure 3.2. Since the dielectric permittivity is larger for the liquid, the vapour will act as an insulator, whereas the liquid will act as a conductor. The influence of the body force can be written as an interfacial force, also known as the dielectrophoretic force and given by;

$$\begin{aligned}
 F_{\text{int}} &= \frac{1}{2} E^2 \nabla \epsilon \\
 &\approx \frac{1}{2} E^2 \frac{(\epsilon_l - \epsilon_v)}{L}
 \end{aligned}
 \tag{3.20}$$

This is normal to the interface and is directed from conductor (liquid) to insulator (vapour). Figure 3.2a) is a stratified vapour-liquid state, where liquid is between the two electrodes and has a vapour film at the ground surface. This vapour region is called film boiling and the direction of the electric field is from positive electrode to the ground. Film boiling occurs when a layer of liquid is in contact with the heated surface and the temperature of the surface is much higher than the saturation of the liquid. The liquid at the surface turns to vapour and creates an insulating effect, which reduces the rate of the heat transfer.

Figure 3.2b) show the liquid-vapour interface where liquid is at the ground surface and vapour between the liquid and the positive electrode. Here this force makes the liquid surface extend in the gas toward the electrode and away from the ground surface. This slight rise of the liquid surface will increase the dielectrophoretic force and raise the liquid surface even more due to the decrease of the distance between the surface and the electrode since the dielectrophoretic force is inversely proportional to the length.

Figure 3.2c) shows a droplet, whose diameter is on the mm order, being pulled towards the positive electrode from an annular liquid film below $100\mu\text{m}$. Again the interfacial force is directed from the liquid to the vapour as shown.

Finally figure 3.2d) is an occurrence of a bubble in the liquid state. Since the dielectric permittivity of a vapour (bubble) is near that of a vacuum and liquids have dielectric constants greater than that of a vacuum, the vapour bubble will be attracted to the regions of lower field strengths. This figure is valid under the conditions that; $\nabla T_g \approx \nabla T_l \approx 0$

and $T_{g\text{int}} = T_{l\text{int}}$, meaning that the temperature change across the vapour or liquid is approximately zero and that there is no external heat applied, and where the vapour and liquid temperature are the same. This is for the condition of the wire-plate electrode where $\epsilon_l > \epsilon_v$. The next chapter will present the experiment apparatus, the instrumentations and the procedure taken in order to start up of the system.

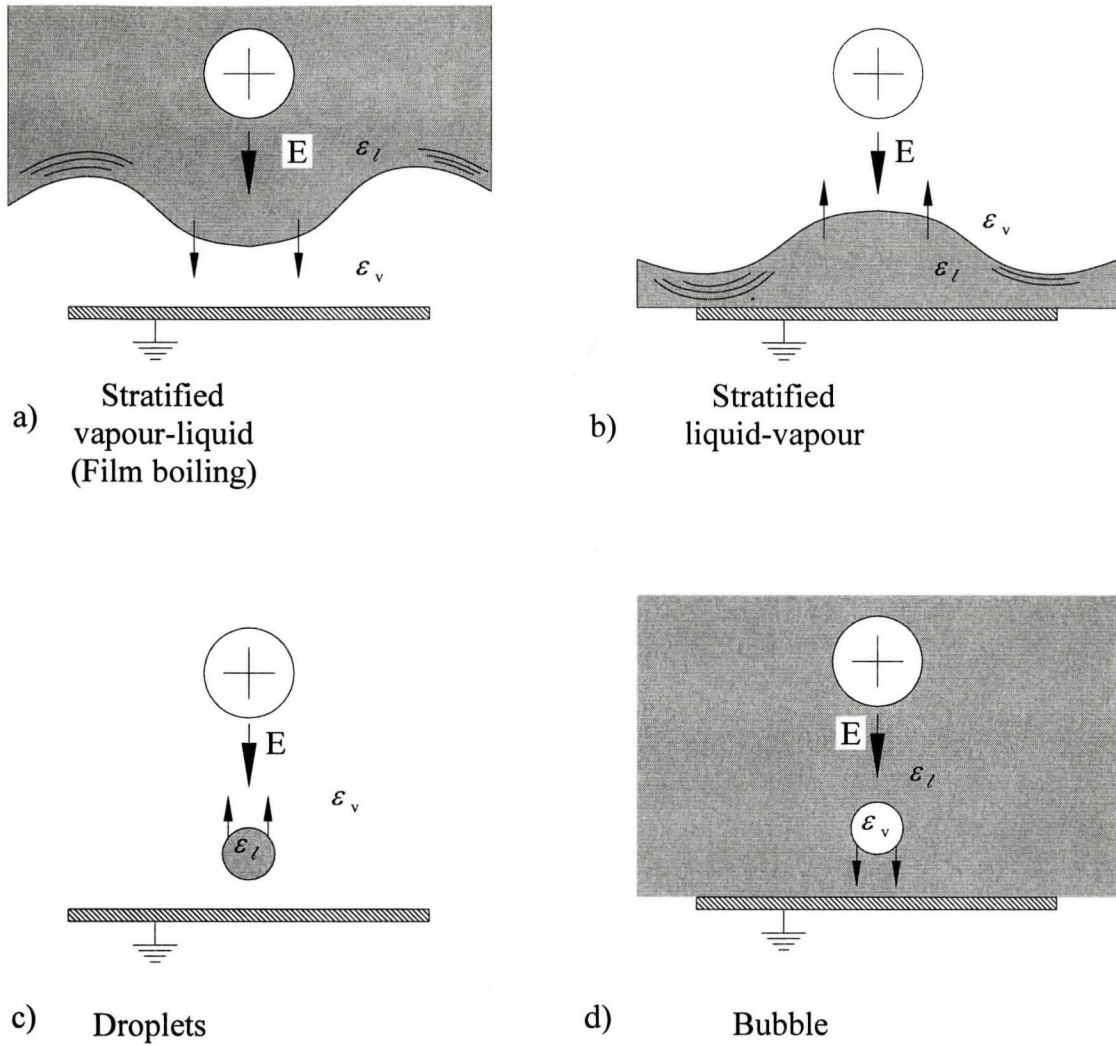


Figure 3.2: EHD instability on the vapour-liquid interface for a) stratified vapour-liquid b) stratified liquid-vapour c) droplets and d) bubble under wire-plate electrodes

Chapter 4

EXPERIMENTAL FACILITIES

The experimental apparatus is discussed in this chapter as well as the experimental methodology. The experimental apparatus consists of a Capillary Pumped rig and associated instrumentation. The instrumentation consists of thermocouples, pressure transducer, and ultrasonic transducers for the measurement of temperature, pressure difference across the evaporator and the flow rate, respectively. The application of high voltage to the electrode in the enhanced capillary evaporator (ECE) is designed to increase the flow rate of this system. This chapter will present the details of the EHD-enhanced capillary evaporator (EHD-ECE) test apparatus, and methodology.

4.1 Experimental Apparatus

4.1.1 Capillary pump rig

The present setup is called a rig instead of a loop since the main objective of this work is to increase the flow rate due to the addition of an electric field to the evaporator. Hence the main focus is therefore the enhancement of the evaporator device. Figure 4.1 shows the schematic of the experimental facility with dimensions of 120x30x90 cm³. The setup consists of three stainless steel tanks: condensate collection tank, liquid tank, liquid reservoir tank. Stainless steel tubing of 12.7 mm diameter was used to complete the loop. The electrical power that was applied to the evaporator heater was manually applied by a Variac (1.4 KVA)

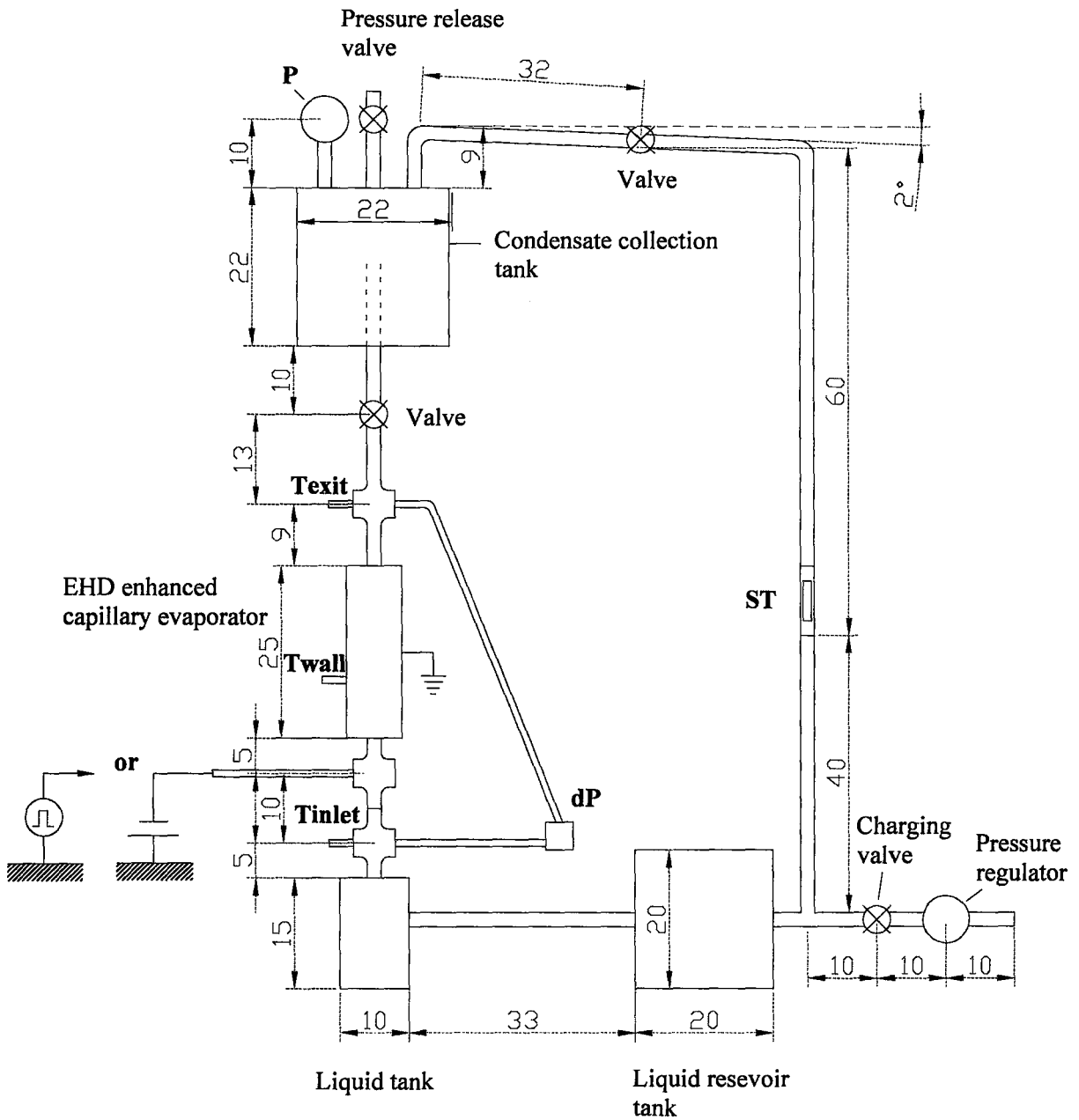


Figure 4.1: Schematic of test loop and location of measurement instruments
 T_{inlet} , T_{wall} , T_{exit} : Thermocouples, dP : Pressure transducer, P : Pressure gauge ST : Sight tube

and recorded by the Extech power multi-meter (Model 382860). A photograph of the test rig is shown in Figure 4.2.

The methodology will be given in the latter of this chapter, however in order to discuss the apparatus it is necessary to discuss the overall operations of the experiment. The wick in the evaporator requires being fully wetted before start-up, once heat is applied the liquid refrigerant will evaporate into the vapour grooves and up-ward to the vapour channel to the condensate collection tank as shown by Figure 4.2.

4.1.2 Capillary evaporator

The evaporator is a 220 mm long aluminum housing with square inlet and outlet frame of 38x38 mm², an outer diameter of 30 mm and an inner diameter of 19 mm as shown in Figure 4.3.

The porous media, called the wick, is placed press fitted inside the evaporator so that good contact is made between the wick and the fins. Both ends of the evaporator are manufactured for a connection to 6.35mm Swagelok connection, one end to the vapour line and the other to the liquid line. One side of the wick is pushed against the inlet of the evaporator so that only liquid enters the wick; the other was supported by a Teflon piece with a spring at the exit so that the vapour grooves allow the vapour to exit the evaporator as shown in Figure 4.3.

Three band heaters are clamped on the outside of the evaporator body. Electrical heaters are connected to the band heaters and input power was manually controlled. At start-up the pores of the wick at the liquid-vapour interface are wetted with liquid.

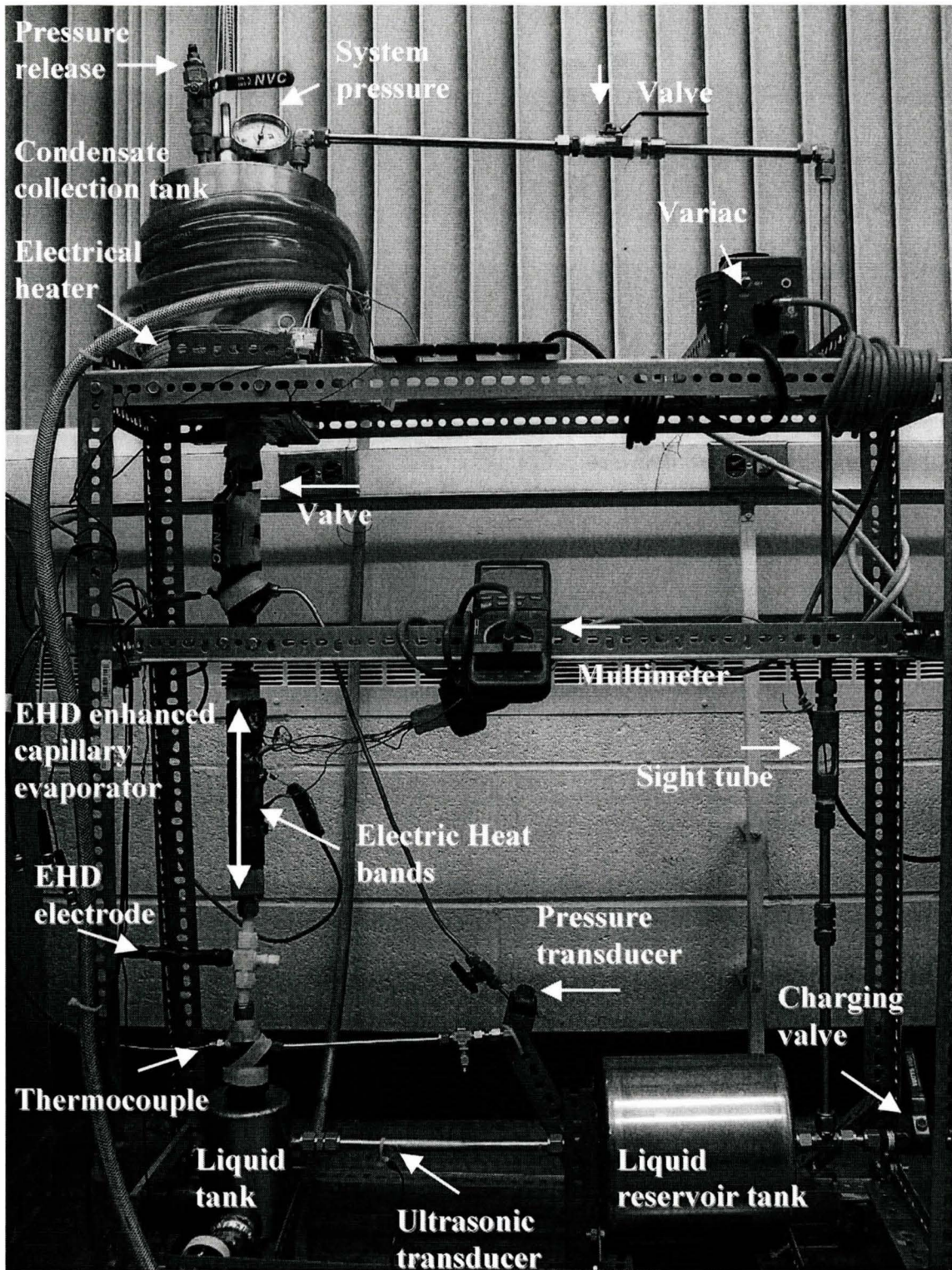


Figure 4.2: EHD-ECE test layout

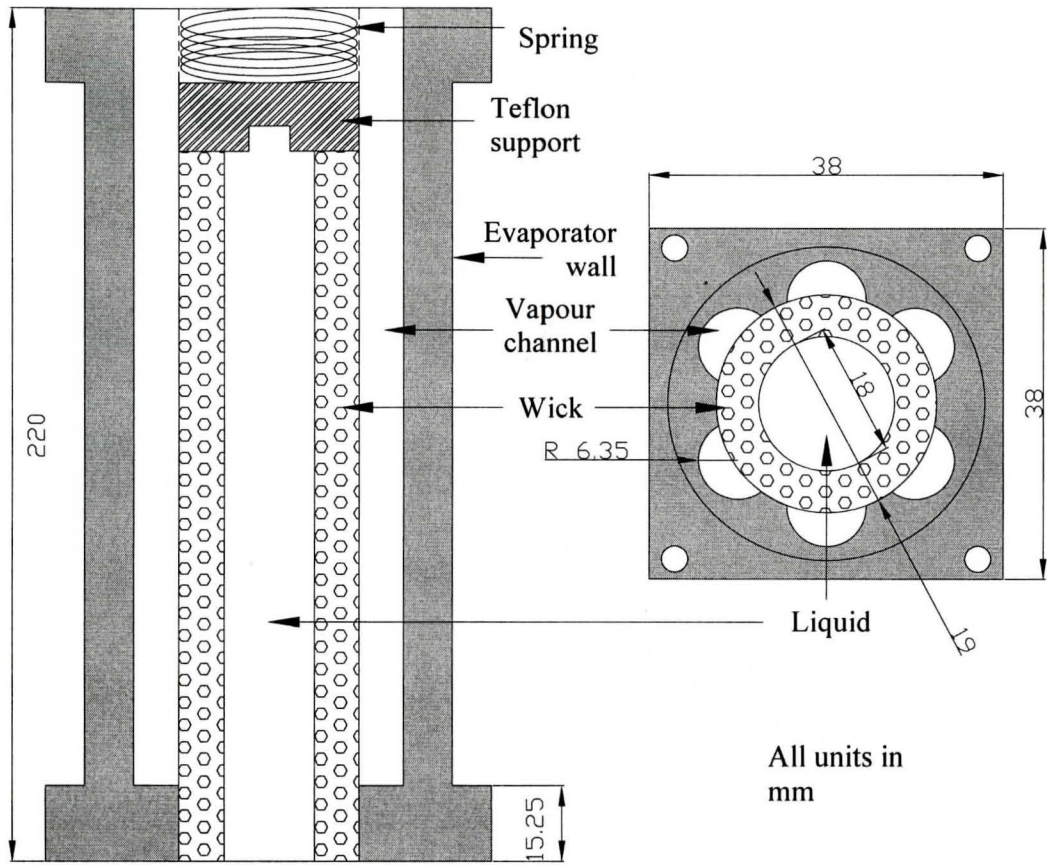


Figure 4.3: Schematic of experimental evaporator

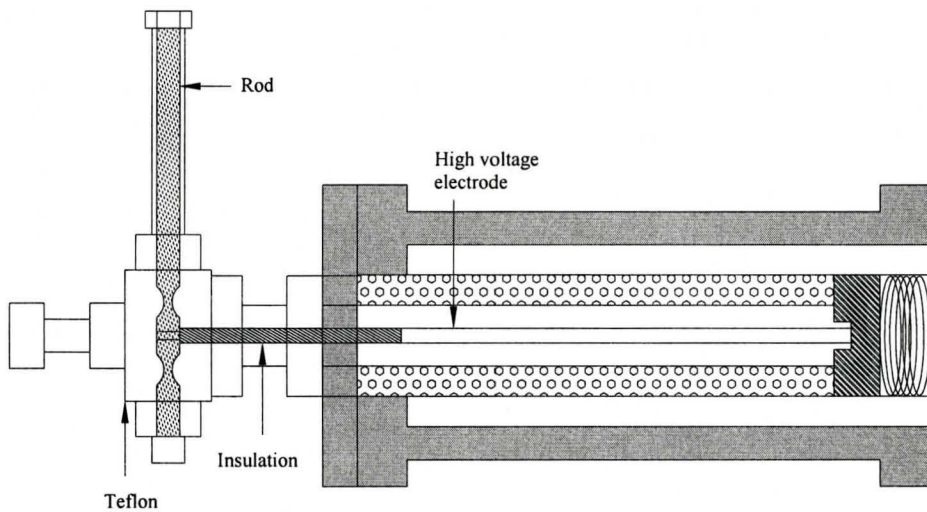


Figure 4.4: Schematic of EHD enhanced capillary evaporator with high voltage electrode

The applied heat in the evaporator is transferred through the fin to the liquid-vapour interface. Evaporation will occur at this interface and vapour will flow into the vapour groove. Thus the liquid is drawn through the wick to the liquid-vapour interface to preserve mass balance. At the same time, capillary menisci are established at the interface with an effective contact angle θ as discussed in equation 2.3. These menisci facilitate the pumping function, which again draws the liquid from the wick to the liquid-vapour interface.

4.1.2.1 Ultra high molecular weight polyethylene wick

The wick is one of the most critical pieces as its pore sizes and porosity are responsible for the capillary forces, which are capable of developing very high capillary heads. The ultra high molecular weight polyethylene (UHWPE) wick has an average pore size of $20\mu\text{m}$ with 50% porosity. The outside diameter is 20mm with an inner diameter of 18mm. The melting temperature is around 150°C and the temperature of the evaporator wall temperature (see Figure 4.3) should be kept below this temperature.

4.1.2.2 High voltage electrode arrangement

The stainless steel electrode, 3.1mm in the center of the wick, as shown in Figure 4.4, is held by a 12.7mm O.D. Swagelok union Teflon cross. The horizontally rod is 6.35mm O.D. and the electrode is press fitted orthogonal to the rod rising up to the evaporator. The orthogonal electrode is insulated with Teflon tubing up to the end of the evaporator entrance to reduce the probability of any discharge with the stainless steel

fittings. A Teflon cap that has been drilled to insert the electrode inside as shown in Figure 4.4 supports the top of the vertical electrode.

When a voltage is applied to the electrode, an electric field is applied to the evaporator wick, the liquid-vapor interface, and driving the instability-induced Maxwell stresses, which will contribute to providing substantial improvement in CPL performance.

4.1.3 Condensate collection tank

The condensate collection tank (CC-tank) was cooled by cold water in 19mm O.D. Tygon tube in the secondary side. This is to ensure that transported fluid was condensed and the condensate liquid level, hence the flow rate, can be measured. The cooling water flow rate is set to an arbitrary 5 L/min for all experiments; this value should be adjusted in the future to observe its contribution. Upon completing one set of experiments, any vapour that was condensed in the CC-tank will be required to be removed in preparation for the next set of experiments.

In order to remove this liquid from the CC-tank, heat was applied via an electric heater shown in Figure 4.5 in order to evaporate this liquid. The liquid reservoir tank is kept cool in order to condense the vapour from the CC-tank back to liquid state in the liquid reservoir tank. Once all the liquid is removed from the CC-tank, the system is allowed to reach steady state and now is once again ready for start-up.

The condensate collection tank has a radius of 11 cm and a height of 22 cm as shown in figure 4.5. One port is at the bottom where the vapour would enter and three

ports are on the top for the system pressure, pressure relief and the return line back to the reservoir tank. The port from the evaporator continues 12 cm inside the tank in order to avoid any reflux into the vapour channel, which would affect the evaporator performance. The liquid tank has dimensions of radius 5 cm and height 15 cm with two ports, one connected from the liquid reservoir tank and the other connected to the inlet of the evaporator.

The liquid reservoir tank has dimensions with radius of 10 cm and a height of 20 cm with two ports, one from the return line and the other to the liquid tank.

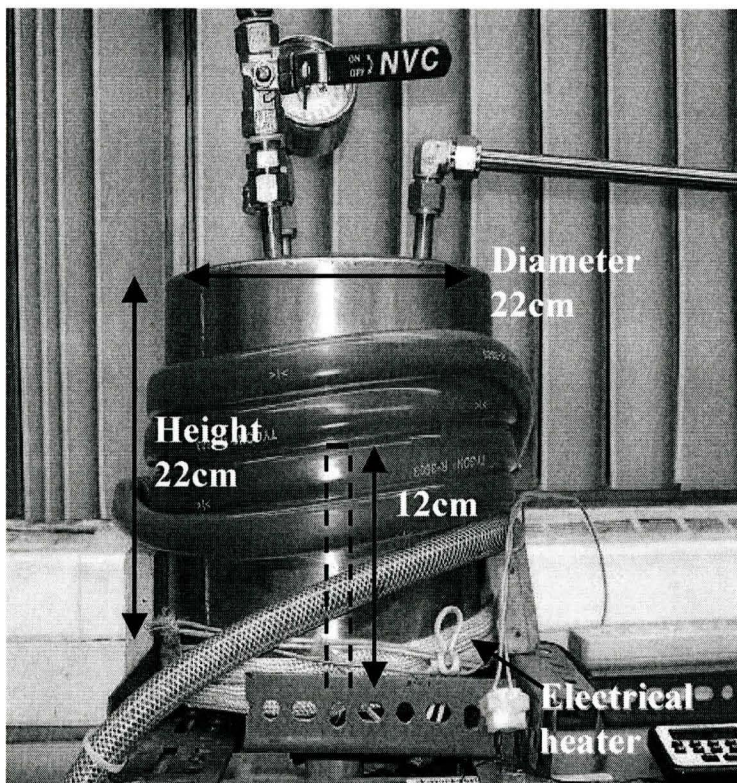


Figure 4.5: Condensate collection tank

4.1.4 Instrumentation

The test facility is equipped with measurement sensors for the pressure difference across the evaporator, as well as the wall temperature, the exit temperature and inlet temperature of the evaporator. The flow rate was determined by liquid level measurements of the condensate collection and liquid reservoir tank via an ultrasonic method.

Data is collected using a National Instrument high performance PC platform for data acquisition applications. An Intel Pentium III CPU operates it with 863 MHz processor frequency and 256 MB RAM and running Microsoft© Windows XP professional. The embedded controller (PXI-8187) integrates the Pentium 4 processor with the data acquisition board chassis (PXI-6115) for measurement modules.

4.1.4.1 Data acquisition board

The National Instruments data acquisition (PXI-6115) delivers high performance capabilities for measuring high-bandwidth signals. The features are 10 MS/s simultaneous sampling, 12-bit resolution and up to $\pm 42V$.

The National Instruments TB-2705 is a screw terminal block for the PXI-6115 and analog output modules that use a 68-pin D-type connector.

4.1.4.2 Temperature measurements

T-type Omega Inc. thermocouples were used to measure the refrigerant liquid (T_{inlet}), vapour (T_{exit}) and the evaporator wall temperature (T_{wall}). The evaporator wall

was measured by applying an Omegatherm-201 thermally conductive silicon paste that is rated for -40°C to 200°C , to safely attach the thermocouple to the evaporator wall. Temperatures were taken at the inlet and exit of the evaporator with a 1.5875mm T-type thermocouple that was held by a 1.5875mm to 6.35mm stainless steel Swagelok tube fitting. This fitting was chosen to fit to the stainless steel Swagelok union-cross connected to the main vertical pipe of the inlet and exit evaporator. The thermocouple locations are shown in Figure 4.1.

4.1.4.3 Pressure measurements

A Validyne model DP15 differential pressure transducer was used to measure the pressure difference between the evaporator located at the stainless steel union cross of the inlet and exit, 490 mm apart. The diaphragm used was range dash no. 32 and rated linear for a maximum of 13.8 kPa with accuracy of $\pm 0.25\%$ FS hence measurement accuracy was ± 0.0345 kPa.

The pressure transducer is connected to a Validyne Carrier Demodulator, which operates with variable reluctance transducers to provide a DC output signal $\pm 10\text{V}$ for measurements. The pressure transducer is calibrated by using the Demodulator and the Crystal IS33 pressure gage with accuracy of 0.05% of reading. The pressure drop location is also shown in Figure 4.1 as dP.

4.1.4.4 Ultrasonic transducers and liquid level measurement

Four Parametric ultrasonic transducers model A112S-RM, 10MHz, 8.88mm diameter with 10.6mm high contact transducers were used which were connected to the Panametric pulser receiver model 5052PR as shown in Figure 4.6. The pulse receiver outputs the waveform of the pulse echo onto a 4 channel Tektronix TDS 5054 500MHz 5GS/s digital phosphor oscilloscope. The ultrasonic is rectified and enveloped as shown in Figure 4.7 to improve accuracy. The height of the liquid is given by the following

equation;

$$h = c_r \times \frac{\Delta t}{2}; \quad 4.1$$

, where h is the height of the liquid (m) , c_r is the speed of sound in liquid phase for refrigerant R134a and Δt is the time difference between the peak when signal was sent and received as demonstrated in Figure 4.7.

4.1.5 Pulse and dc power supplies

For the application of dc high voltage, a Glassman high voltage power supply, model PS/ER50R06.0-11 was used as shown in Figure 4.8. For dc applications a $4M\Omega$ protection cylindrical resistor is used.

Pulse high voltage applications are also studied since the power consumption can be minimized. The pulse method may be able to impose higher electric fields than dc method since higher breakdown voltage can be achieved. Modifications of an ignition coil type high voltage pulse power supply (Kim and Chang, 2005) was made in order to increase the power supply efficiency due to impedance matching losses.



a) b)
Figure 4.6: Ultrasonic Panametric instrumentation a) Pulser receiver and b) 10MHz ultrasonic transducer

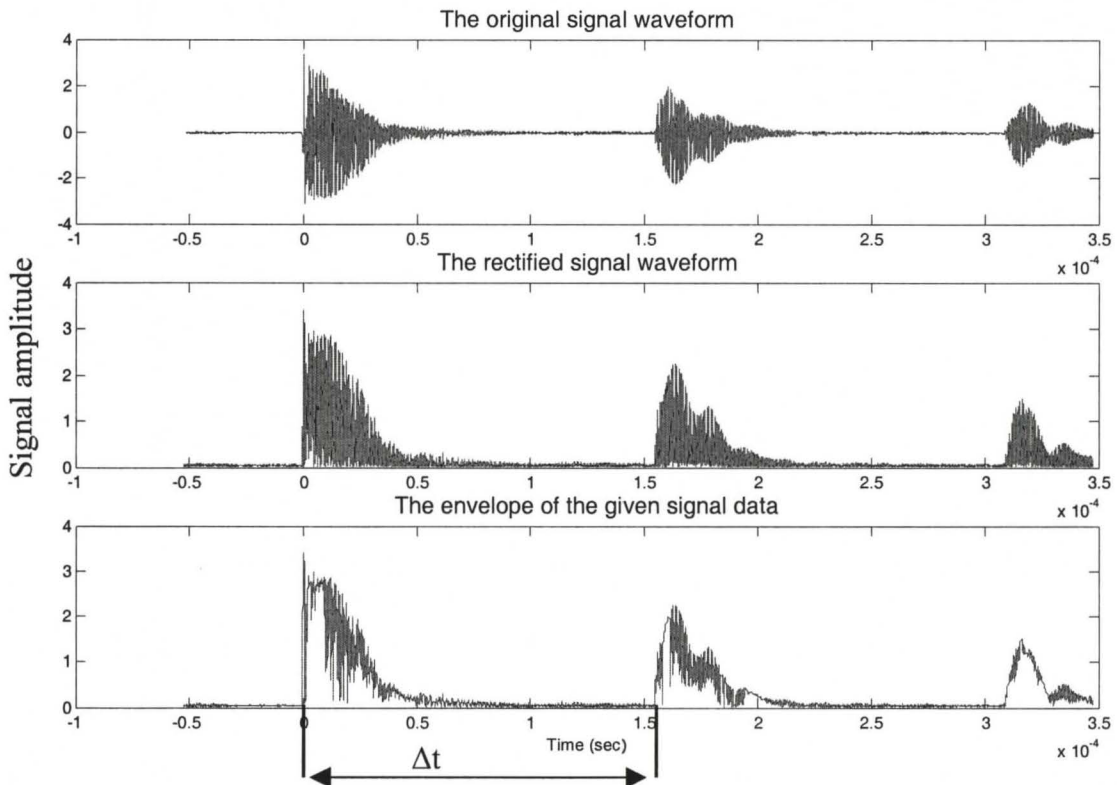


Figure 4.7: Typical ultrasonic waveform signal analysis a) raw signal b) rectified signal and c) envelope signal

4.1.5.1 Pulse power supply

The original ignition coil type pulse high voltage power supply (Chang et. al. 2003) consists of a dc low voltage regulated power supply, a function generator, a trigger circuit and an ignition coil as shown in Figure 4.9. There are two main circuits: astable and monostable that can be used with the 555 timers. Astable produces square waves with set frequencies depending on the selected resistor and capacitor in the circuit. The other method for 555 timers is monostable, which produces a single pulse when triggered. For the present case, since the optimum frequency is unknown, a monostable method was tested in the frequency range of 50-200Hz where the trigger was the function generator.

The modified pulse power supply uses the same method of generating a high voltage pulse but with some minor changes. The schematic is shown for the modified pulse power supply in Figure 4.10. The 555-timer is replaced with a MOSFET driver which is built specifically to increase rise-fall time in order to minimize losses across the MOSFET which can result in heat dissipation and can ultimately lead to burn out of MOSFETs. The product of the voltage and current give the instantaneous power dissipated in the device as shown in Figure 4.11. The heat energy developed over the switching period is the summation of the power multiplied by the time-values, which is represented by the area under the power curve ($\text{area} = \text{power} \times \text{time}$). The average power loss is the sum of the energies multiplied by the frequency of the switching. Therefore it is desired to minimize this loss for large frequency application since the losses are proportional to the frequency.



Figure 4.8: Glassman high voltage for dc applications

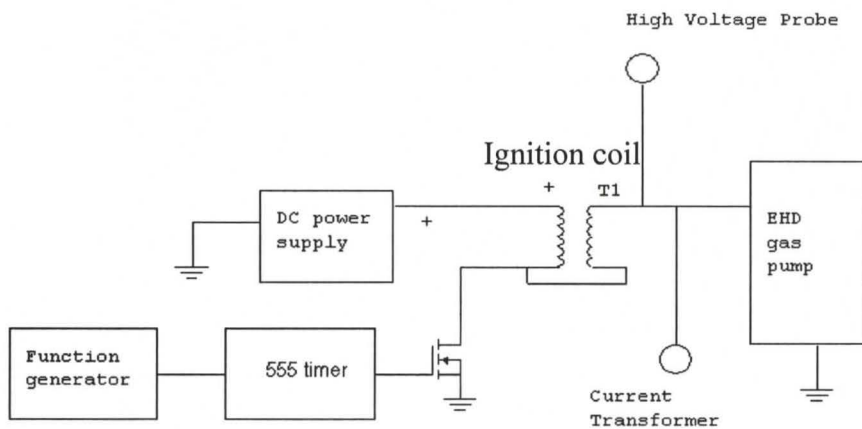


Figure 4.9: Schematic of 555-timer type pulse power supply

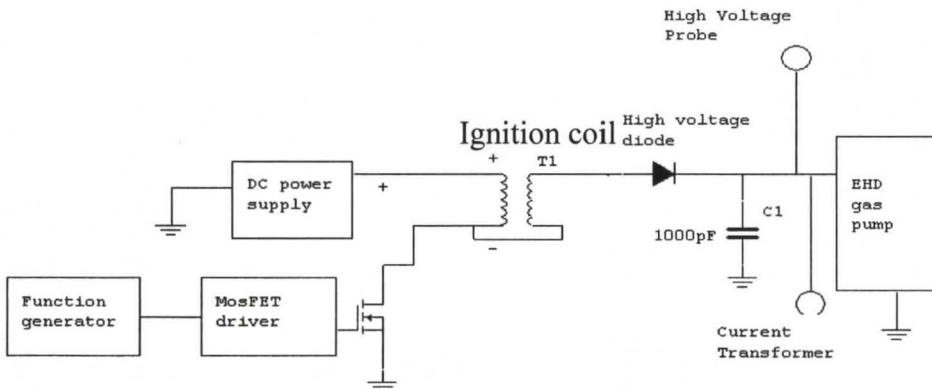


Figure 4.10: Schematic of the MOSFET driven type pulse power supply

Additional modification is done on the secondary side as a high voltage diode is placed after the ignition coil and a charging capacitor is also connected as shown. The purpose of the high voltage diode is to have a one directional current flow depending on the polarity so that the current does not oscillate, instead it would be ideal to have the current flow in one direction at all times. The charging capacitor will keep this current flow in the desired direction for a longer time and then discharge.

High voltage pulse application will be applied to an electrode with ground housing and polyethylene wick in between. This high electric field strength is desired to have an influence on the fluid and increases the flow rate.

Since it is difficult to physically see any effects that the pulse power supply may have on the evaporator, it is necessary to test the two power supplies on an arbitrary load to test the efficiency of the designed pulse power supply.

A wire-rod type EHD gas pump (Komeili et. al., 2005) is used to physically evaluate the efficiency of the pulse high voltage power supply. The EHD gas pump is shown in Figure 4.12. The motivation is to generate airflow from this gas pump and optimize the efficiency of the pulse power supply in order to apply it to the capillary evaporator. Although the geometry and the working fluid are different, higher power efficiency means more power is transferred to the load with the least amount of losses. Having a larger power delivered from the ignition coil translates to a higher electric field since power is the integral of electric field cross magnetic field.

It is now necessary to test both pulse power supplies in order to select the most efficient design to be used towards the application of the EHD-ECE.

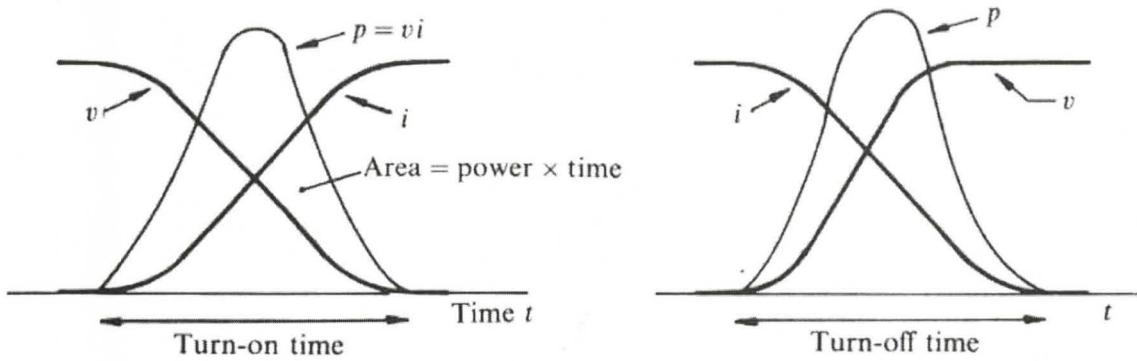


Figure 4.11: Typical power loss and heat generation across the MOSFET due to switching losses

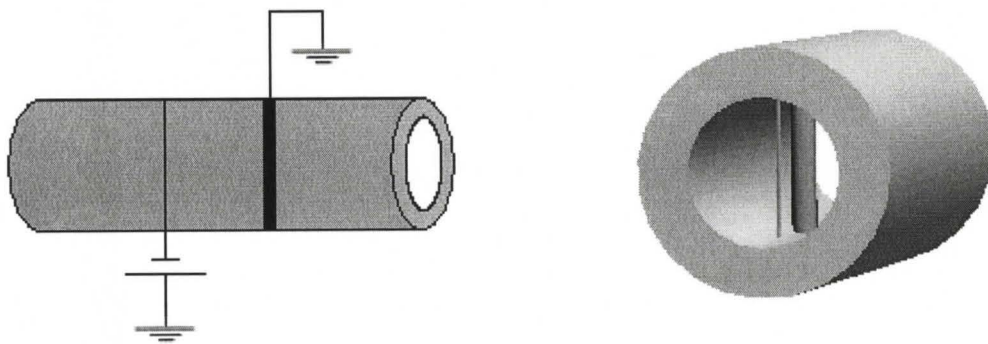


Figure 4.12: EHD gas pump used to test pulse power supply

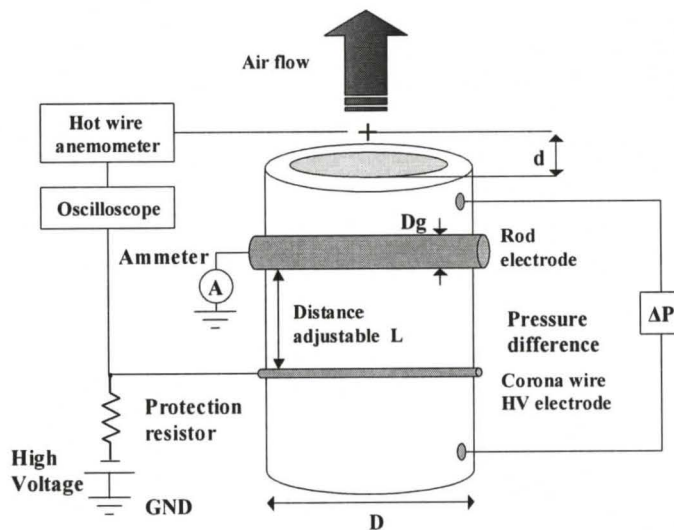


Figure 4.13: Schematic of EHD gas pump

4.1.5.2 Experimental apparatus EHD gas pump

This section discusses tests performed using an EHD gas pump to evaluate the performance of the pulse power supply (PP-supply). The EHD gas pump is chosen for optimization of the PP-supply, as the gas pump is simpler to understand, as it is a single-phase device.

Although the EHD-ECE is two-phase and the two devices have different geometries this design of the pulse power supply will be beneficial to the EHD-ECE as well. The general reduction of stresses on the components, for example reducing heating across the MOSFET is still favored for the final application. The theory discussed in chapter 3 is still appropriate for the final application since high electric fields are desired which is one of the driving forces for the gas pump.

The gas pump is placed inside an open ended rectangular Acrylic environmental chamber (80cm x 80cm x 30cm) to reduce any surrounding interference, where the details of the experimental set up is shown in Figure 4.13. Simple DC high voltage tests were conducted to determine the optimum geometry, and then the existing pulse power supply was tested on the optimum geometry, followed by tests using the modified PP-supply. The grounding electrode is connected to a multimeter (Fluke 187) then to ground. A hot wire anemometer (Dantec 55M and Heavy duty hot wire CFM-Thermo-anemometer) was placed at the exit of the EHD gas pump to measure airflow velocity. The digital oscilloscope (Tektronix TDS5054) is used to measure the voltage output from the anemometer as well as the applied voltage to the EHD gas pump. Experiments are conducted for the dc case for three pipe diameters (6.5mm, 10mm and 20mm), three rod

diameters (1.5mm, 2.2mm and 3.1mm) and three different electrode distances (electrode distance/pipe diameter =0.63, =1 and =1.16), where the wire electrode diameter was kept constant ($d_w=0.24\text{mm}$). The optimum geometry was found to be a pipe diameter of 20mm, a ground rod diameter of 3.1mm and an electrode distance/pipe diameter =1.16. The velocity measurement for the two polarities is shown in Figure 4.14 for the applied power.

4.1.5.3 Pulse applied voltage results

The existing 555-timer pulse power supply was tested and could not generate any airflow due to the waveform of the secondary current as shown in Figure 4.15. Since discharge current is very important in the success of generating airflow, we can see the main problem is from the secondary current. In reality the air gap in the electrode EHD gas pump acts as a capacitor of some unknown value, therefore the current across this is

$I = C \frac{dV}{dt}$, where C is the capacitance of the EHD gas pump and $\frac{dV}{dt}$ is the change in the

secondary voltage with respect to time. The rise of the voltage until its peak will result in positive current and when the voltage is dropped this current will be reversed, this pattern will reoccur again at the voltage ripple. Therefore the current in the secondary side is flowing in one direction and then being reversed and so the pump does not see any real current. This reversal current is also referred to as reflected current.

This is the main reason for putting a high voltage diode on the secondary side, this diode insures that the current is unidirectional only and therefore there is no reverse current back to the coil. A charging capacitor, shown in Figure 4.10, takes time to charge

and is shown that no secondary current is present until the capacitor is charged as shown by the secondary voltage as shown by Figure 4.16. The capacitor then discharges and current is allowed to flow into the gas pump, it should be observed that there is no ripple for the secondary current. The modified circuit also has some modifications on the

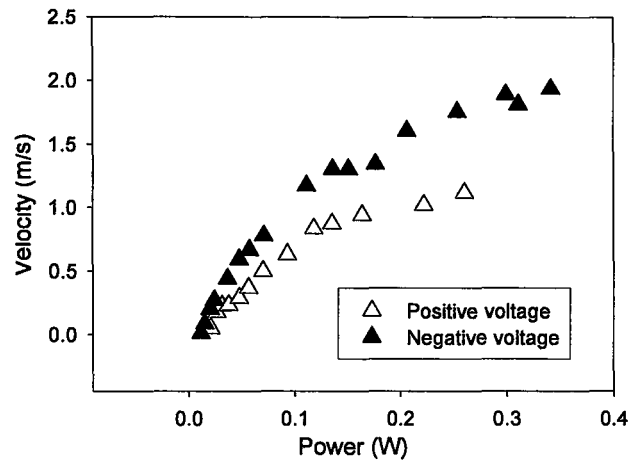


Figure 4.14: Effect of polarity on central axis velocity at the pump exit with applied power for $L=12.6$, $D=20\text{mm}$, $D_g=3.1\text{mm}$ and $d_w=0.24\text{mm}$ for dc case

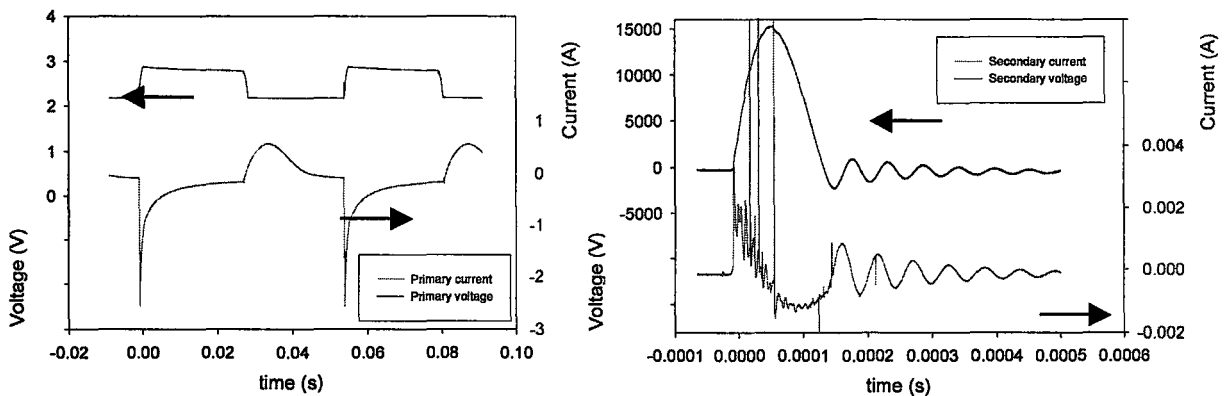


Figure 4.15: Primary and secondary side waveforms of the 555-timer circuit under 20Hz frequencies

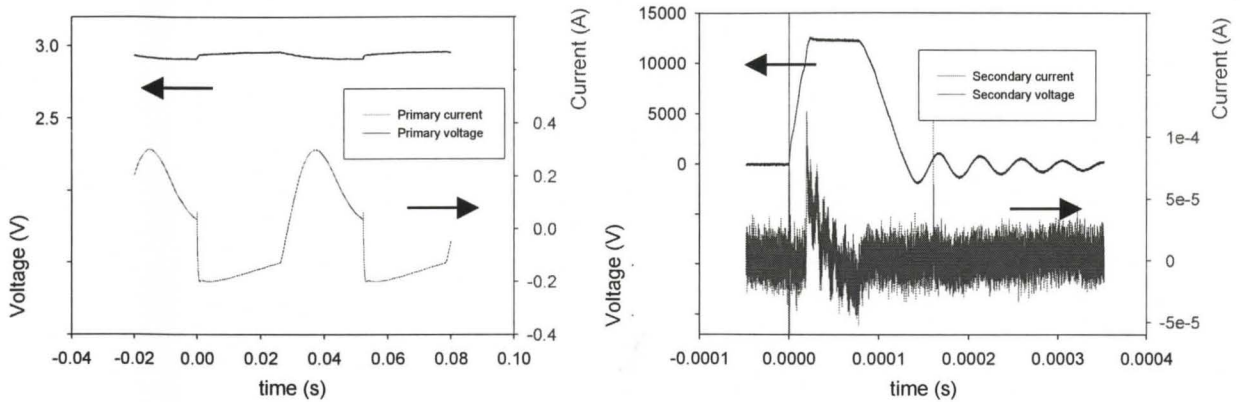


Figure 4.16: Primary and secondary side waveforms of the MOSFET driven circuit for 20Hz frequency

primary side in order to reduce any stress on the primary power supply. As shown by the primary waveform for the switching of the current, therefore very large spikes up to -2.5A, that could damage the primary dc power supply as it can only withstand up to 3A absolute. From the modified circuit it can be observed that the charging current is still the same order whereas the drop in voltage is only to -0.2V and the voltage is not switching as much as before. Both of these improvements are methods to reduce strain and stress on the dc power supply. The modifications generated 1m/s central axis velocity for the specified waveform as shown in Figure 4.16. Efficiency tests were done for the two different types of circuits for three different frequencies as shown in Figure 4.17. For all cases the input from the primary is 3V and the current varies with frequency. The efficiency is based on power output divided by power input for a pulse method, which accounts for frequency effects. The efficiency is increased substantially as frequency is increased and it can be seen that the maximum efficiency for the 555-timer pulse power supply is approximately 2% and hence no airflow is generated whereas a much higher efficiency of approximately 46% is observed for the new MOSFET driven power supply.

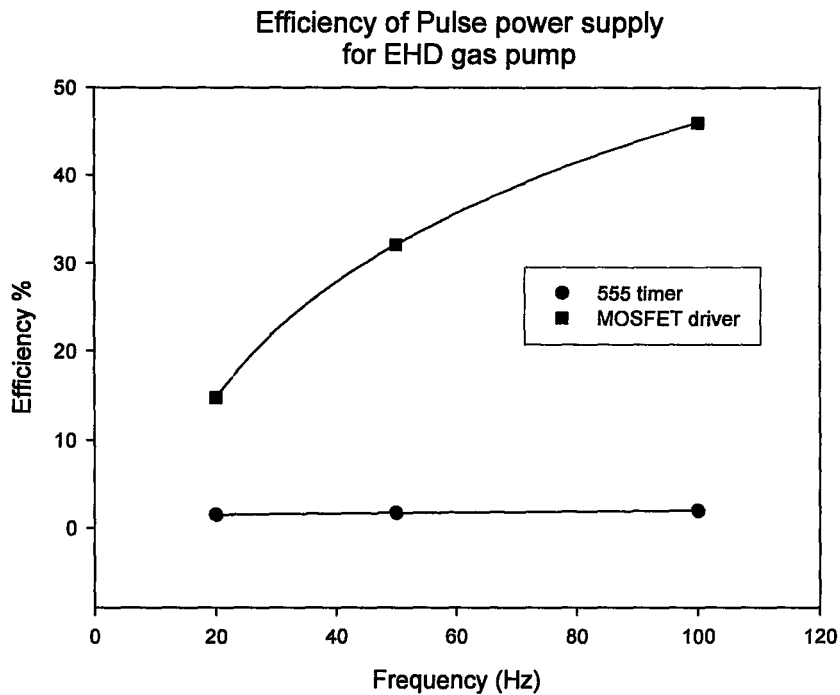


Figure 4.17: Efficiency test with respect to frequency for the two comparing pulse power supplies

4.2 Experimental procedure

The experimental procedure is outlined below followed by an outline of a range of test parameters. The initial start-up consists of the following steps:

- The rig is charged until the wick inside the evaporator is wetted via the charging valve. An ultrasonic transducer under the liquid tank and the liquid reservoir tank is used to confirm the volume of liquid Refrigerant in the tanks as shown by Figure 4.2. The sight tube is used to assist in liquid level analysis.
- The startup of this experiment takes some time in order to obtain all of the condensed liquid from the condensate collection tank to the liquid reservoir tank with the least amount of vapour trapped in the liquid reservoir tank. In

order to achieve this, ice is placed on top of the liquid reservoir tank and heat is applied to the condensate collection tank while the valve is closed just after the evaporator exit. The process of applying heat to the condensate collection tank increases the pressure as the temperature increases and so the addition of heat was stopped when the pressure reaches around 850 kPa for safety reasons. The temperature and the pressure are allowed to drop and heat is applied again in order to remove all the liquid in this tank. This process is repeated until all or most of the liquid is removed and the pressure is allowed to be dropped until room temperature is achieved.

- The valve between the condensate collection tank and exit temperature is released and allowed the system to reach steady state. This steady state is reached when the pressure drop across the evaporator is stabilized and then the valve of the return line is closed.
- The measurements of the liquid levels are made as initial liquid levels.
- The data acquisition is able to record temperature in degrees Celsius and pressure difference in terms of voltages.
- The flow rate is set to 5 L/min in the plastic tubing wrapped around the condensate collection tank.
- The heat input was applied to the evaporator by adjusting the Variac to the desired level.
- Liquid level of the condensate collection tank and reservoir tanks are made at 5 min intervals, whereas the liquid tank is recorded in the initial state and the

liquid line measurements are taken near the end of the experiments between the liquid tank and the liquid reservoir tank to monitor that the pipe is full of liquid.

- The system pressure is also monitored every 5 minutes.
- Voltage is applied when the pressure reaches steady state. Different voltages are applied for different polarity based on the current voltage characteristics and an on-off-on voltage is implemented for the dc case. In the case of the pulse application, one polarity is turned on while changing frequencies to see the effect then turned off and the same is done with the reversed polarity.

The following test matrix details the testing that was done for the existing EHD-ECE and is given by table 4.1.

Table 4.1: Test matrix for the EHD-ECE experiment

Water cooling on condensate collection tank	Heat input (W)	Applied voltage		Pulse power supply frequency (Hz)	Purpose
		<i>Dc voltage (kV)</i>	<i>Pulse power supply (kV)</i>		
No	0-70	No	No	Na	
Yes	0-80	No	No	Na	Condensate effect
Yes	0-80	0	-10	5	Voltage/polarity effect
		-2.5		50	
		-5		200	
		5	5	5	Frequency effect
				50	
				200	

Chapter 5

THERMAL CHARACTERISTICS OF AN EHD ENHANCED CAPILLARY EVAPORATOR

This chapter will describe the experimental results of the work and analyze the results in order to have a better understanding of the EHD-ECE device.

5.1 Characteristics of capillary evaporator without condensate collection tank water cooling: Thermal, pressure difference, system pressure, flow rate

A typical set up transient behavior for the EHD enhanced capillary evaporator (EHD-ECE) characteristics at zero applied voltage without water cooling on the condensate collection tank (CC-tank) are shown in Figure 5.1, where the CC-tank was cooled by natural convection of air. This shows the temperature transient behavior of the upstream liquid inlet T_{inlet} , EHD-ECE wall T_{wall} , downstream vapour T_{exit} and the pressure difference across the evaporator ΔP identified in Figure 4.1. Since the CC-tank is cooled by natural convective air, a slight increase in the liquid temperature inlet is observed.

The steady state EHD-ECE temperature characteristics are shown in Figure 5.2 as a function of heat input. There is no significant change in the liquid temperature at the inlet once steady state is achieved as expected and the vapour temperature at the ECE exit increases with increasing heat input. The EHD-ECE evaporator wall temperature increases significantly with increasing heat input, where the maximum of 70W is used instead of the desired 80W since the melting temperature of the polyethylene (PE) wick is around 150°C.

Figure 5.3 shows the pressure difference per ECE device, system pressure and the liquid flow rate as measured directly from the ultrasonic transducer. Although an ultrasonic system was used at the up-stream liquid reservoir tank and down-stream CC-tank only the CC-tank vapour flow rate measurements are used. The reason that the liquid reservoir tank was not used in analysis of the EHD-ECE is because it sometimes had some vapour trapped inside the tank. However as long as the liquid level is above the halfway part of the tank from start-up until the end of the experiments, which will ensure that dryout will not occur in the evaporator, there is no cause for concern. Yet the measured values for the liquid level reservoir tank are ignored since the liquid is allowed to travel upward to the condensate return as observed by the sight tube due to the trapped in the liquid reservoir tank. This will affect the liquid level measurements in the liquid reservoir tank and give inaccurate results.

There are two other ultrasonic transducers used, one at the liquid line between the liquid tank and the liquid reservoir tank and the other at the liquid tank itself. These two were used to monitor the liquid level to ensure no dryout and that there is always a full pipe between the two liquid tanks as well as a full liquid tank under the evaporator.

Figure 5.3 shows a significant increase in the system pressure as heat is applied. There is a relative low flow rate observed here for the no water cooling of CC-tank as expected from the lower driving force between the EHD-ECE and CC-tank due to less natural convection of vapour by $(T_{\text{exit}} - T_{\text{inlet}})$ and less vapour condensation in CC-tank. The pressure difference non-monotonically increases with increasing heat input then slightly decreases as expected due to increasing liquid flow.

Figure 5.4 is the calculated vapour flow rate based on the measured liquid flow rate, system pressure and exit temperature. When the vapour temperature is at or below the saturated temperature, the refrigerant is subcooled and no significant vapour flow rate is observed. Once the vapour temperature exceeds the saturate temperature, vapour flow is observed. The importance of this graph is discussed later in this chapter.

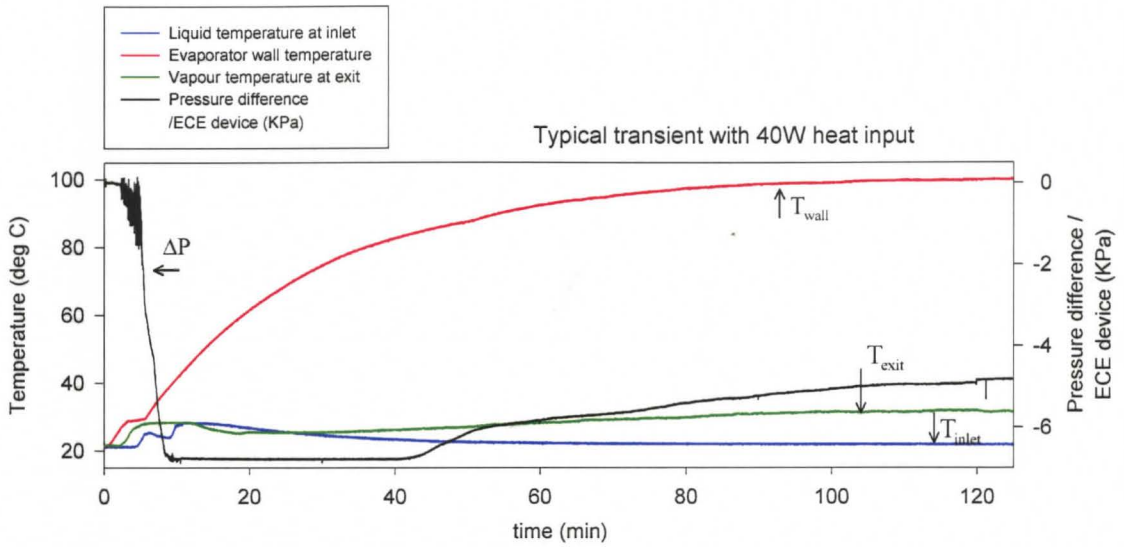


Figure 5.1: Typical transient behavior of liquid, vapour, wall-temperature and pressure difference/ECE device for EHD-ECE for no water cooling on condensate collection tank for heat input=40W and $V=0$

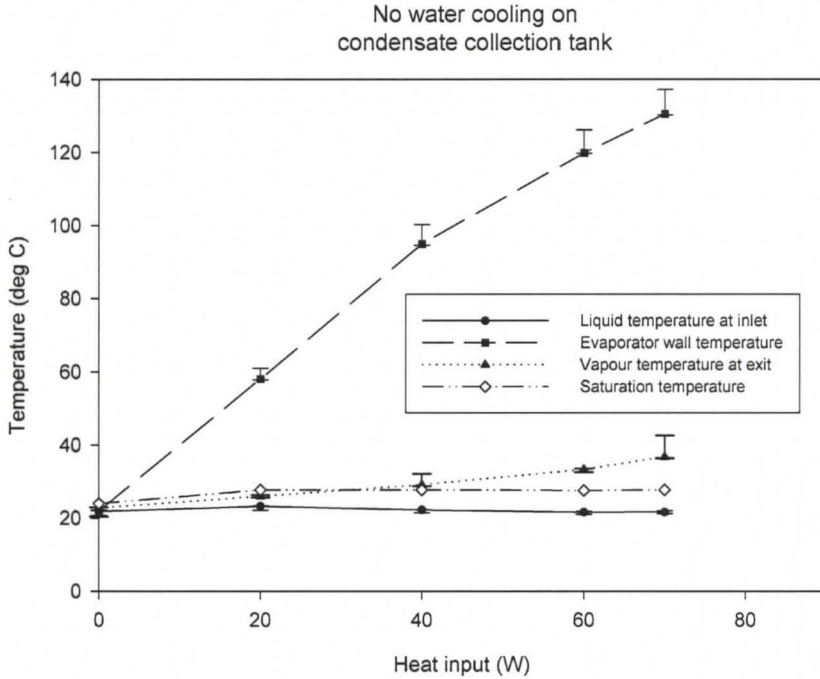


Figure 5.2: Steady state liquid, vapour and wall-temperature for EHD-ECE for no water cooling on condensate collection tank as a function of heat inputs and $V=0$.

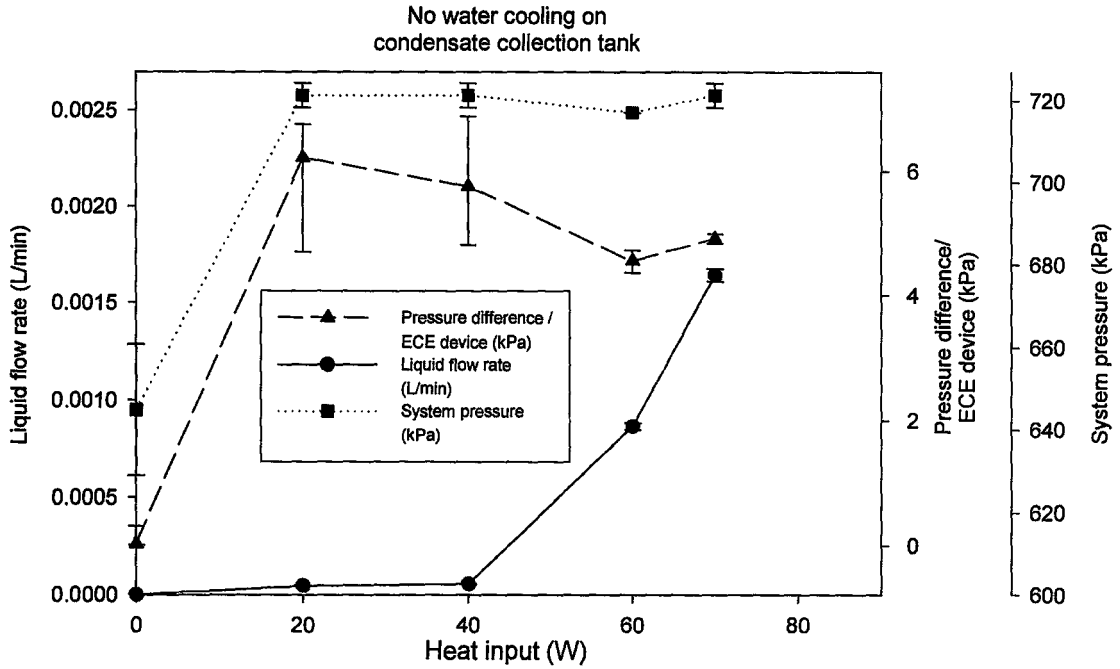


Figure 5.3: Steady state pressure drop, liquid flow rate and system pressure measurements for EHD-ECE for no water cooling on condensate collection tank as a function of heat inputs and $V=0$.

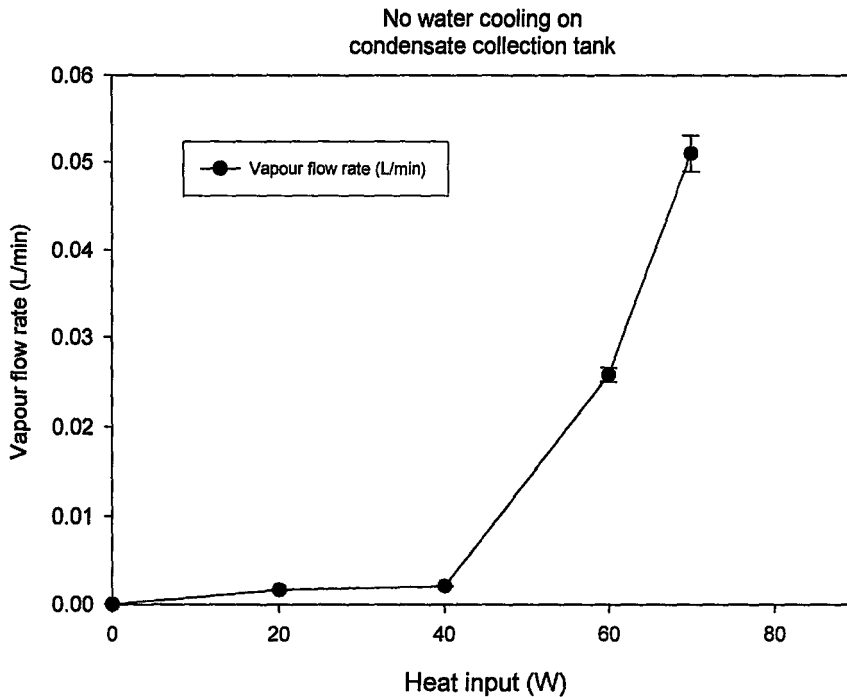


Figure 5.4: Steady state vapour flow rate measurements for EHD-ECE for no water cooling on condensate collection tank as a function of heat inputs and $V=0$.

5.2 Characteristics of capillary evaporator with condensate collection tank water-cooling: Thermal, pressure difference, system pressure, flow rate

A typical transient behavior for the EHD-ECE characteristics at zero voltage applied with water cooling on CC-tank is shown in Figure 5.5 for an input heat of 40W, where the CC-tank was cooled by outside ground water at an average flow rate of 5 L/min. The difference from Figure 5.1 and Figure 5.5 is the temperatures of the evaporator wall and the vapour temperature at the exit increase faster in Figure 5.1; this is due to the absence of the cooling water. The liquid temperature at the inlet also increases initially for Figure 5.1 whereas by having the water cooling, the temperature at the inlet does not change.

Figure 5.6 shows the averaged steady state temperatures observed for EHD-ECE at $V=0\text{kV}$ as a function of applied heat. Due to the CC-tank water-cooling, 80W heat input was applied and the evaporator wall was carefully monitored so that the melting point of the PE wick was not attained. The vapour temperature at the exit is actually higher than the no cooling water case as the system pressure becomes lower as shown in Figure 5.7.

Figure 5.7 shows the system pressure, pressure difference between the ECE device, and the liquid flow rate measured at the CC-tank. Liquid flow rates at 0W and 20W are not shown since the temperature for these heat inputs at the vapour exit are below the saturation temperature. This may imply that due to 0W heat input and a low heat input of 20W, no evaporation occurs for these two heat inputs. There may be liquid in the vapour channel due to overcharging of the system during start up, and not high

enough heat is applied through the fins to evaporate the liquid. It was observed that in the process of charging the system, the liquid level was above the wick as observed in all cases by the sight tube before start up. This liquid level as observed through the sight tube drops as heat input was increased to 40W, 60W, and 80W.

Figure 5.5 shows that once the evaporator wall temperatures is around 26°C, there is some bubbly flow occurring in the vapour line and once the evaporator exit has reached this temperature then the pressure decreases due to the presence of vapour in the vapour line. There is an increase in temperature of the evaporator wall at $t=20\text{min}$ in Figure 5.5 which may be because the vapour grooves are actually occupied by vapour and not liquid anymore so the wall temperature will increase, this phenomena does not occur for the two cases of the 0W and 20W. Therefore if the heat input is small or not present, the condenser may be dominating and natural convection of the fluid will be transported to the CC-tank, which may act as a vacuum since the average temperatures for the vapour temperature at the exit is below the saturation temperature and the system pressure is low as seen in Figures 5.6 and Figure 5.7, respectively.

The liquid flow rate, measured by the ultrasonic at the CC-tank shows the raw data, however since the exit temperature of the evaporator is also measured, it is possible to calculate the vapour flow rate as temperature and pressure correction can be made and a more accurate measurement can be made as shown in Figure 5.8.

Figure 5.8 shows the calculated vapour flow rate at the exit based on the exit temperature and pressure measured. The source of error in this flow rate is measured by the fluctuation level of the sent ultrasonic signal in the CC-tank where there is some error

expected since there is condensation of the vapour occurring. It can be observed from the vapour flow rate that on average the flow rate increases with increasing heat input as expected.

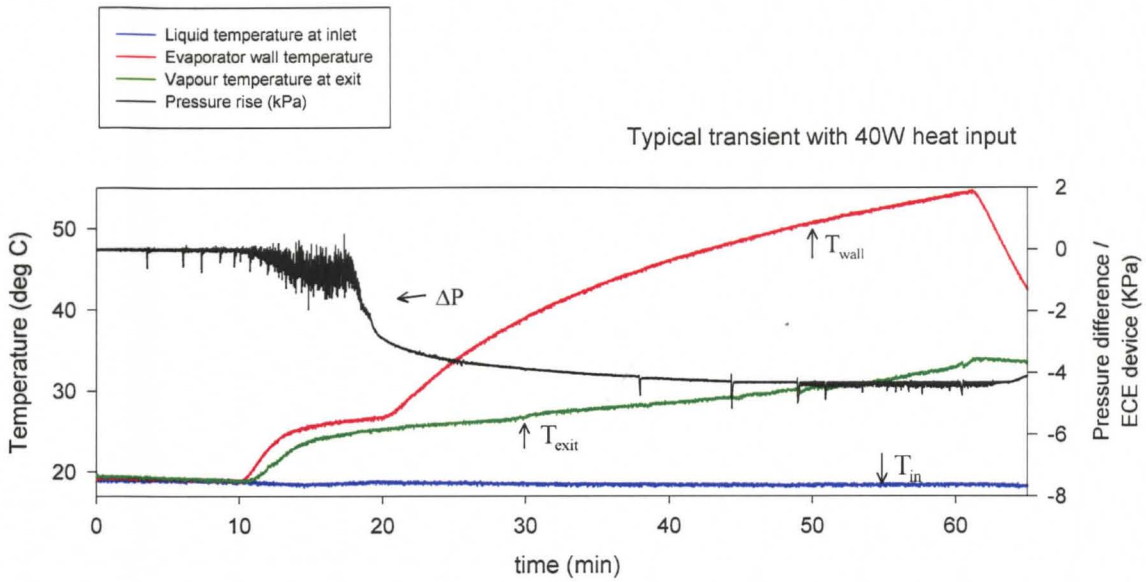


Figure 5.5: Typical transient behavior of liquid, vapour, wall-temperature and pressure difference/ECE device for EHD-ECE for water cooling on condensate collection tank for heat input=40W and $V=0$

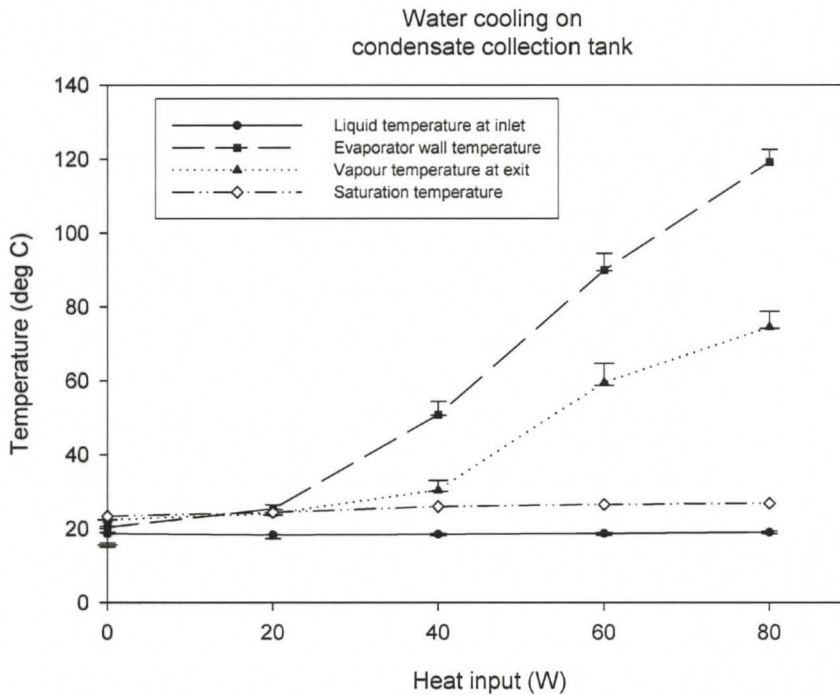


Figure 5.6: Steady state liquid, vapour and wall-temperature for EHD-ECE for water cooling on condensate collection tank as a function of heat inputs at $V=0$

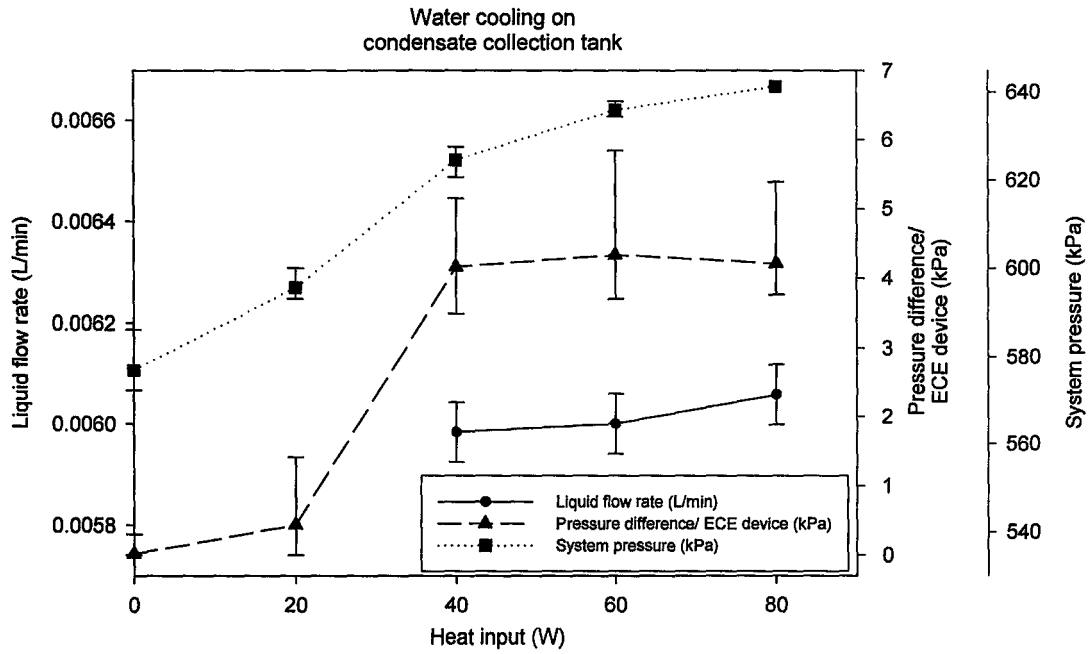


Figure 5.7: Steady state pressure difference, liquid flow rate and system pressure measurements for EHD-ECE for water cooling on condensate collection tank as a function of heat inputs and $V=0$.

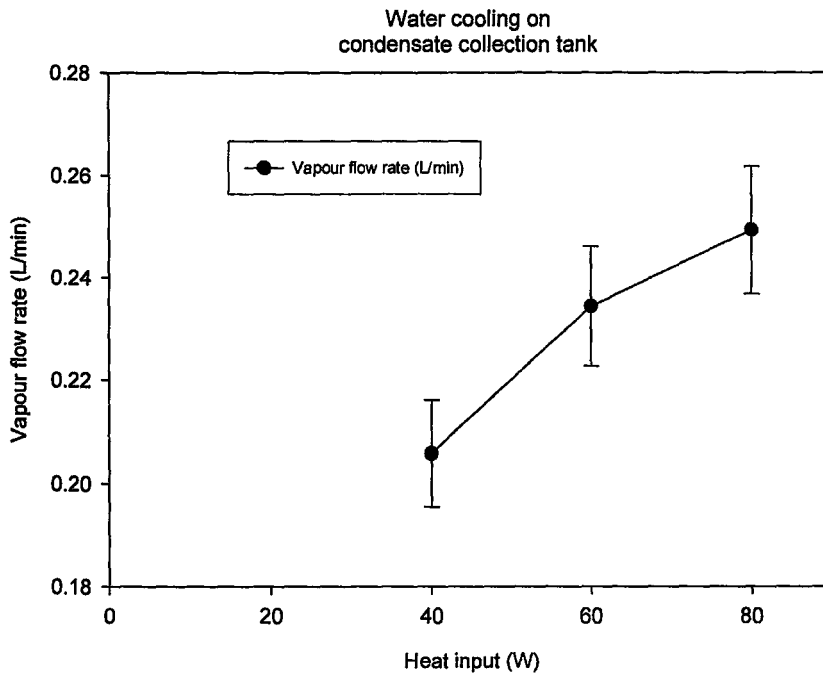


Figure 5.8: Steady state vapour flow rate measurements for EHD-ECE for water cooling on condensate collection tank as a function of heat inputs and $V=0$.

5.3 Characteristics of capillary evaporator with condensate collection tank water-cooling under DC high voltage: Thermal, pressure difference, system pressure, flow rate

A typical transient behavior for the EHD-ECE characteristics at applied voltage with water-cooling on CC-tank is shown in Figure 5.9 for an input heat of 60W. Voltages of -2.5kV, -5kV and 5kV are applied as shown. A typical variation of the liquid flow rate behavior is also shown in Figure 5.10. It can be seen that for the first 15 minutes any trapped vapour that is present in the CC-tank condenses and then steady state is achieved, which is when on-off dc voltage is applied. The dc voltage observes an obvious disturbance of the liquid flow rate in the on-off states.

Figure 5.11 shows the liquid at the inlet, evaporator wall and vapour at exit temperature for applied dc voltage of -2.5kV. The error bars represent temperature fluctuation and it can be shown that the error increases with increasing heat input. This error increase is due to the fact that the $V=-2.5\text{kV}$ is the first voltage applied and temperatures increase faster for higher heat inputs initially, and hence have a higher fluctuation. Again it can be shown by Figure 5.11 that for 20W heat input both the evaporator wall and vapour at the exit have temperatures near the saturation temperature and may suggest a liquid phase at the exit of the evaporator again.

Figure 5.12 shows the liquid flow rate, system pressure and the pressure difference across the ECE device for a comparison between -2.5kV and 0V applied. The system pressure difference between the two voltages as well as the pressure difference across ECE device is insignificant as shown. However a more significant effect can be

seen for the liquid flow rate and an enhancement is shown for applied voltage of -2.5kV for all heat inputs.

A higher vapour flow rate is shown in Figure 5.13 for heat inputs 40W and higher and the flow rate enhancement is shown. The non-monotonic increase of the flow rate is accounted for the fact that steady states are reached at different times between heat inputs and therefore the applied -2.5kV is made at a different time for different heat inputs as shown in the appendix and a comparison between heat inputs are difficult, and rather a comparison of flow rate for the common heat inputs, should be made to observe enhancement due to applied voltage.

Figure 5.14 shows the three temperature measurements discussed before for the case of -5kV applied. The same behavior is shown as the case of -2.5kV but with smaller error bars as the temperature is reaching a more steady state case.

System pressure, liquid flow rate and the pressure difference across ECE device for the -5kV case are shown in Figure 5.15. Again the applied voltage does not significantly affect the system pressure and pressure difference. The enhancement of the vapour flow rate is again visible for the addition of the voltage as shown in Figure 5.16 and shows flow enhancement.

The final applied voltage of 5kV for the temperature case is shown in Figure 5.17 and again the fluctuation level is decreased substantially since the temperature has reached its steady state.

No significant change is shown for the system pressure and the pressure difference across the ECE for 5kV and 0kV shown in Figure 5.18.

The vapour flow rate is again enhanced for the addition of 5kV voltage and the enhancement percentage due to this voltage as well as the case of -2.5kV and -5kV are compared in Figure 5.20.

The enhancements for the various applied voltages are shown in Figure 5.20 in terms of percentage and can be shown that for the higher heat input of 80W, the largest enhancement of 202% is observed for the larger and positive voltage of 5kV (see Appendix C for slight Polarity effect).

It can be shown that all the applied voltages enhance the vapour flow rate. The enhancement is relatively large for the 80W case and is promising for higher heat inputs. The case of the 80W might demonstrate dryout more effectively. It is suggested that due to this large heat input, the evaporator is near dryout due to the low vapour flow rate, however once voltage is applied the flow rate enhanced significantly. This suggests that the presence of the electric field may raise the gas-liquid interface, pushing the liquid closer to the heated surface and therefore increasing evaporation and avoiding dryout (see Appendix C).

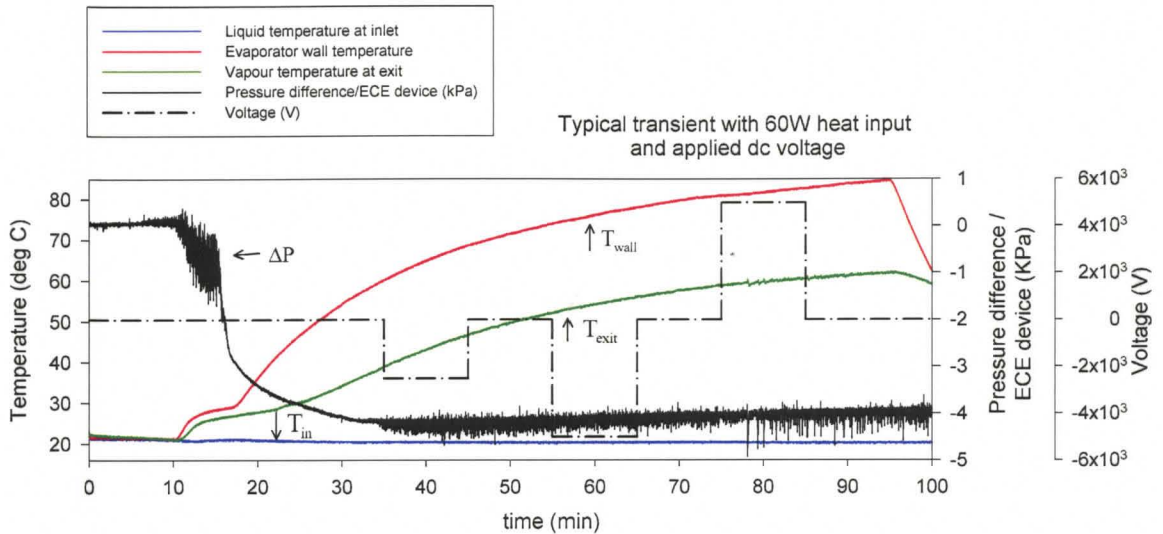


Figure 5.9: Typical transient behavior of liquid, vapour, wall-temperature and pressure difference for EHD-ECE for water cooling on condensate collection tank for heat input=60W at dc voltage applied

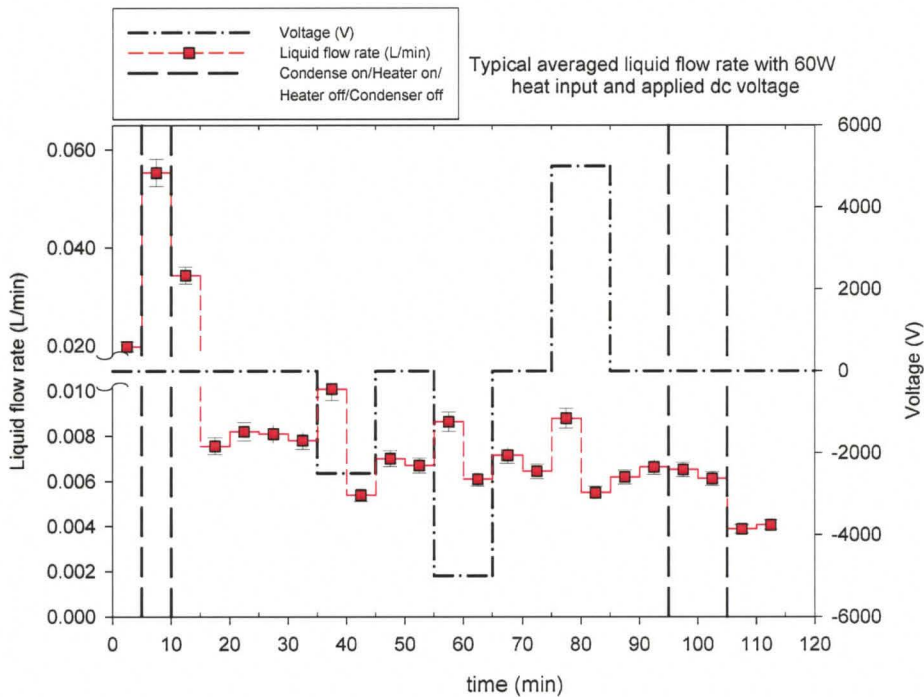


Figure 5.10: Typical variation in behavior of liquid flow rate averaged over 5 min for EHD-ECE for water cooling on condensate collection tank for heat input=60W at dc voltage applied

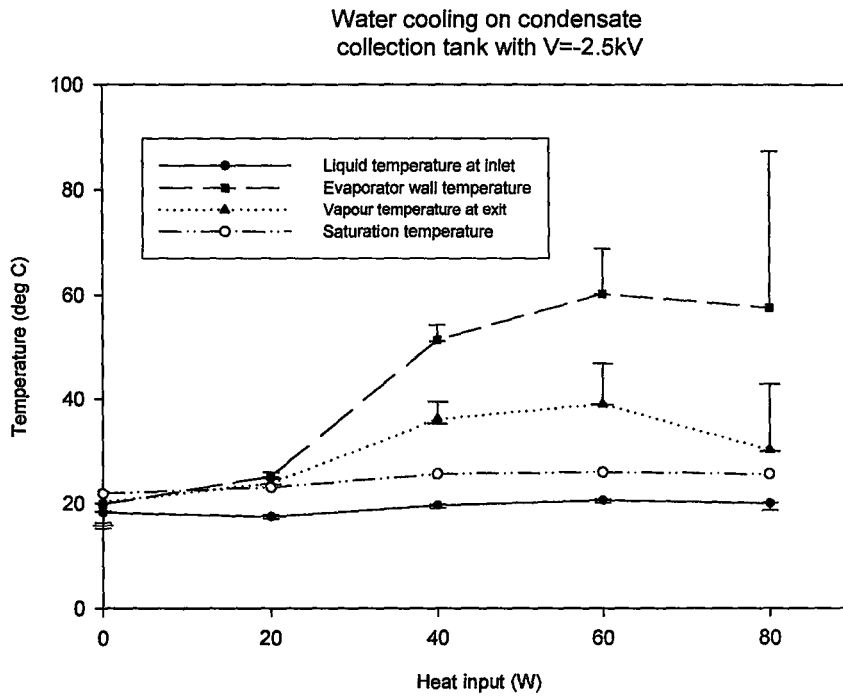


Figure 5.11: Steady state liquid, vapour and wall-temperature for EHD-ECE for water cooling on condensate collection tank as a function of heat inputs at $V= -2.5kV$. The room temperature was 20-22°C and inlet cooling water 15-16°C

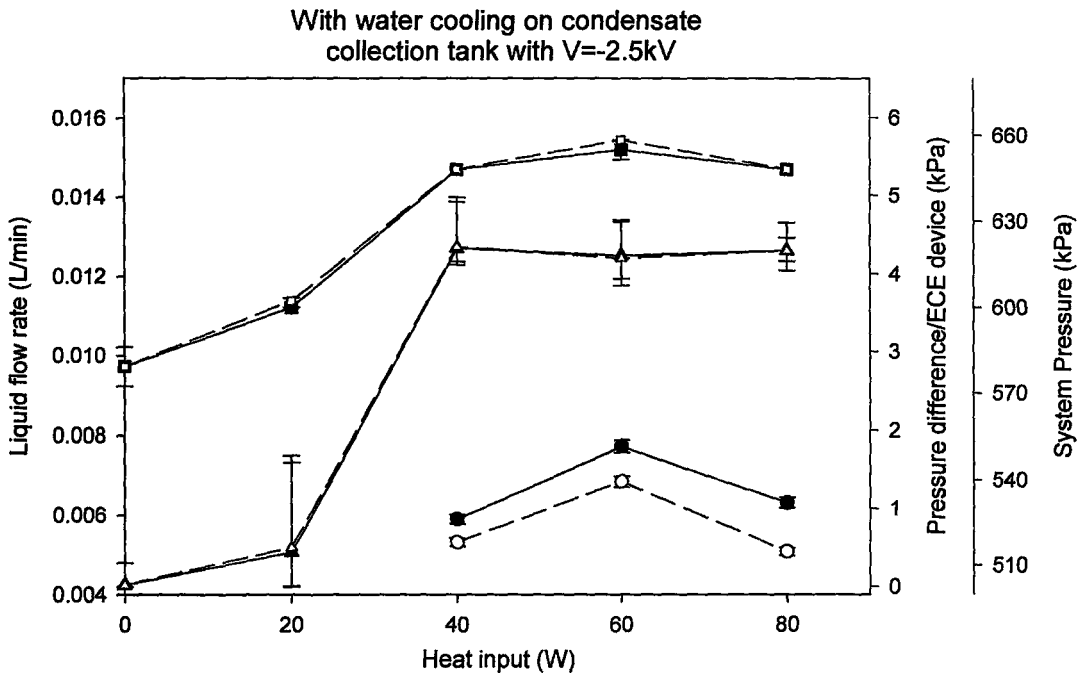
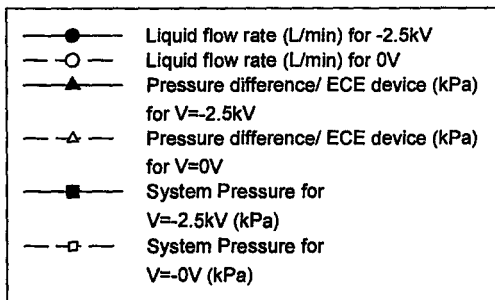


Figure 5.12: Steady state pressure difference, liquid flow rate and system pressure measurements for EHD-ECE for water cooling on condensate collection tank as a function of heat inputs and $V=-2.5kV$.



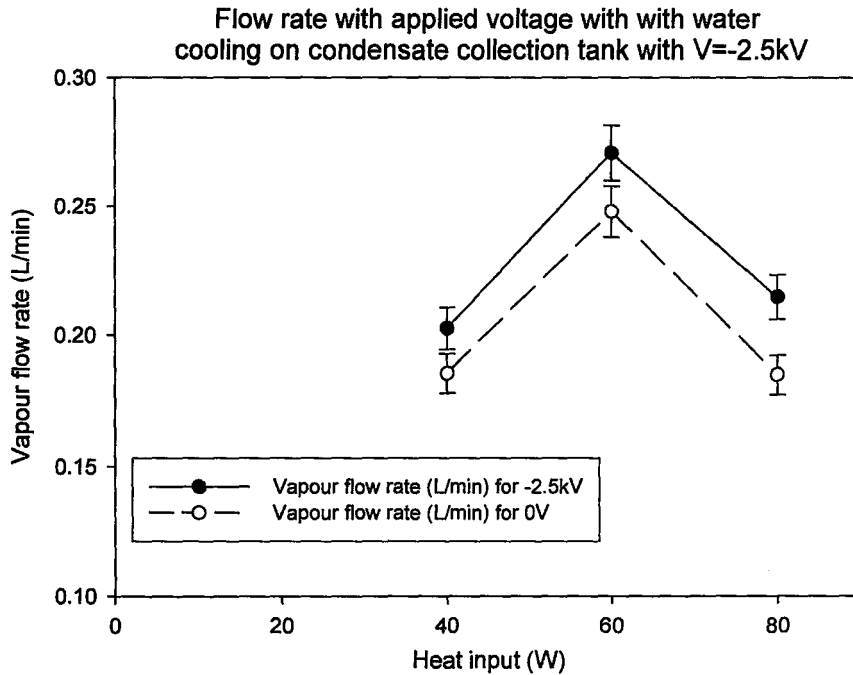


Figure 5.13: Average flow rate in ECE with water cooling on condensate collection tank for various heat inputs comparing -2.5kV applied voltage and 0V. The room Temperature was 20°C-23°C and cooling water average temperature was 14°C-16.5°C.

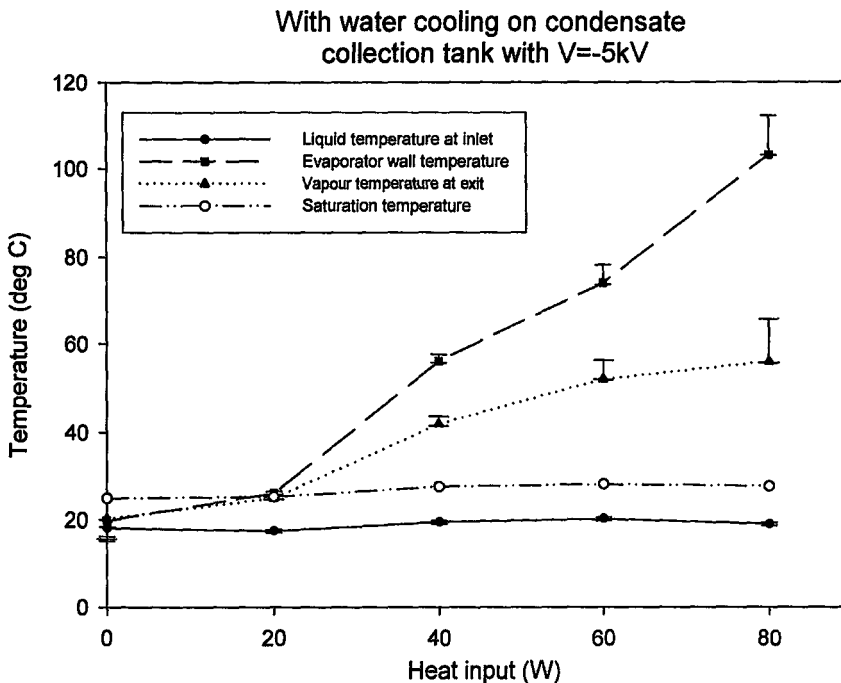


Figure 5.14: Steady state liquid, vapour and wall-temperature for EHD-ECE for water cooling on condensate collection tank as a function of heat inputs and $V= -5kV$. The room temperature was 20-23°C and inlet cooling water 14-16.5°C.

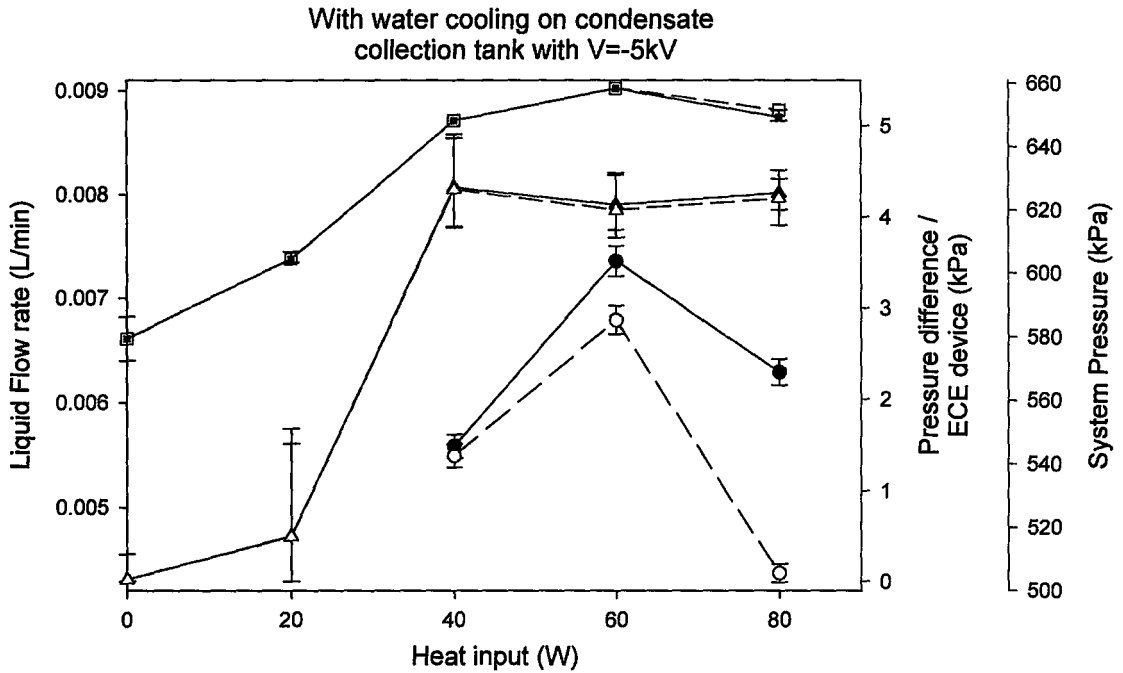
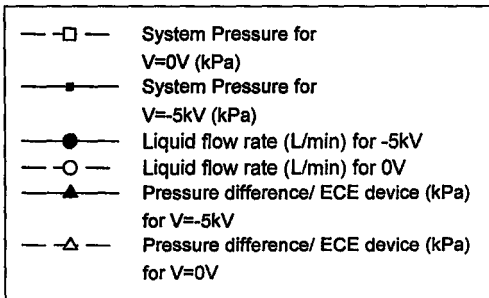


Figure 5.15: Steady state pressure difference, liquid flow rate and system pressure measurements for EHD-ECE for water cooling on condensate collection tank as a function of heat inputs at $V=-5kV$



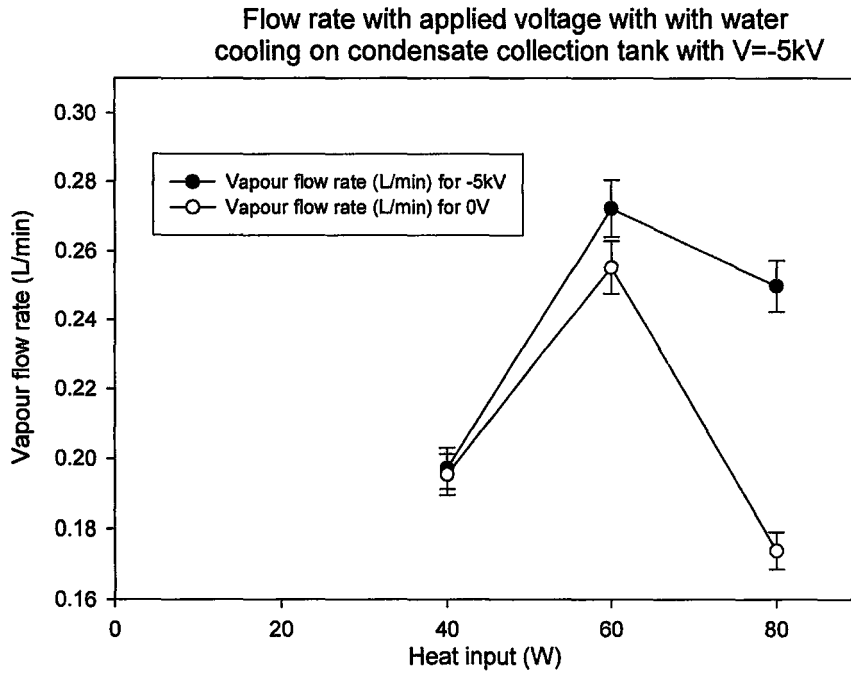


Figure 5.16: Average flow rate in ECE with water cooling on condensate collection tank for various heat inputs comparing -5kV applied voltage and 0V. The room average temperature was 20°C-23°C, and average cooling water temperature=14°C-16.5°C

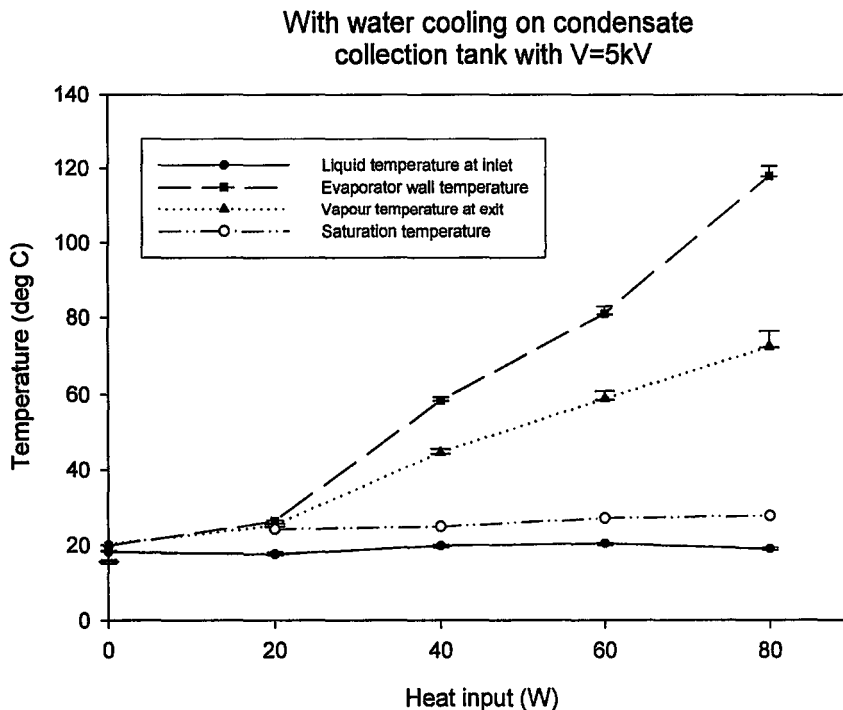


Figure 5.17: Steady state liquid, vapour, wall-temperature for EHD-ECE for water cooling on condensate collection tank as a function of heat inputs at V= 5kV. The room temperature was 20-22°C and inlet cooling water 15-16°C

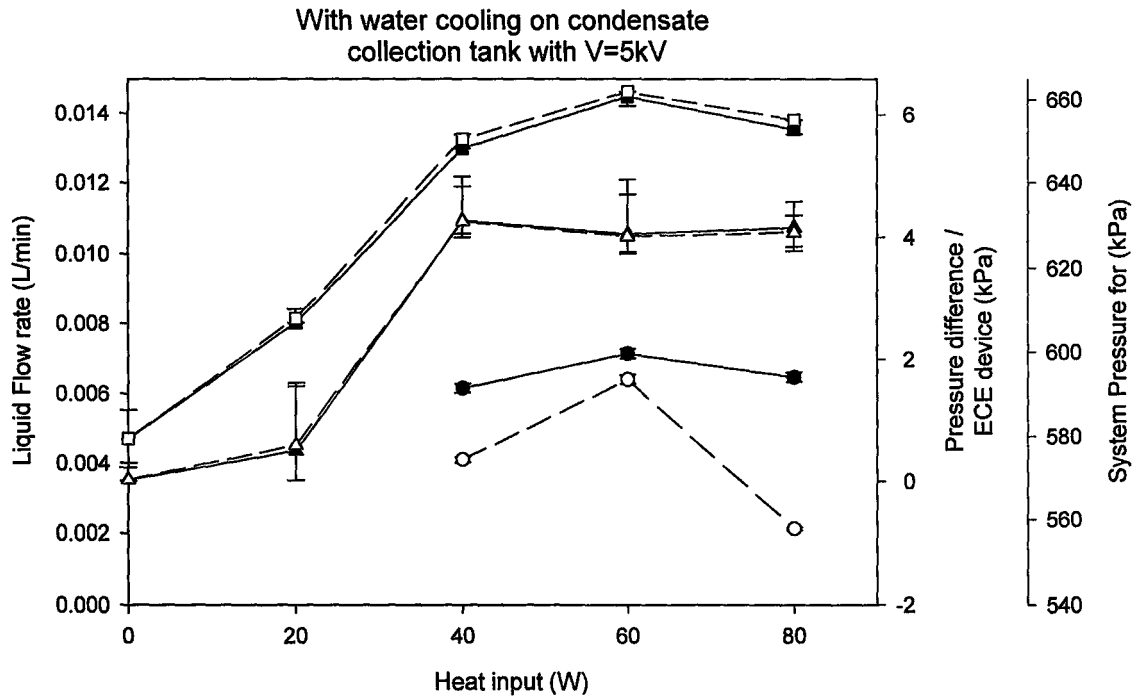
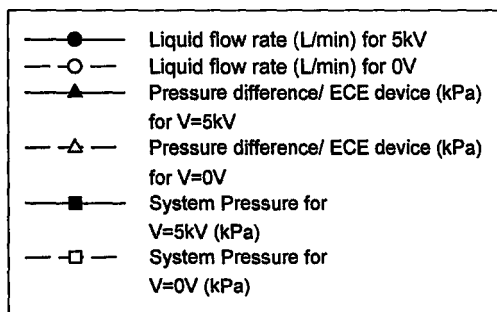


Figure 5.18: Steady state pressure difference, liquid flow rate and system pressure measurements for EHD-ECE with water cooling on condensate collection tank for various heat inputs comparing 5kV applied voltage and 0V. The room average temperature was 20°C-23°C, and average cooling water temperature was 14°C-16.5°C



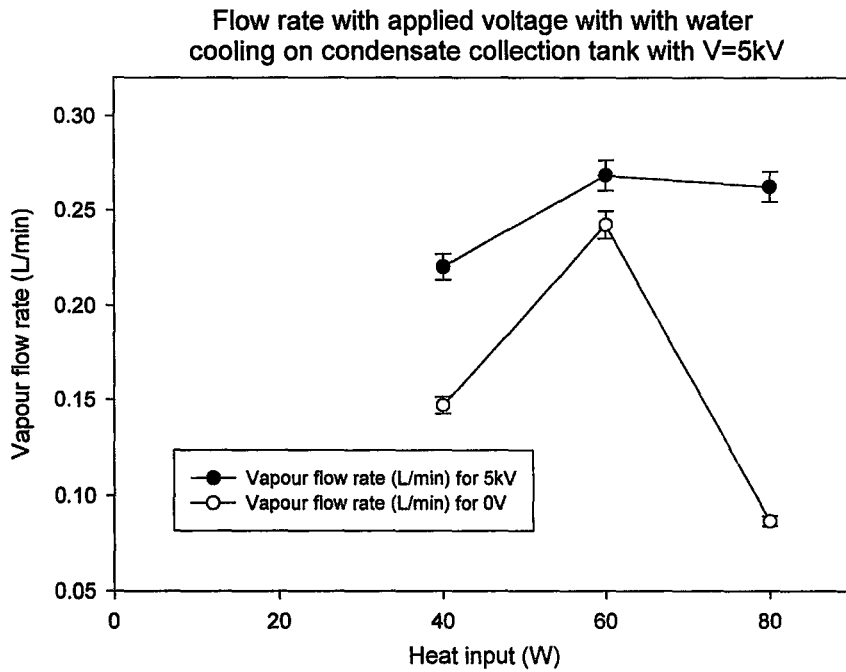


Figure 5.19: Average flow rate in ECE with water cooling on condensate collection tank for various heat inputs comparing 5kV applied voltage and 0V. The room average temperature was 20°C-23°C, and average cooling water temperature was 14°C- 16.5° C

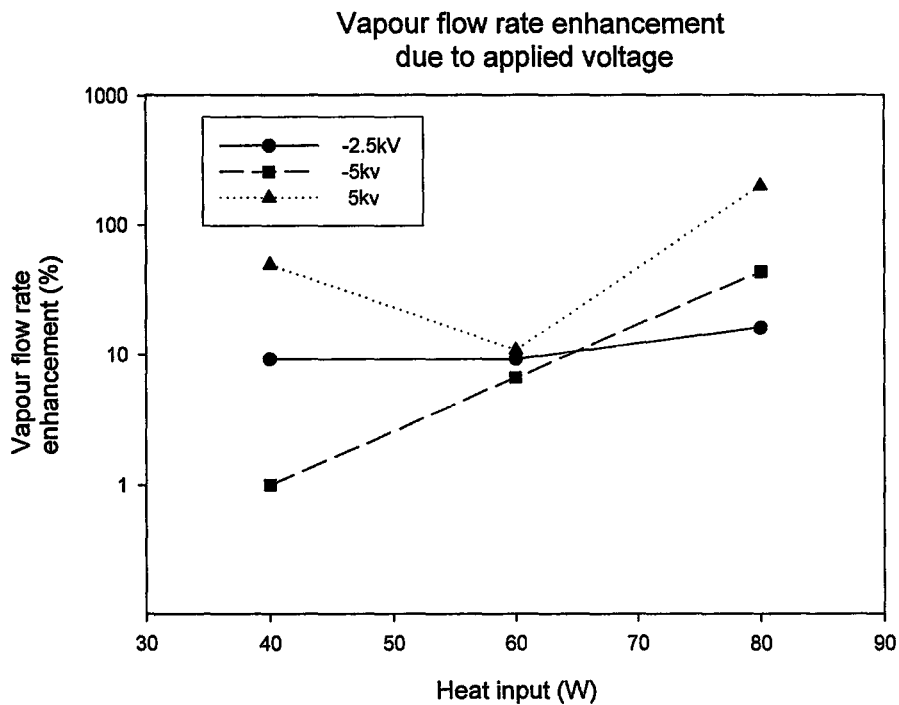


Figure 5.20: Vapour flow rate enhancement percentage in ECE with water cooling on condensate collection tank for various heat inputs comparing applied voltages.

5.4 Characteristics of capillary evaporator with condensate collection tank water-cooling under pulse high voltage application: Thermal, pressure difference, system pressure, flow rate

A typical transient behavior for the EHD-ECE characteristics for the applied pulse high voltage with water-cooling on CC-tank is shown in Figure 5.21 for an input heat of 40W. Once the pressure difference has reached close to steady state a pulse voltage of -10kV is applied at 5Hz, then increased the frequency to 50Hz after ten minutes and again after 10 minutes to 200Hz for another 10 minutes and then turned off where this is repeated again for 5kV as shown in Figure 5.21.

Figure 5.22 shows the upstream liquid, downstream gas and of wall temperature measurements as a function of heat inputs for -10kV case. The Liquid temperature at the inlet like all the other cases before is not affected greatly by the applied heat as expected since there should not be any evaporation in the liquid tank and should be in liquid state. For both the evaporator wall and the vapour exit temperatures, it can be seen that the temperatures are higher as the frequency increases which is expected since temperature is increasing with time and the frequency order is such as shown in Figure 5.21.

Figure 5.23 shows the liquid flow rate, pressure difference and the system pressure for the 5Hz, 50Hz and 200Hz for -10kV. The average system pressure is only plotted for simplicity of the figure since it can be observed from the previous cases that the system pressure does not change significantly for different cases across the heat input since steady state is attained and fluctuation is reduced. It is necessary to take a closer look at the vapour flow rate as this will explain more about the enhancement and is shown in Figure 5.24.

Figure 5.24 shows the vapour flow rate a function of heat input and different frequencies for -10kV case. With the exception of the 5Hz case in 60W and 80W where there is a large error bar, there is again enhancement shown for applied voltage. The effect of frequency is not understood and may have no effect with the chosen frequencies for enhancement of flow rate.

By the time that the positive voltage of 5kV is applied the temperature values are expected to reach a more steady state and are shown by Figure 5.25 as the temperatures of the three frequencies are within error bars for the evaporator wall and vapour exit case. This also shows that frequency has no significant effect on the temperature. The liquid inlet temperature is not affected significantly as the heat input is increased.

Once again the pressure difference across the ECE is insignificant for the different frequencies and has the same behavior as the dc case, and the system pressure is taken as an average so simplify since not a significant effect was shown in Figure 5.26. The liquid flow rate again needs to be observed as vapour flow rate for the interested heat inputs.

Once again vapour flow rate shows enhancement for applied voltage of 5kV, however some of the enhancements are within the error bars, the frequency effect is still not clear as shown in Figure 5.27.

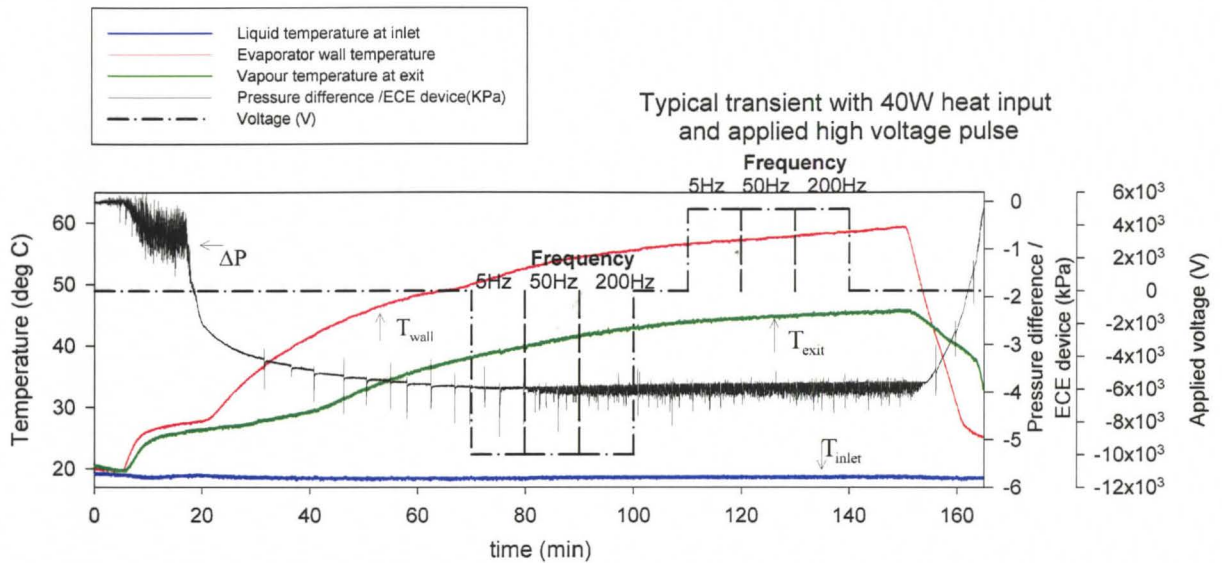


Figure 5.21: Typical transient behavior of liquid, vapour, wall-temperature and pressure difference for EHD-ECE for water cooling on condensate collection tank for heat input=40W

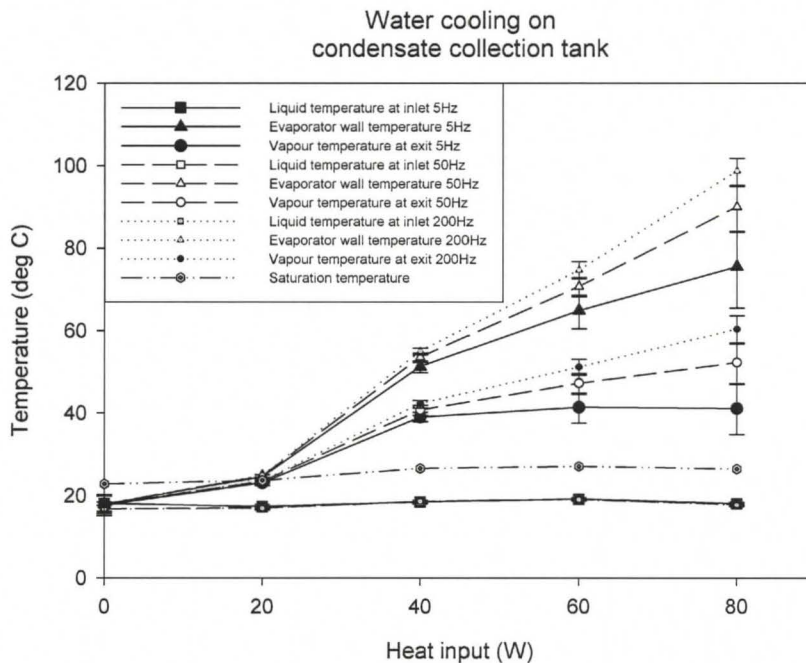


Figure 5.22: Steady state liquid, vapour and wall-temperature for EHD-ECE for water cooling on condensate collection tank as a function of heat inputs and $V = -10kV$ for various frequencies of 5Hz, 50Hz and 200Hz. The average room temperature was $20-22^{\circ}C$ and inlet cooling water $10-12.5^{\circ}C$.

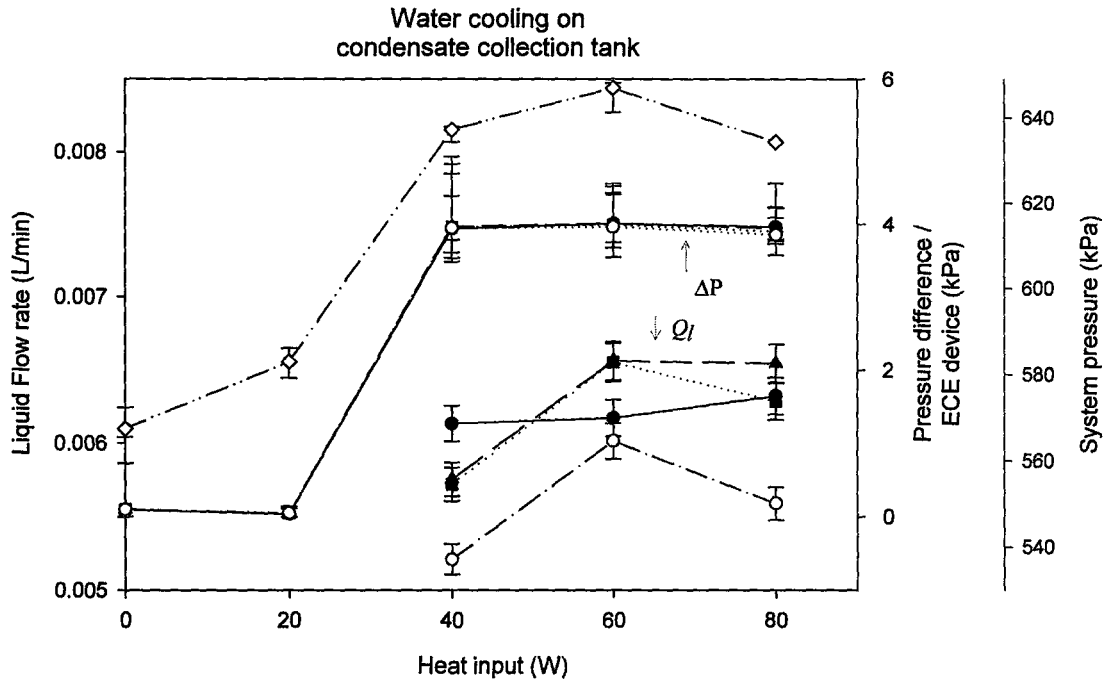
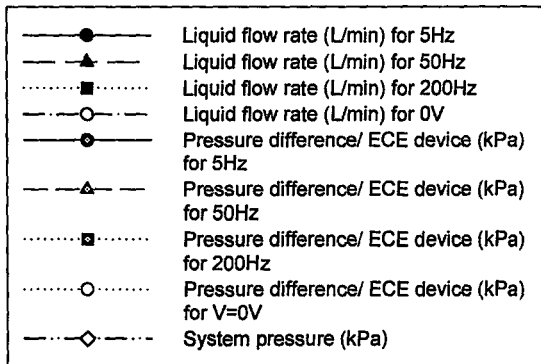


Figure 5.23: Steady state pressure difference, liquid flow rate and system pressure measurements for EHD-ECE for water cooling on condensate collection tank as a function of heat inputs at $V = -10\text{kV}$ for various frequencies of 5Hz, 50Hz and 200Hz. . The average room temperature was 20-22°C and inlet cooling water 10-12.5°C.



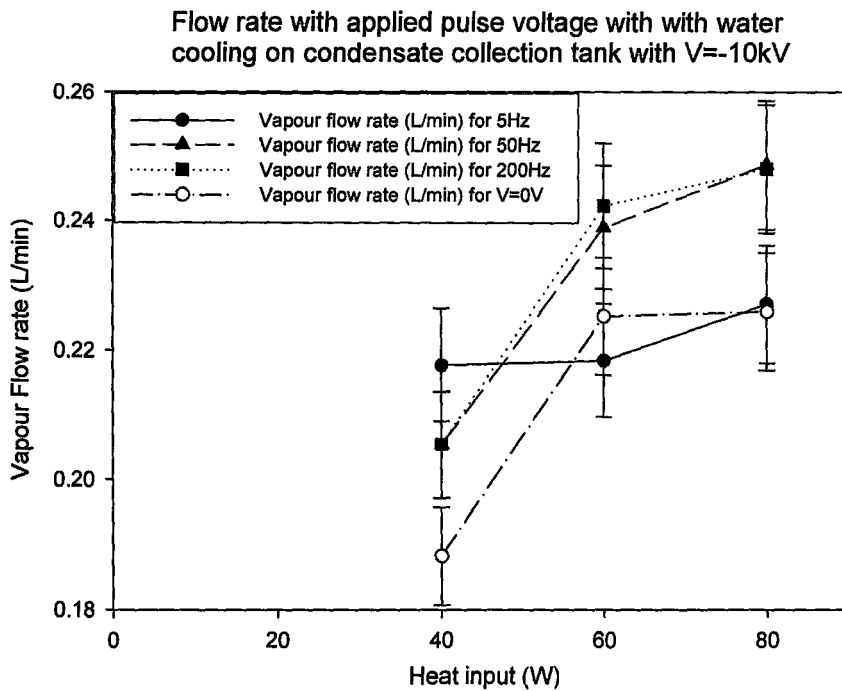


Figure 5.24: Average flow rate in EHD-ECE for water cooling on condensate collection tank as a function of heat inputs at $V = -10kV$ for various frequencies of 5Hz, 50Hz and 200Hz. The average room temperature was 20-22°C and inlet cooling water 10-12.5°C.

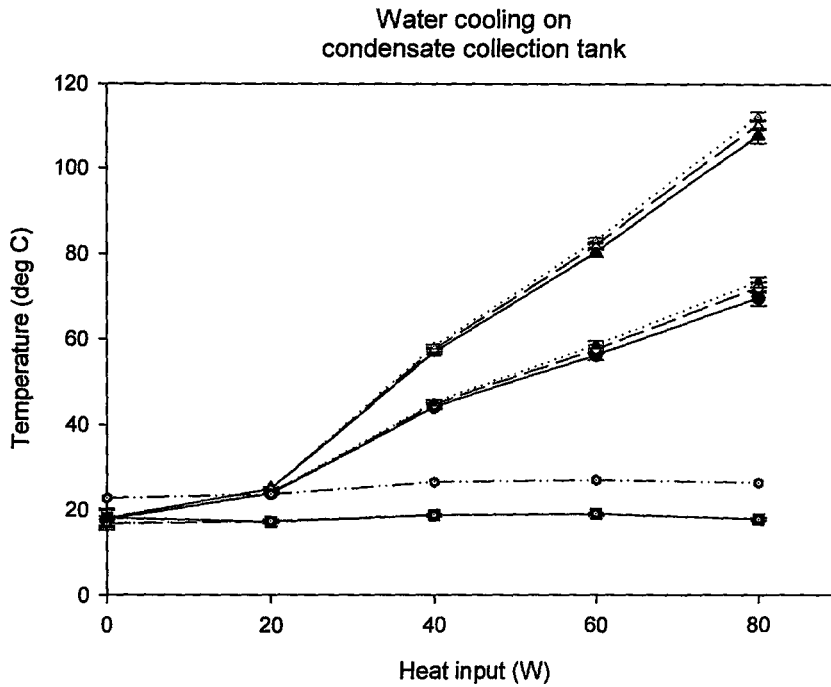
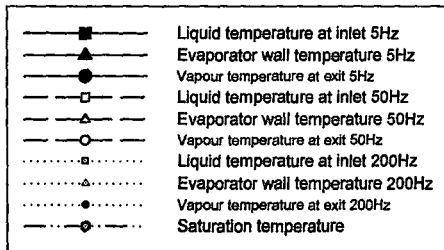


Figure 5.25: Steady state liquid, vapour and wall-temperature for EHD-ECE for water cooling on condensate collection tank as a function of heat inputs at $V=5\text{kV}$ for various frequencies of 5Hz, 50Hz and 200Hz. The average room temperature was 20-22°C and inlet cooling water 10-12.5°C



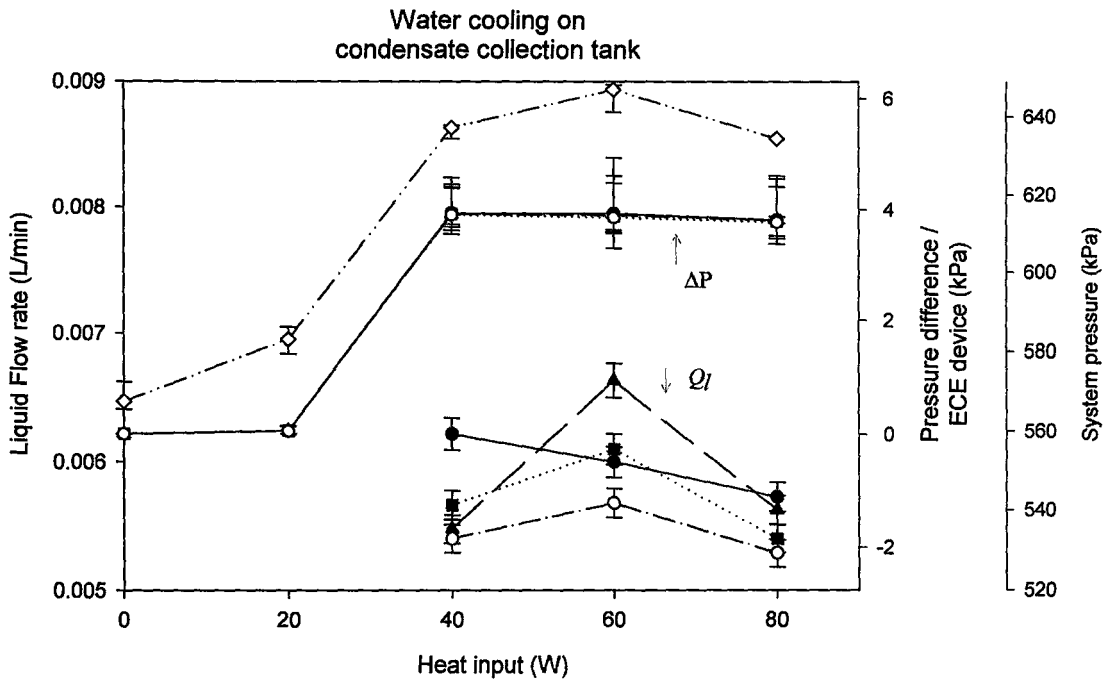
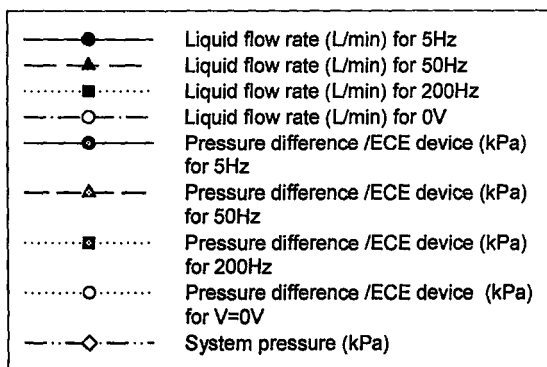


Figure 5.26: Steady state pressure difference, liquid flow rate and system pressure measurements for EHD-ECE for water cooling on condensate collection tank as a function of heat inputs at $V = 5\text{ kV}$ for various frequencies of 5Hz, 50Hz and 200Hz. The average room temperature was 20-22°C and inlet cooling water 10-12.5°C.



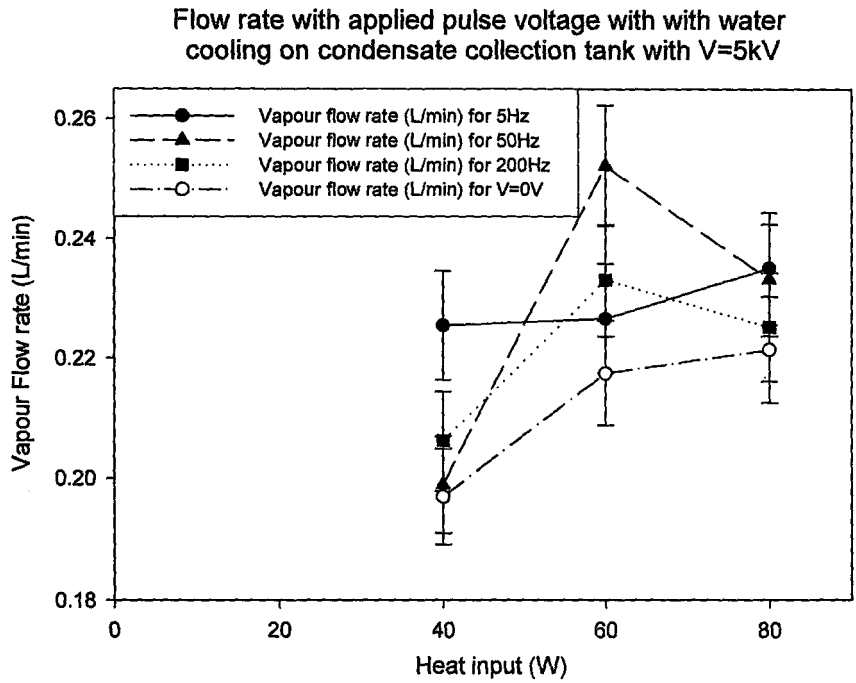


Figure 5.27: Average flow rate in EHD-ECE for water cooling on condensate collection tank as a function of heat inputs at V= 5kV for various frequencies of 5Hz, 50Hz and 200Hz. . The average room temperature was 20-22°C and inlet cooling water 10-12.5°C.

Based on the results and the theory from chapter 3 as well as the results obtained from Appendix C, a figure showing the possible reason due to the flow enhancement is shown in Figure 5.28. This shows the cross sectional view of the evaporator and the presence of the vapour at wick-fin interface. From the dimensionless values in Table C1, Appendix C, it may be concluded that the dielectrophoretic force is the dominating force and occurs at the gas-liquid interface. This force may have an instability occurring at the vapour bubble and may push the vapour bubble away from the wick-fin interface and into the vapour channel as show.

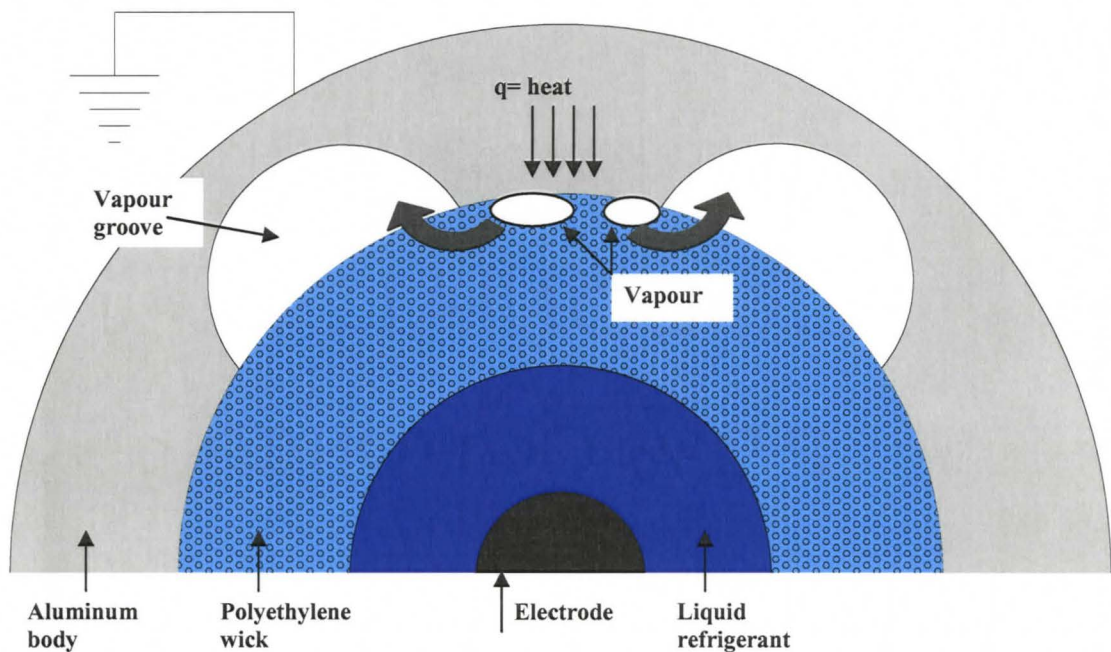


Figure 5.28: Vapour presence at the wick-fin interface.

Chapter 6

CONCLUSIONS AND RECOMMENDATIONS

The overall goal of this project was to study the feasibility of enhancing the flow rate in the electrohydrodynamic enhanced capillary evaporator with dc and pulse applied voltages. This chapter presents various conclusions based on the work performed and recommendations that could assist further enhancement of the flow rate.

6.1 Conclusions

An experiment was conducted for electrohydrodynamic enhanced capillary evaporator (EHD-ECE), where the time-averaged values of the flow rate are measured in order to study applied voltage effects. Based on the experimental investigation the following conclusions are drawn:

- For the transient region after applied heat input for no applied voltage, and the input powers 40-80W conditions, the evaporator wall temperature increases first as input power is applied and then followed by an increase in temperature in the vapour exit temperature. The evaporator wall temperature reaches steady state temperature of approximately $27\pm 1^\circ\text{C}$ at which point the temperature for the vapour exit increases to $25.5\pm 0.5^\circ\text{C}$ and the evaporator wall temperature suddenly increases significantly. The second sudden increase in evaporator wall temperature decreases in time as the power is increased. For the case of 20W the

vapour exit temperature never reaches saturation temperature and hence the second region of the evaporator wall temperature is never attained. It is interesting to note that the liquid inlet temperature remains relatively constant during the transient state whereas for the case of no cooling water on CC-tank, the liquid inlet temperature increases during the transient state and then decrease slowly. This increase in the liquid temperature is expected since no cooling with water is used.

- The pressure difference across the ECE is initially zero when input power is applied. For the case of 40-80W, a significant oscillation or “bubbly flow” in the pressure is observed across the first region of the evaporator wall temperature. The pressure actually drops first and once the saturation temperature is reached, the second region of the evaporator wall temperature increase is observed. This again may imply that once the liquid starts to evaporate in the vapour groves, the pressure drops across the ECE device, subsequently the vapour would now be at a higher temperature and hence the evaporator wall temperature would increase substantially. For the case of 20W, the temperature is not high enough to evaporate all of the trapped liquid in the vapour channels and hence no pressure drop was observed.
- The steady state evaporator wall and vapour exit temperatures increase with increasing heat load but no significant liquid inlet temperature increase was observed. Steady state measurement was observed and results shown that applied voltage had a significant effect on the flow rate both for dc and pulse applied

voltages. It was observed that positive polarity enhanced the flow rate more than negative for the same applied voltage. The polarity effect was not observed for the pulse application on the vapour flow rate. It is observed that enhancement of the vapour flow rate is present for all the pulse applied voltage for all frequencies; however the optimum frequency is unknown. No conclusion can be made between dc or pulsed method in terms of higher enhancement without further experimentation.

- It is proposed that vapour bubbles will be generated at the fin-wick interface due to the increase of heat input as shown by Schertzer et. al. (2006). This vapour bubble will act as an insulator and reduce the heat transfer to the “wetted” wick and reduce evaporation which in turn reduces the flow rate. It was suggested that an addition of EHD forces on the capillary evaporator will have external body forces acting on the interface of the liquid-vapour bubble and push the bubble towards the lower electric field region and away from the electrode. This instability effect on the vapour bubble and removal of the vapour bubble from the fin-wick interface will allow more liquid to the heated surface, which will allow more evaporation resulting in a higher flow rate. This addition of the EHD forces also may reduce transition to burn-out on the heating surface as suggested by Johnson (1968).

Present result show great potential in the future applications of EHD enhanced capillary pumped loop. Its main advantage is due to its passive nature in utilizing the capillary action to pump and therefore does not require any moving components. The

device has also shown to have the ability to enhance the flow rate through the application of EHD. However more experiments are required to fully understand the performance and behaviour of the EHD-ECE system.

6.2 Recommendations for future work

During the course of the present investigation, several suggestions can be given and should be explored in the future. The following are recommendations for future research:

- It is desirable to apply a larger heat input to the evaporator. The factor that limited this work was the PE wick that was restricted by a temperature of 150°C. Replacing this material with another non-conductive material such as a ceramic wick, which will have a much higher melting temperature, will enable a higher application of heat load. Various pore sizes and porosity should also be experimented with since these are proportional to the capillary forces.
- Different diameters as well as different shapes of the electrode voltage should be investigated with. Localizing the electric field or different electric field distribution across the electrode might have a larger enhancement on the flow rate.
- The liquid reservoir ultrasonic transducer gave inaccurate results due to the change in the liquid level since reservoir liquid was allowed to travel up the return line. It is recommended that a valve be placed beside the reservoir tank on the sight tube side; this will ensure there is no other direction for the flow than towards the liquid tank.

References:

1. P. Atten, and J. Seyed-Yagoobi, "Electrohydrodynamically Induced Dielectric Liquid Flow Through Pure Conduction in Point/Plane Geometry", IEEE Transactions on Dielectrics and Electrical Insulation Vol. 10, No. 1, pp. 27-36, 2003.
2. M. Aoyama and S. Masuda, "Theoretical characteristics of double and triple array electric curtains of standing wave type", Proc. Institute of Electrostatics Japan, Vol. 1, pp.123, 1977.
3. D. Avsec and M. Luntz, Comptes-Rendus, Paris, Vol. 204, pp. 420-428, 1937.
4. A.E Bergles, M.K Jensen, E.F.C. Somerscales and R.M. Manglik, "Literature review of Heat Transfer Enhancement Technology for Heat Exchangers in Gas Fired Application", GRI 91-0146, Gas research institute, Chicago, IL, 1991.
5. B.J., Bohinsky & J. Seyed-Yagoobi, "Induction electrohydrodynamic pumping-selecting an optimum working fluid", IEEE Industry Applications Society Annual Meeting, Vol. 1, pp. 795-801, 1990.
6. J. E. Bryan and J. Seyed-Yagoobi, "An Experimental Investigation of Ion-drag Pump in a Vertical and Axisymmetric Configuration", IEEE Transactions on Industry Applications, Vol. 28, No. 2, pp. 310-316, 1992.
7. J.E Bryan and J. Seyed-Yagoobi, "Electrohydrodynamically enhanced convective boiling: relationship between electrohydrodynamic pressure and momentum flux rate", Journal of heat transfer, Vol. 122 pp.266-277, 2000.
8. D. Butler and R. McIntosh, "Development and Integration of the Capillary Pumped Loop gas and Hitchhiker Flight Experiments", NASA Technical Memorandum 100756, 1990.
9. J.C. Campeau, J.S. Chang and S. Masuda, "Particulate Phenomena & Multi-Phase Transport", (ed: T.N. Vezirglu) Hemisphere Pub. Co., Washington, Vol. 5, pp. 3-9, 1988.
10. Y. Cao and A. Faghri, "Conjugate analysis of a flat-plate type evaporator for capillary pumped loops with three-dimensional vapor flow in the groove", Int. J. Heat Mass Transfer, Vol 37, No 3. pp. 401-409, 1994.

11. J.S. Chang, W.H. Baird, and S. Masuda, "Development of Pulsed Travelling Wave Type EHD Powder Pump: Preliminary Results", *Mat. Sci.* Vol XVI, pp. 9-14, 1985.
12. J.S. Chang "Stratified gas-liquid two-phase electrohydrodynamics in horizontal pipe flow", *IEEE Trans. Ind. Appl.*, Vol 25, No. 2 pp. 241-247, 1989b.
13. J.S. Chang and A. Watson, "Electromagnetic Hydrodynamics", *IEEE Transactions on Dielectrics and Electrical Insulation* Vol 1, No 5, pp. 871-895, 1994.
14. J.S. Chang, "Two-phase flow in electrohydrodynamics" in part V of "Electrohydrodynamics", International centre for mechanical sciences courses and lectures – No.380, A. Castellanos ed., Springer Wein, New York, pp. 279-349, 1998.
15. R.C. Chu, IBM "Thermal Management Roadmap Cooling Electronic Products from Hand-Held Devices to Supercomputers", Rohsenow Symposium on Future Trends in Heat Transfer, Cambridge, MA, 2003.
16. L.W. Chubb, "Improvements relating to Methods and Apparatus for Heating Liquids", U.K. Patent No. 100796, 1916.
17. J. Cotton, A.J. Robinson, M. Shoukri, J.S. Chang "A two-phase flow pattern map for annular channels under a DC applied voltage and the application to electrohydrodynamic convective boiling analysis", *International Journal of Heat and Mass Transfer*, Vol. 48, pp. 5563-5579, 2005.
18. J.M., Crowley, G.S. Wright, and J.C. Chato, "Selecting a working fluid to increase the efficiency and flow rate of an EHD pump", *IEEE Trans. Ind. Appl.* Vol 26, No 1, pp. 42-49, 1990.
19. J.L. Fernandez, and R. Poulter, "Radial mass flow in electrohydrodynamically-enhanced forced heat transfer in tubes", *Int. J. Heat Mass Transfer*, Vol. 30 No. 10, pp. 2125-2136, 1987.
20. W. He and J.S Chang, "EHD enhanced mass transfer operations and chemical reactions". in "Handbook of electrostatic processes", J.S. Chang, A.J Kelly and J.M Crowley, ed., Marcel Dekker, Inc.,New York, pp 527-554, 1995.
21. IEEE-DEIS-EHD Technical Committee, "Recommended International Standard for Dimensionless Parameters Used in Electrohydrodynamics", *IEEE Transactions on Dielectrics & Electrical Insulation.* Vol 10 pp 3-6, 2003.

22. H.R. Jeng and C. Pan, “Analysis of two-phase flow characteristics in a natural circulation loop using the drift-flux model taking flow pattern change and subcooled boiling into consideration”, *Annals of Nuclear Energy*, Vol. 26 pp.1227–1251, 1999.
23. R.L. Johnson, “Effect of an electric field on boiling heat transfer”, *AIAA Journal*, Vol. 6, pp. 1456-1460, 1968.
24. T.B. Jones, and G.W. Bliss, “Bubble dielectrophoresis”, *J. Appl. Phys.* Vol. 48, pp.1412-1422. 1977.
25. J.T. Kim and J.S. Chang, “Generation of metal oxide aerosol particles by a pulsed spark discharge technique”, *Journal of electrostatics*, Vol.63, pp. 911-916, 2005.
26. B. Komeili, J.S. Chang, and G. Harvel, “Polarity Effect and Flow Characteristics of Wire Rod Type Electrohydrodynamic Gas Pump” 2006 IEEE Conference on Electrical Insulation and Dielectric Phenomena, pp. 182-185, 2006.
27. G.H. Krawinkel, “Zum wirkungsgrad einer elektrostatischen pumpe”, *Z. Angewandte Phys.* Vol. 25, No. 5, pp. 302-306, 1968.
28. S. Masuda and Matsumoto, “Motion of a Microcharge Particle within EHD Field”, *Trans. I.E.C.E. Japan*, Vol. 93-B, pp. 41, 1973.
29. J.R Melcher, “Traveling-Wave Induced Electro-convection”, *Phys. Fluids*, Vol. 9, No.8 pp. 1548-1555, 1966.
30. J.R Melcher, “Electric fields and forces in semi-insulating liquids”, *Journal of electrostatics*, Vol. 2, pp. 121-132, 1976.
31. B. Mo, M.M. Ohadi, S.V. Dessiatoun, K.R. Wrenn, “Capillary pumped-loop thermal performance improvement with electrohydrodynamic technique”, *Journal of Thermophysics and heat transfer*, Vol 14, pp. 103-108, 2000.
32. H. Morgan, N.G.Green, M.P.Hughes, W.Monaghan and T.C.Tan “Large-area travelling-wave dielectrophoresis particle separator”, *J. Micromech. & Microeng.* vol. 7 pp. 65-70, 1997.
33. S. Ogata, K. Tan, K. Nishijima, and J.S. Chang, “Development of improved bubble disruption and dispersion technique by an applied electric field method”, *AICHE Journal* Vol. 31, pp. 62-69, 1985.
34. J.M.H. Peters, J. L. Sproston, and G. Walker, “Preliminary observations on bulk electroconvection in electrically stressed liquid insulants Part I: Experimental Investigation”, *J. Electrostatics.* Vol. 8, pp. 139-152, 1980a.

35. W. Pickard, *Progress in Dielectrics*, Vol. 6, Heywood and Co. Ltd., London, 1965.
36. H.A. Pohl, "Some Effects of Nonuniform Fields on Dielectrics", *Journal of Applied Physics*, Vol. 29, Issue 8, pp. 1182-1188, 1958.
37. F. Pollack, "New Microarchitecture Challenges in the Coming Generations of CMOS Process Technologies," *Micro32*, 1999.
38. M.J. Schertzer, D. Ewing, C.Y. Ching, "The effect of gap distance on the heat transfer between a heated finned surface and a saturated porous plate", *International Journal of Heat and Mass Transfer*, Vol. 49, pp. 4200-4208, 2006.
39. J. Seyed-Yagoobi, B.D. Margo and J.E. Bryan, "Effect of Frequency on Heat Transfer Enhancement in Temperature-induced Electrohydrodynamic Pumping", *IEEE Transactions on Dielectrics and Electrical Insulation* Vol. 1 No. 3, pp. 468-473, 1994.
40. S.J Shelestynsky, "Two-Phase Flow in Capillary Pumped Loops", PhD thesis, McMaster University, 2007.
41. F.J. Stenger, "Experimental feasibility study of water-filled capillary-pumped heat-transfer loops", NASA-TM-X-1310, NASA Lewis Research Center, Cleveland, Ohio, 1966.
42. A. H. Sharbaugh and G. W. Walker, "The Design and Evaluation of an Ion-Drag Dielectric Pump to Enhance Cooling in a Small Oil-Filled Transformer", *IEEE Trans. Indust. Appl.*, Vol. 21, pp. 950-955, 1985.
43. O.M Stuetzer, "Ion drag pressure generation", *Journal of applied physics*, volume 30. No 7, pp. 984-994, 1958.
44. H.R. Velkoff, and J.H. Miller, "Condensation of vapour on a vertical plate with a transverse electrostatic field", *ASME J.Heat Transfer*, Vol. 87, pp 197-201, 1965.
45. P.K. Vijayan, "Experimental observations on the general trends of the steady state and stability behaviour of single-phase natural circulation loops", *Nuclear Engineering and Design* vol 215, pp. 139–152, 2002.
46. R.L Webb, A.E Bergles and G.H Junkhan, "Bibliography of U.S. patents on Augmentation of Convective Heat and Mass Transfer", Heat Transfer Laboratory report HTL-32, ISU-ERI-Ames-81070, Iowa State University, 1983b.

47. H.G Wulz and F. Mayinge, “Heat and fluid transport in an evaporative capillary pump”, International journal of energy research, Vol 17, pp. 1-18, 1993.
48. A. Yabe, “Heat Engineering” in “Handbook of electrostatic processes”, J.S. Chang, A.J Kelly and J.M Crowley, ed., Marcel Deker, Inc., New York, pp 555-580, 1995.
49. A.I. Zhakin, “Conduction phenomena in dielectric liquids, EHD models, Linear and nonlinear effects on the charged interface, EHD pumping of dielectric liquids” in part II of “Electrohydrodynamics”, International centre for mechanical sciences courses and lectures – No.380, A. Castellanos ed., Springer Wein, New York, pp. 149-162, 1998.
50. Y. Zvirin, “A Review of Natural Circulation Loops in Pressurized Water Reactors and Other Systems” NUC. Eng. Des., 67, pp. 203-225, 1981.

Appendix A

A.1 Transient thermal, pressure difference, system pressure liquid and liquid reservoir characteristics of capillary pump without condensate collection tank water cooling

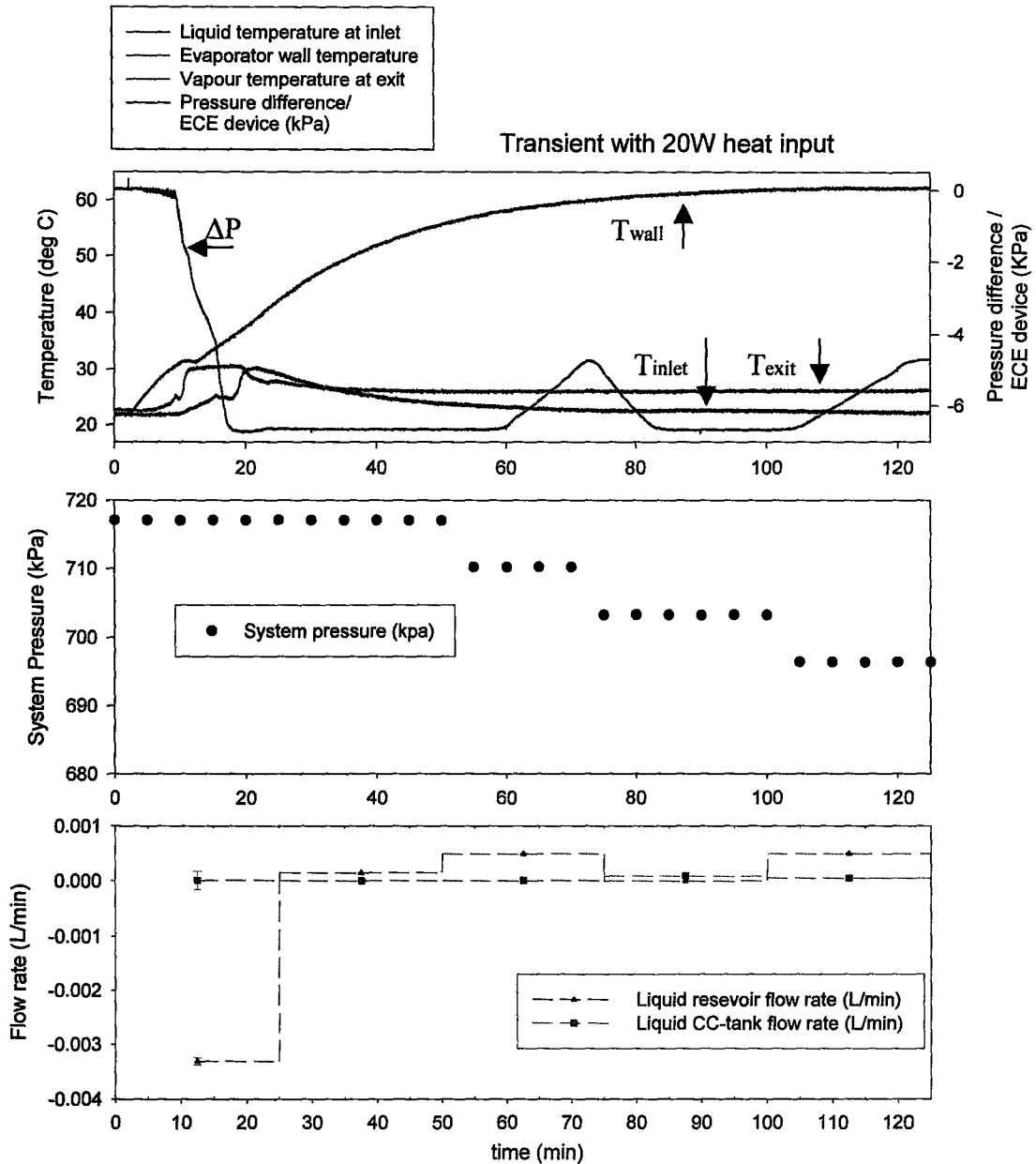


Figure A.1: Transient behaviour of liquid, vapour, wall-temperature and pressure difference /ECE device for EHD-ECE , system pressure, liquid and liquid reservoir flow rates for no water cooling on condensate collection tank for heat input=20W at V=0

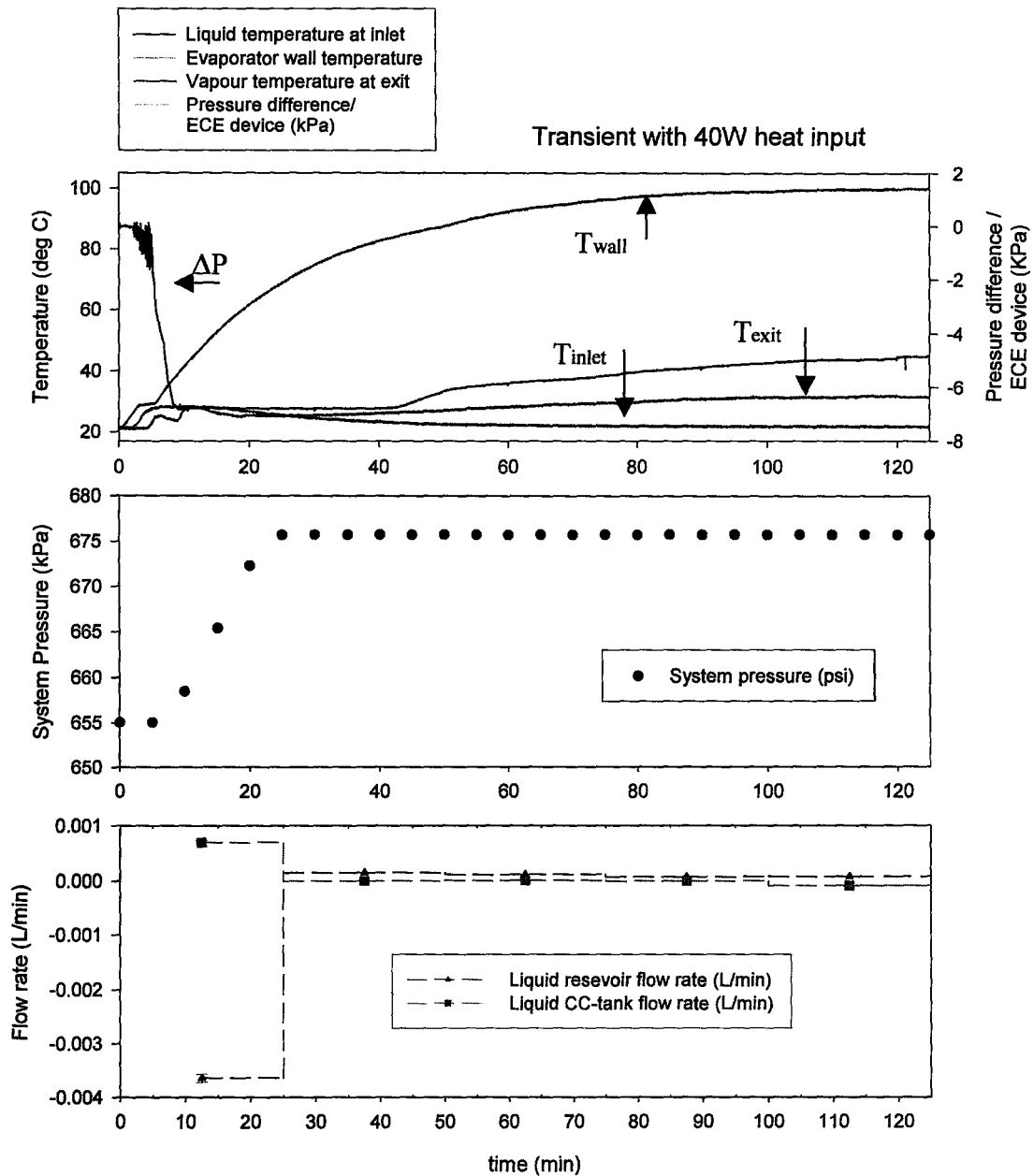


Figure A.2: Transient behaviour of liquid, vapour, wall-temperature and pressure difference /ECE device for EHD-ECE , system pressure, liquid and liquid resevoir flow rates for no water cooling on condensate collection tank for heat input=40W at V=0

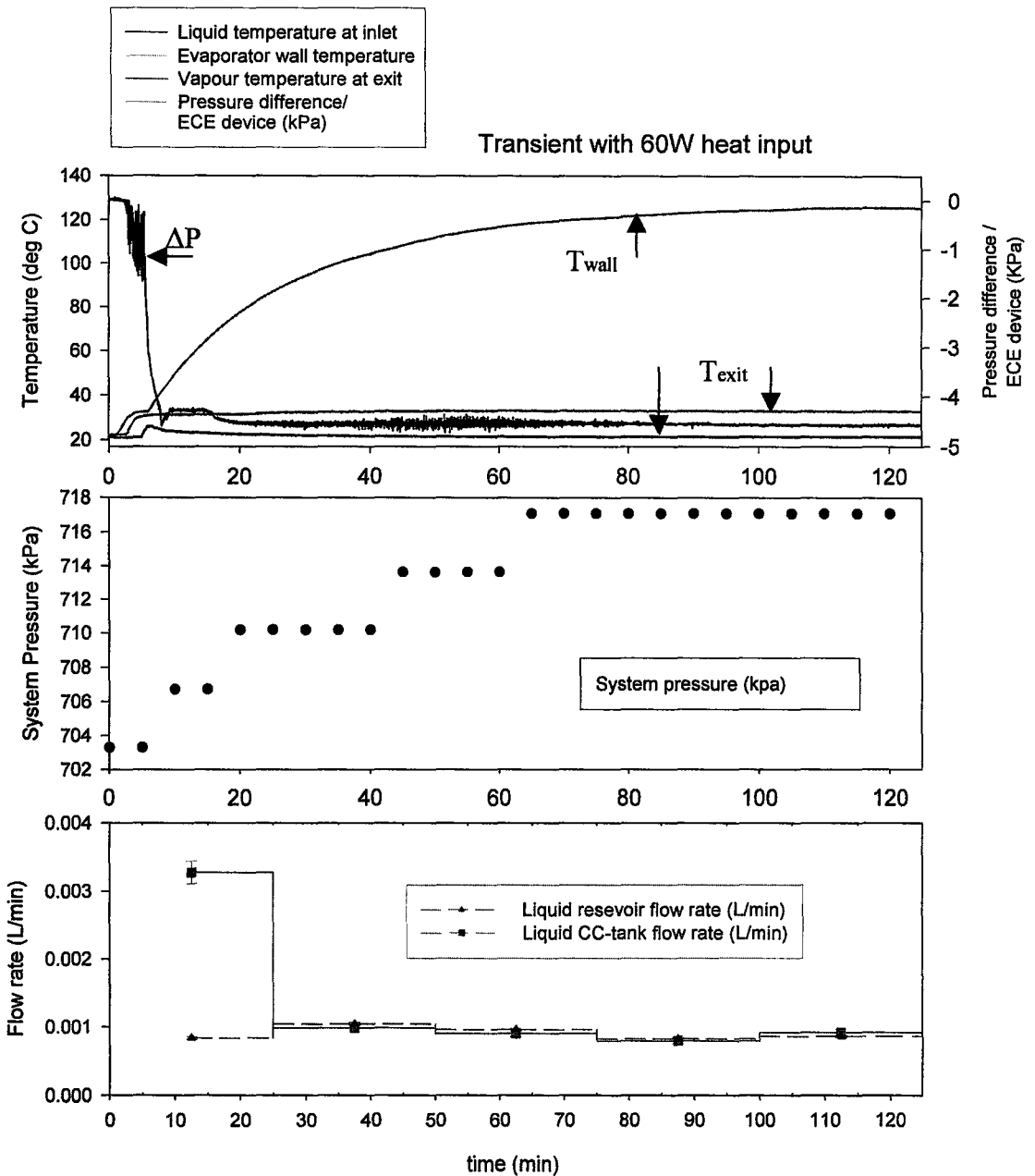


Figure A.3: Transient behaviour of liquid, vapour, wall-temperature and pressure difference /ECE device for EHD-ECE , system pressure, liquid and liquid reservoir flow rates for no water cooling on condensate collection tank for heat input=60W at V=0

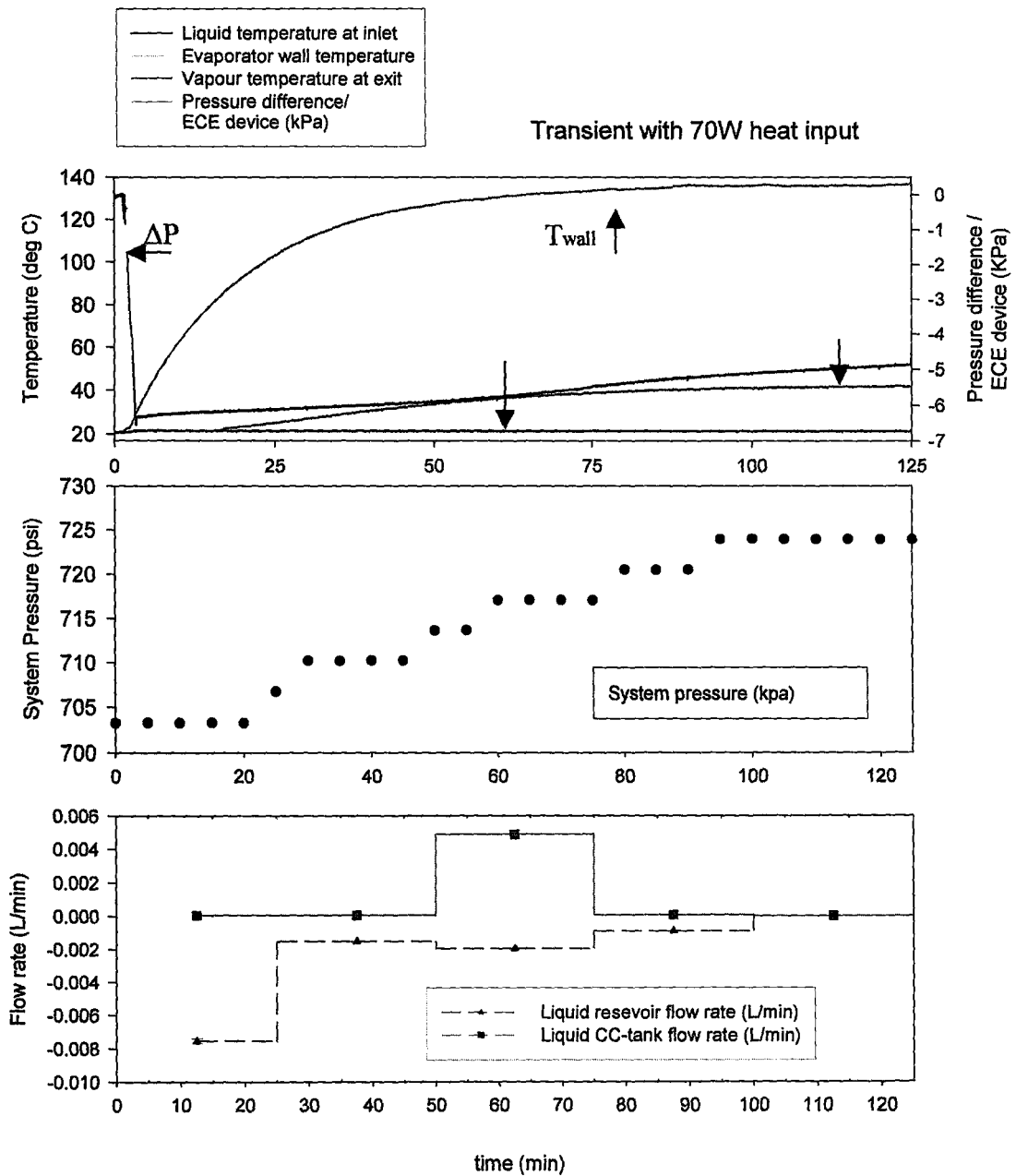


Figure A.4: Transient behaviour of liquid, vapour, wall-temperature and pressure difference /ECE device for EHD-ECE , system pressure, liquid and liquid reservoir flow rates for no water cooling on condensate collection tank for heat input=70W at V=0

A.2 Transit time thermal, pressure difference, system pressure liquid and liquid reservoir characteristics of capillary pump with condensate collection tank water cooling

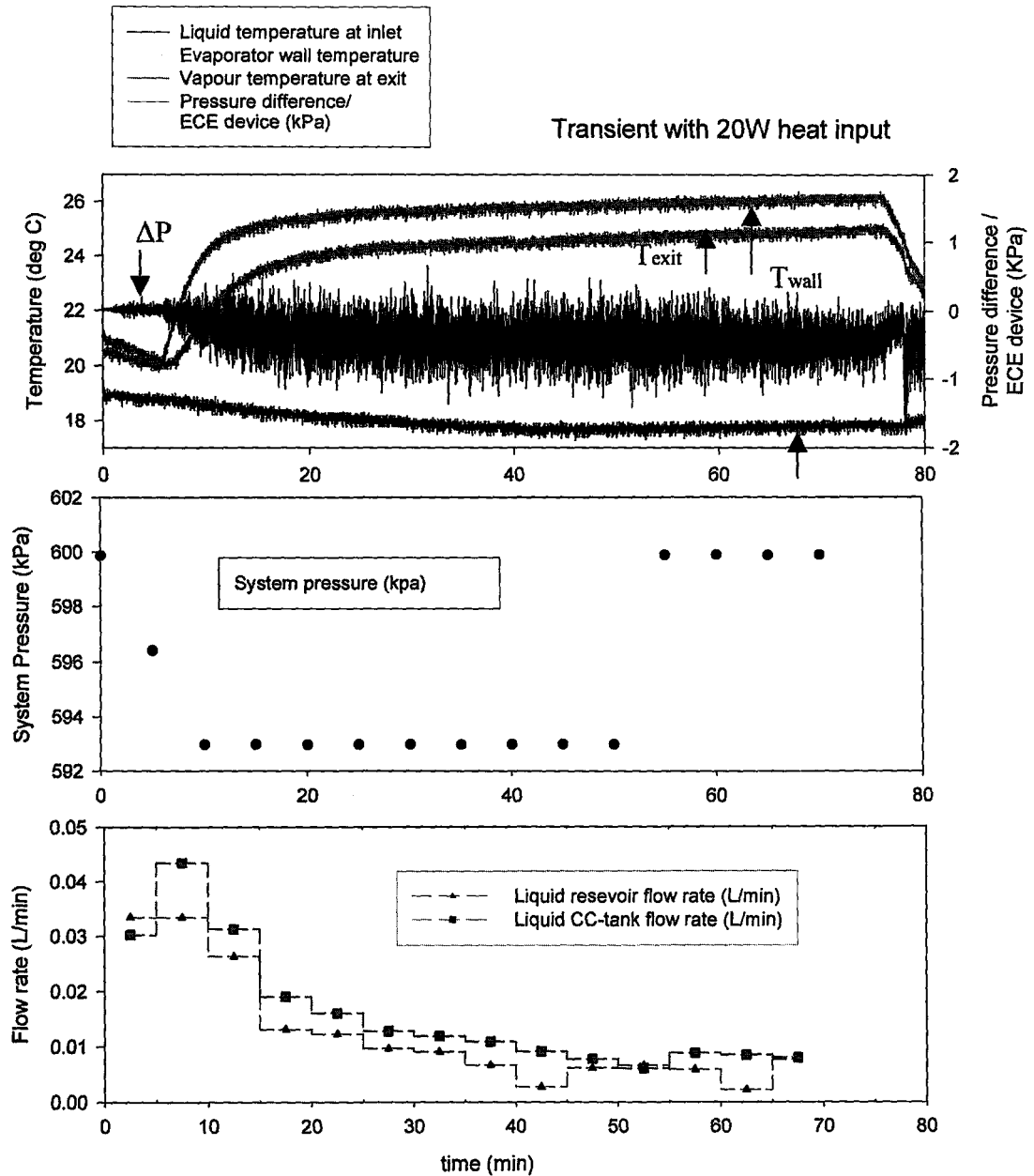


Figure A.5: Transient behaviour of liquid, vapour, wall-temperature and pressure difference /ECE device for EHD-ECE , system pressure, liquid and liquid reservoir flow rates for water cooling on condensate collection tank for heat input=20W at V=0

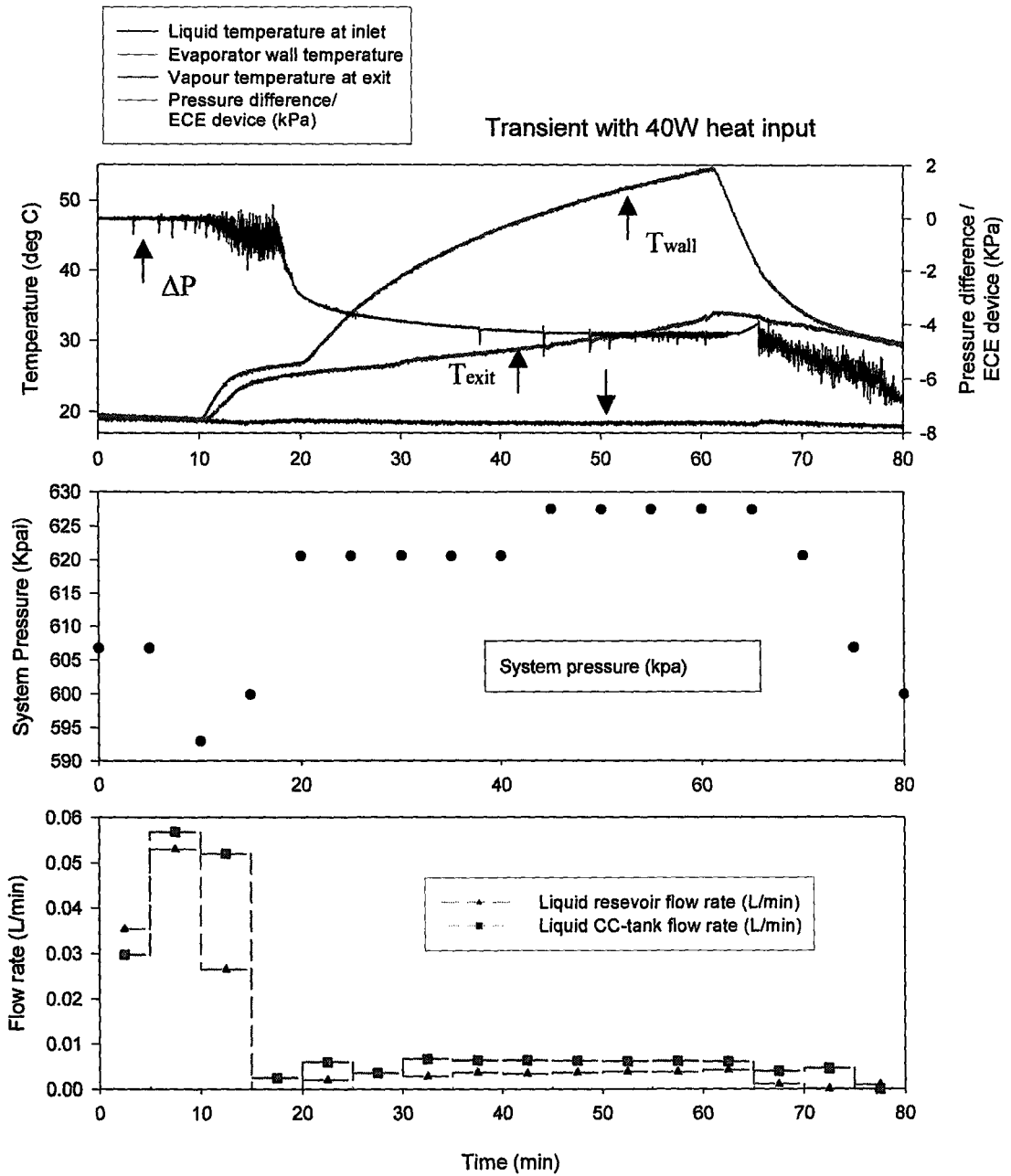


Figure A.6: Transient behaviour of liquid, vapour, wall-temperature and pressure difference /ECE device for EHD-ECE , system pressure, liquid and liquid reservoir flow rates for water cooling on condensate collection tank for heat input=40W at V=0

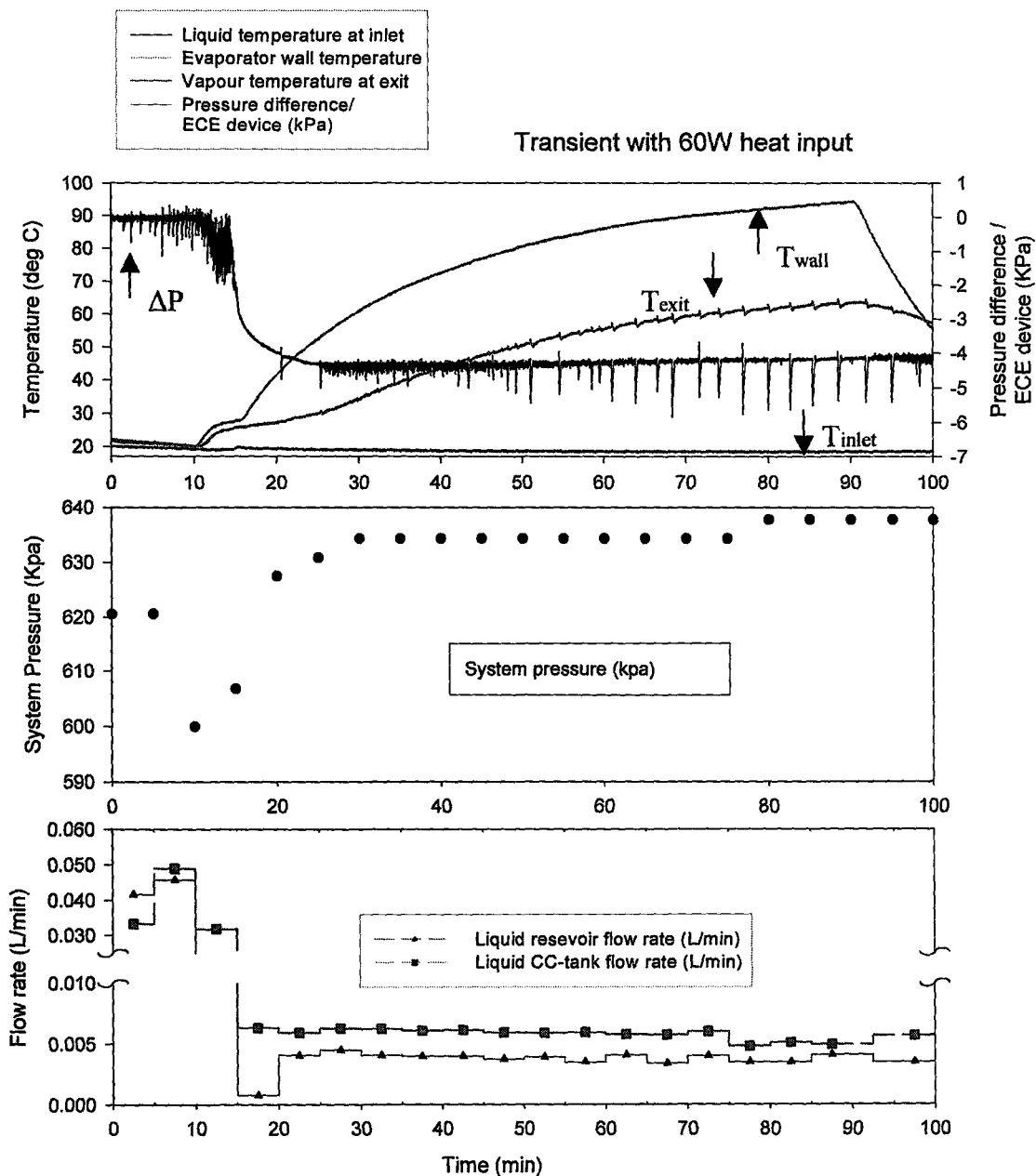


Figure A.7: Transient behaviour of liquid, vapour, wall-temperature and pressure difference /ECE device for EHD-ECE , system pressure, liquid and liquid reservoir flow rates for water cooling on condensate collection tank for heat input=60W at V=0

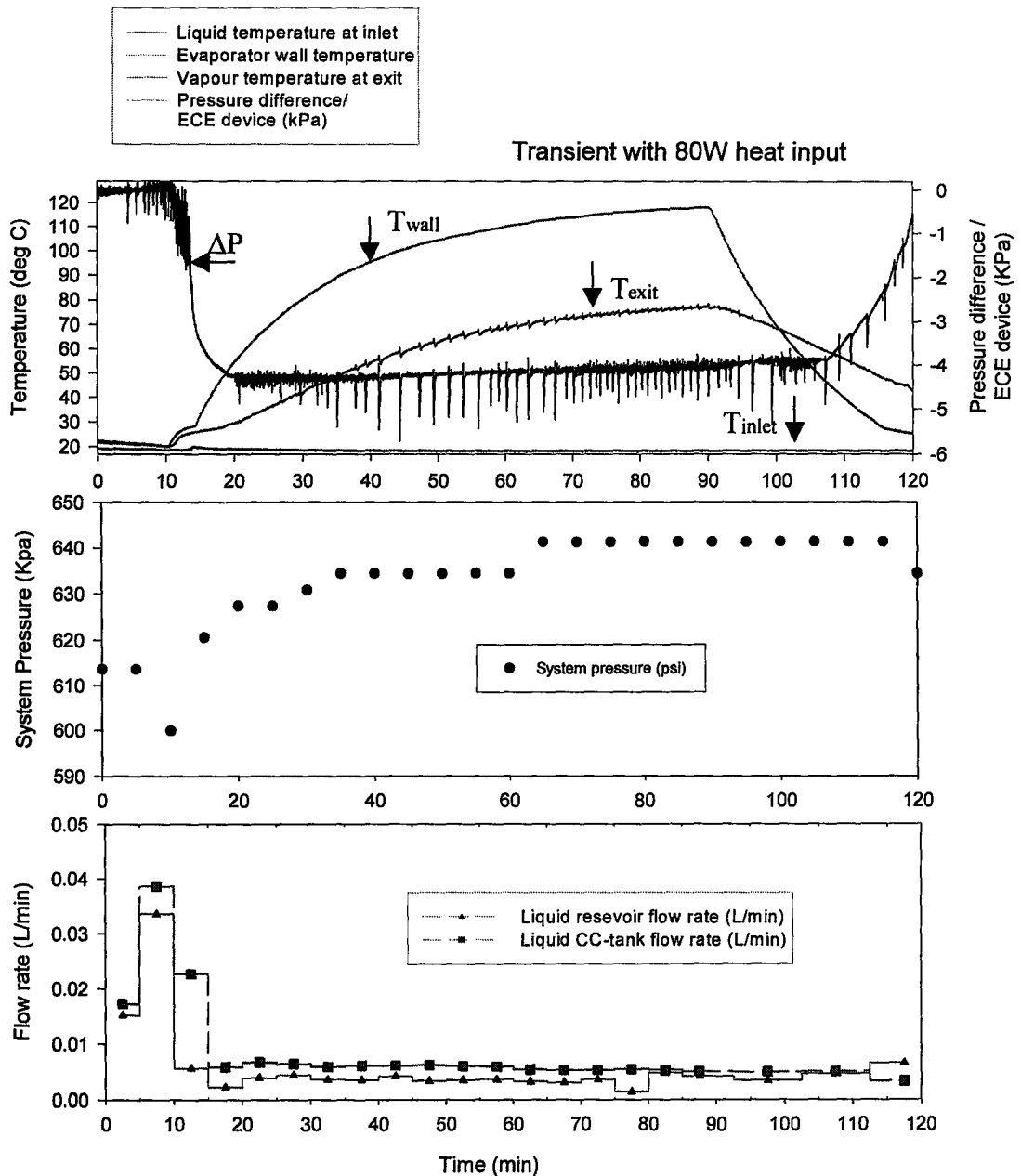


Figure A.8: Transient behaviour of liquid, vapour, wall-temperature and pressure difference /ECE device for EHD-ECE , system pressure, liquid and liquid reservoir flow rates for water cooling on condensate collection tank for heat input=60W at V=0

A.3 Transit time thermal, pressure difference, system pressure liquid and liquid reservoir characteristics of capillary pump with condensate collection tank water cooling with dc voltage

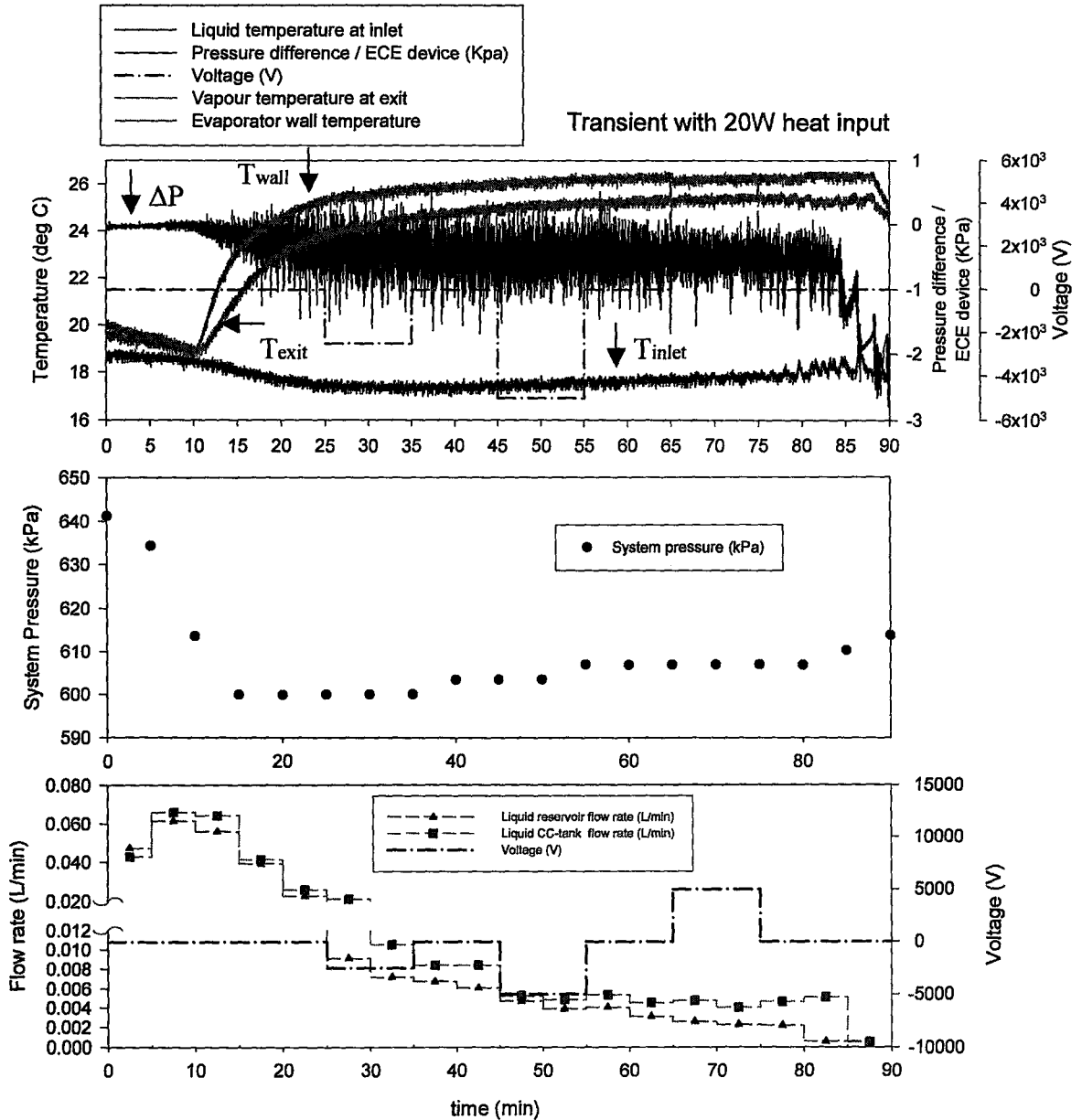


Figure A.9: Transient behaviour of liquid, vapour, wall-temperature and pressure difference /ECE device for EHD-ECE, system pressure, liquid and liquid reservoir flow rates for water cooling on condensate collection tank for heat input=20W at applied voltage

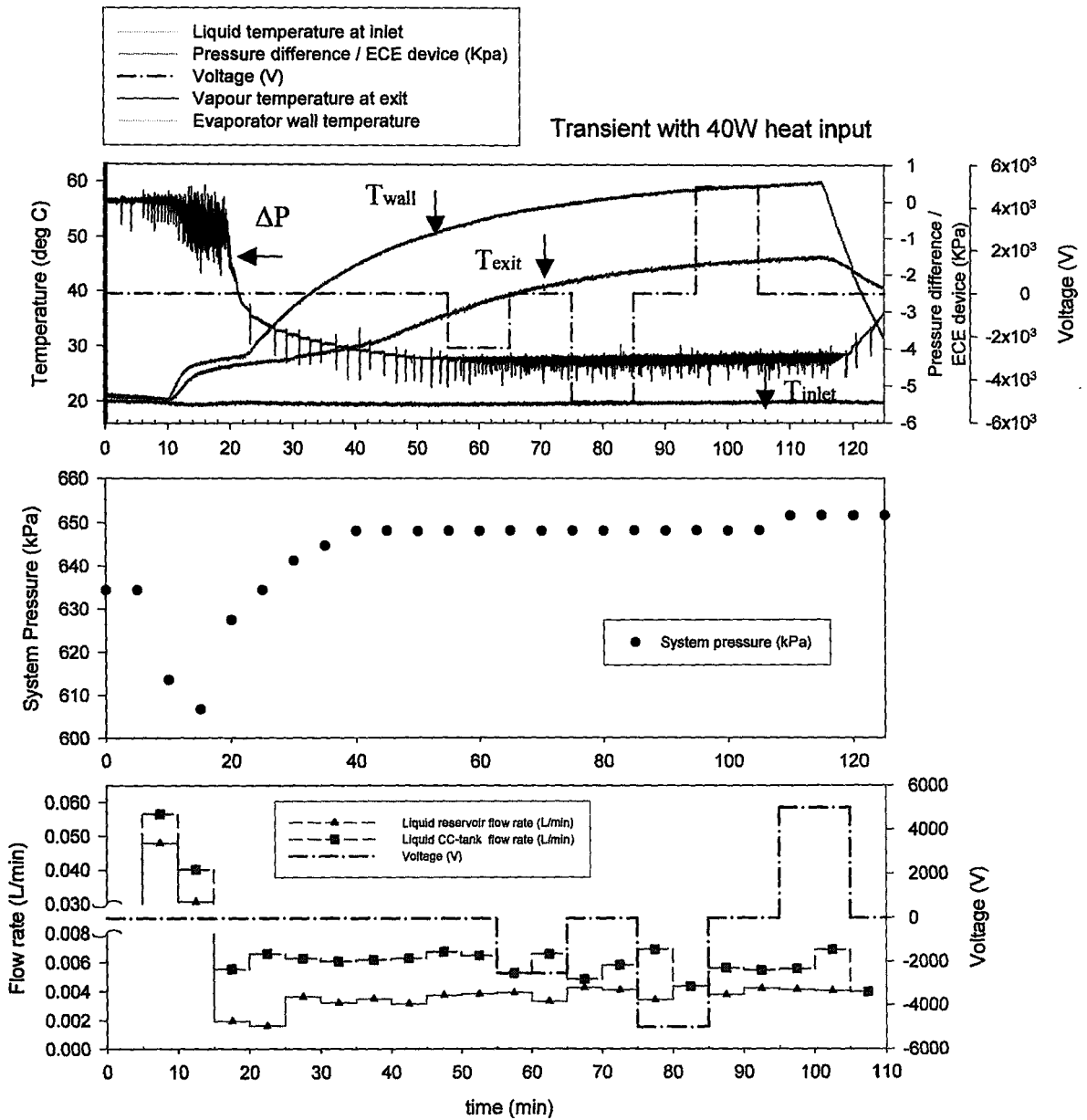


Figure A.10: Transient behaviour of liquid, vapour, wall-temperature and pressure difference /ECE device for EHD-ECE , system pressure, liquid and liquid reservoir flow rates for water cooling on condensate collection tank for heat input=40W at applied voltage

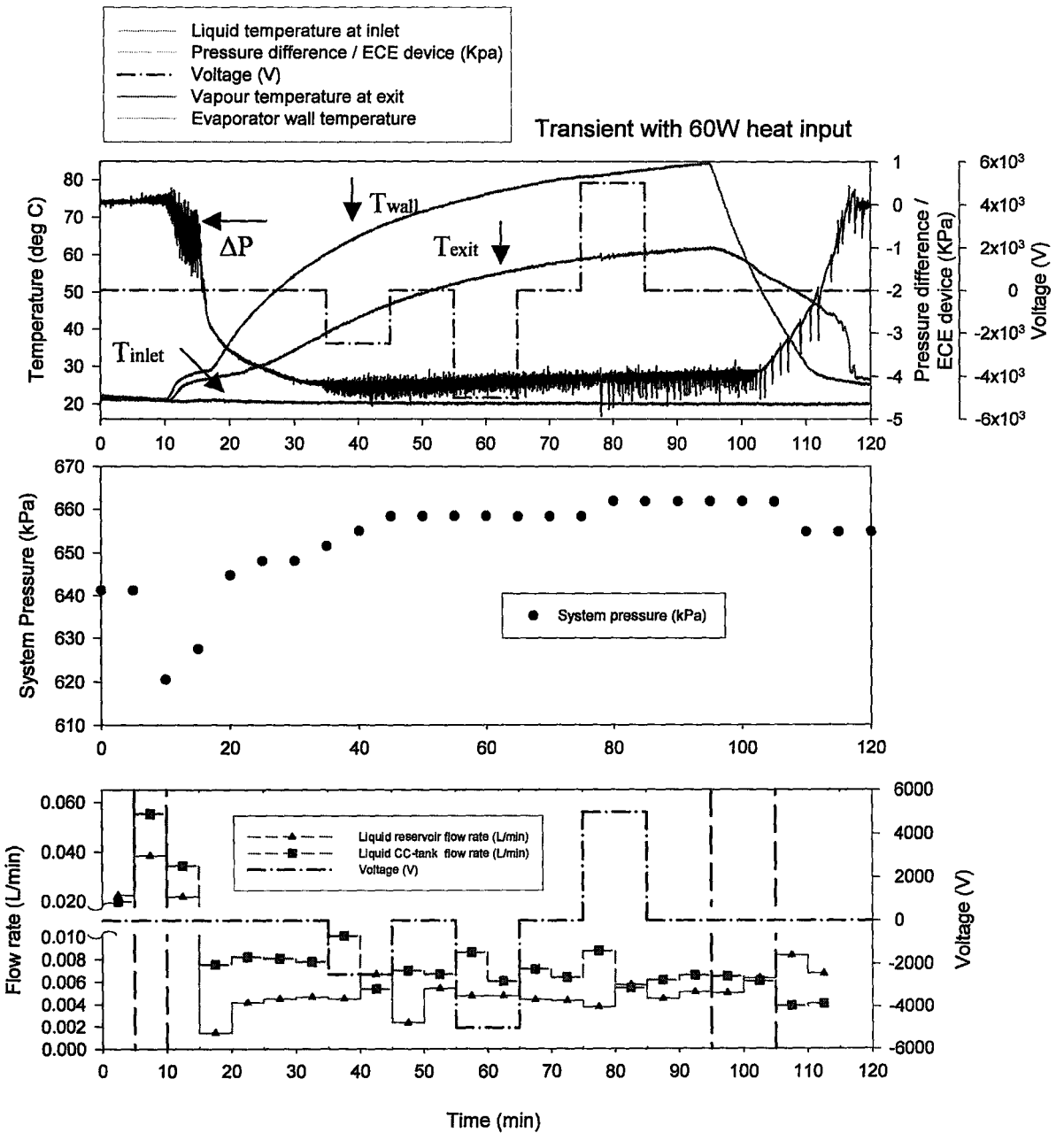


Figure A.11: Transient behaviour of liquid, vapour, wall-temperature and pressure difference /ECE device for EHD-ECE , system pressure, liquid and liquid reservoir flow rates for water cooling on condensate collection tank for heat input=60W at applied voltage

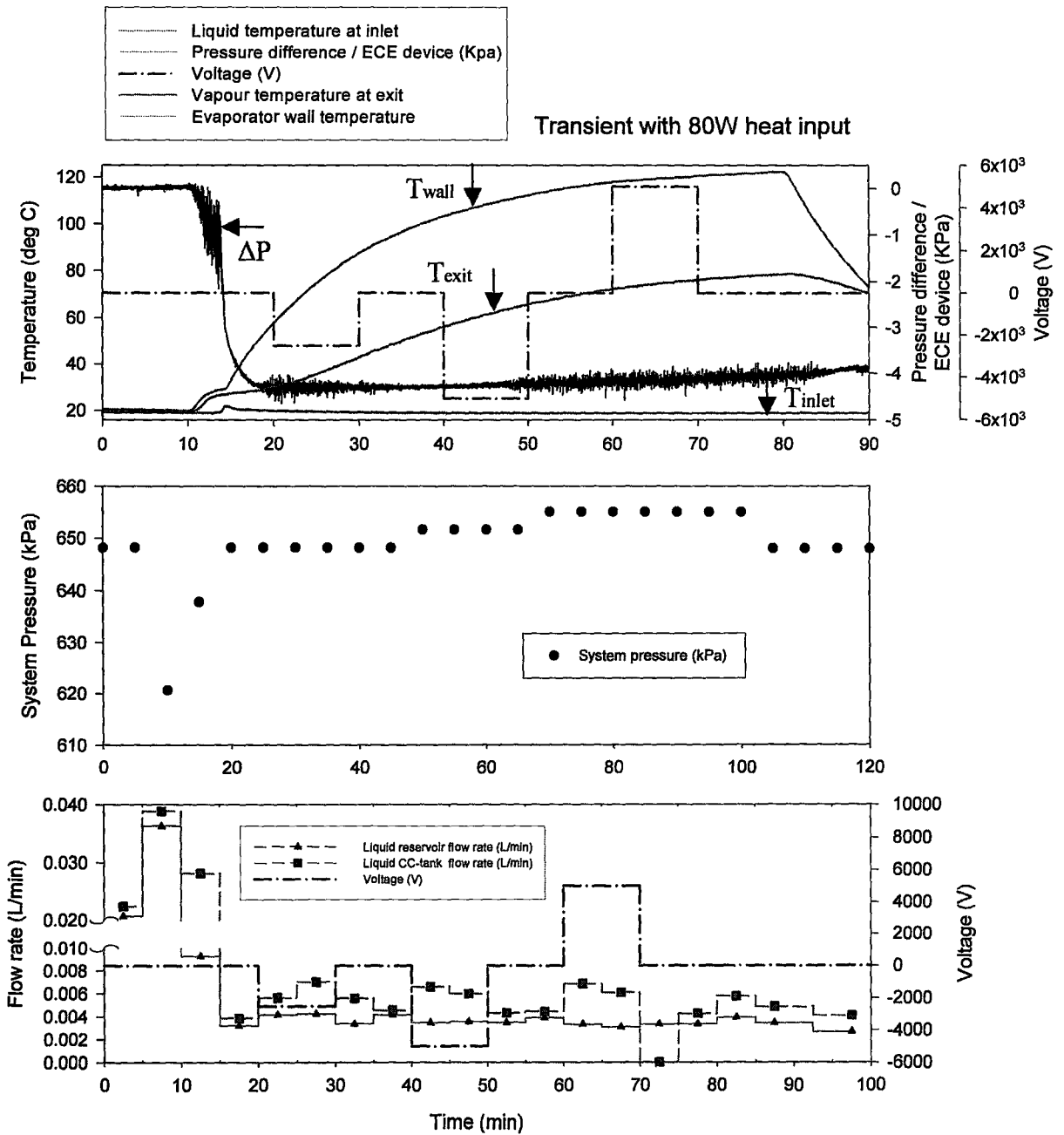


Figure A.12: Transient behaviour of liquid, vapour, wall-temperature and pressure difference /ECE device for EHD-ECE , system pressure, liquid and liquid reservoir flow rates for water cooling on condensate collection tank for heat input=80W at applied voltage

A.4 Transit time thermal, pressure difference, system pressure liquid and liquid reservoir characteristics of capillary pump with condensate collection tank water cooling with pulse voltage with frequency range 50-200Hz

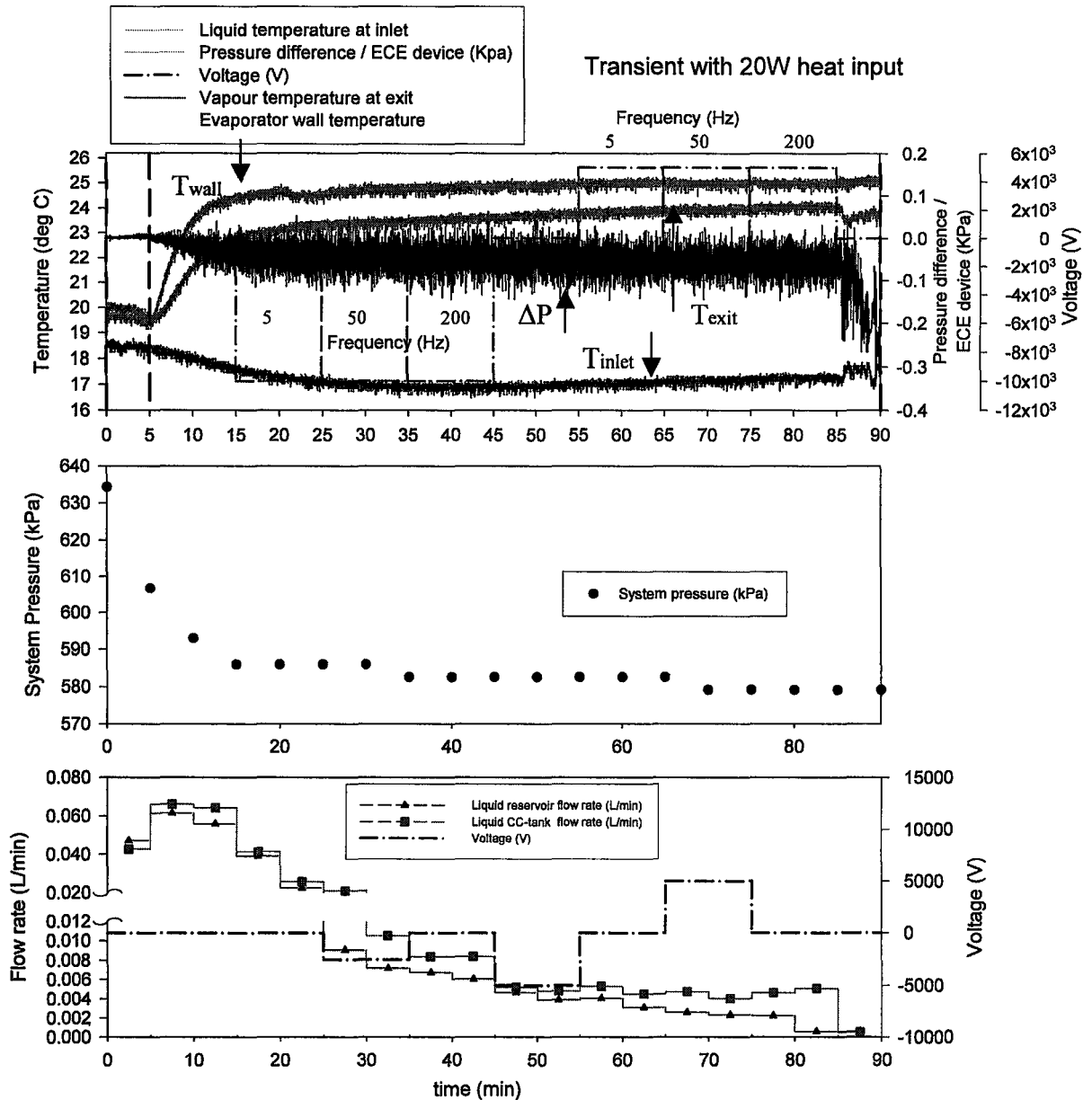


Figure A.13: Transient behaviour of liquid, vapour, wall-temperature and pressure difference /ECE device for EHD-ECE, system pressure, liquid and liquid reservoir flow rates for water cooling on condensate collection tank for heat input=20W at applied pulse voltage

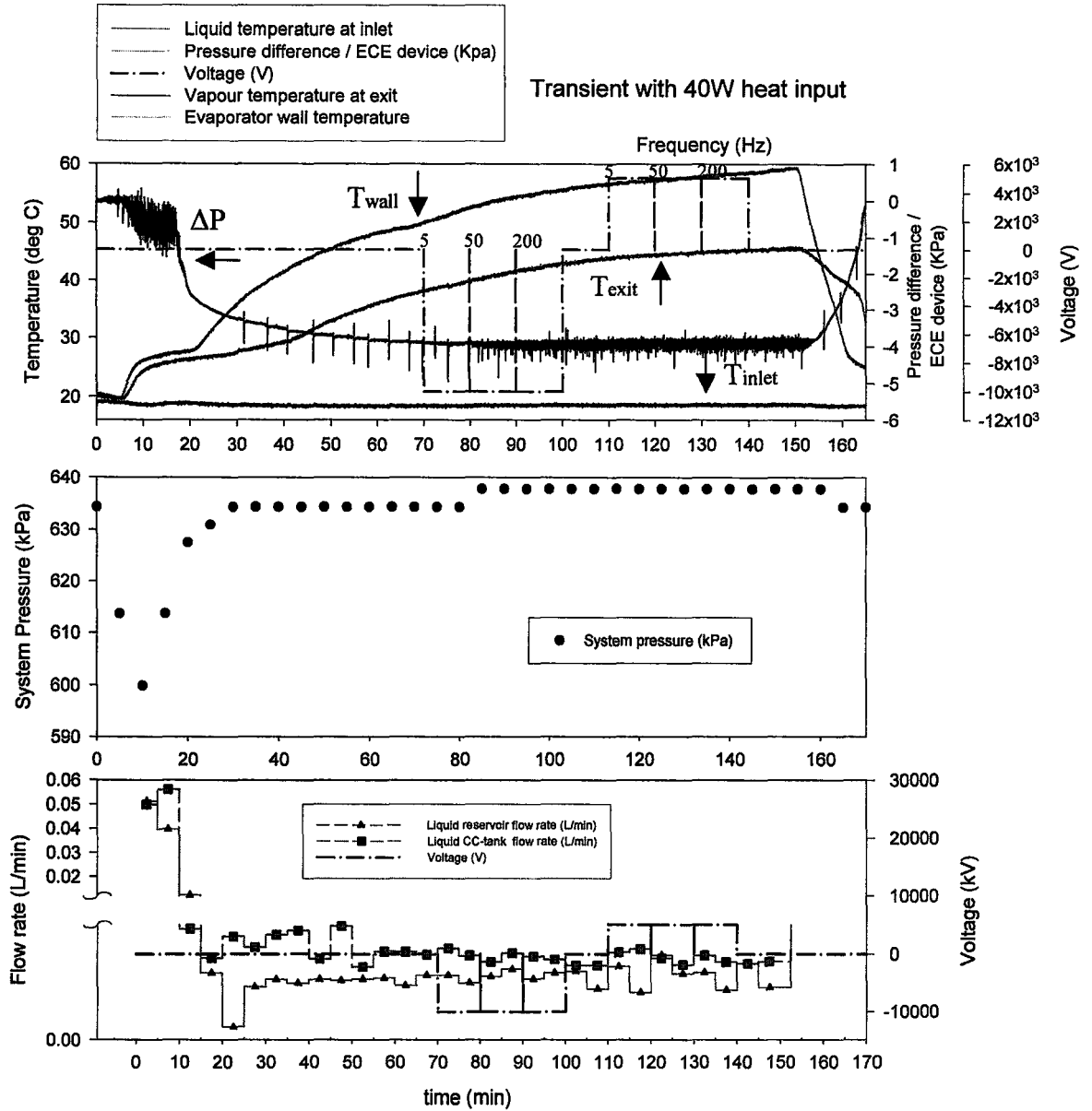


Figure A.14: Transient behaviour of liquid, vapour, wall-temperature and pressure difference /ECE device for EHD-ECE , system pressure, liquid and liquid reservoir flow rates for water cooling on condensate collection tank for heat input=40W at applied pulse voltage

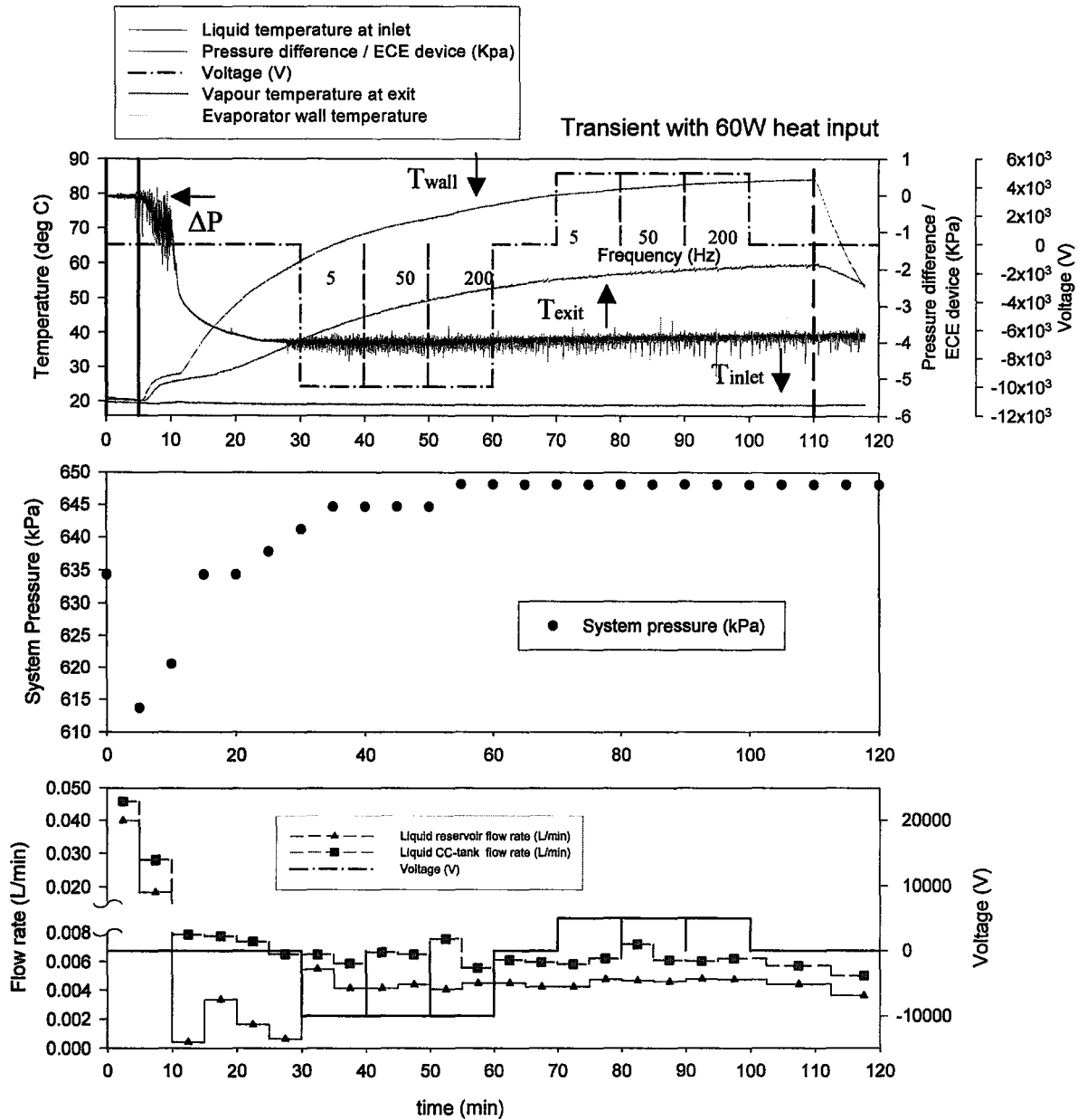


Figure A.16: Transient behaviour of liquid, vapour, wall-temperature and pressure difference /ECE device for EHD-ECE , system pressure, liquid and liquid reservoir flow rates for water cooling on condensate collection tank for heat input=60W at applied pulse voltage

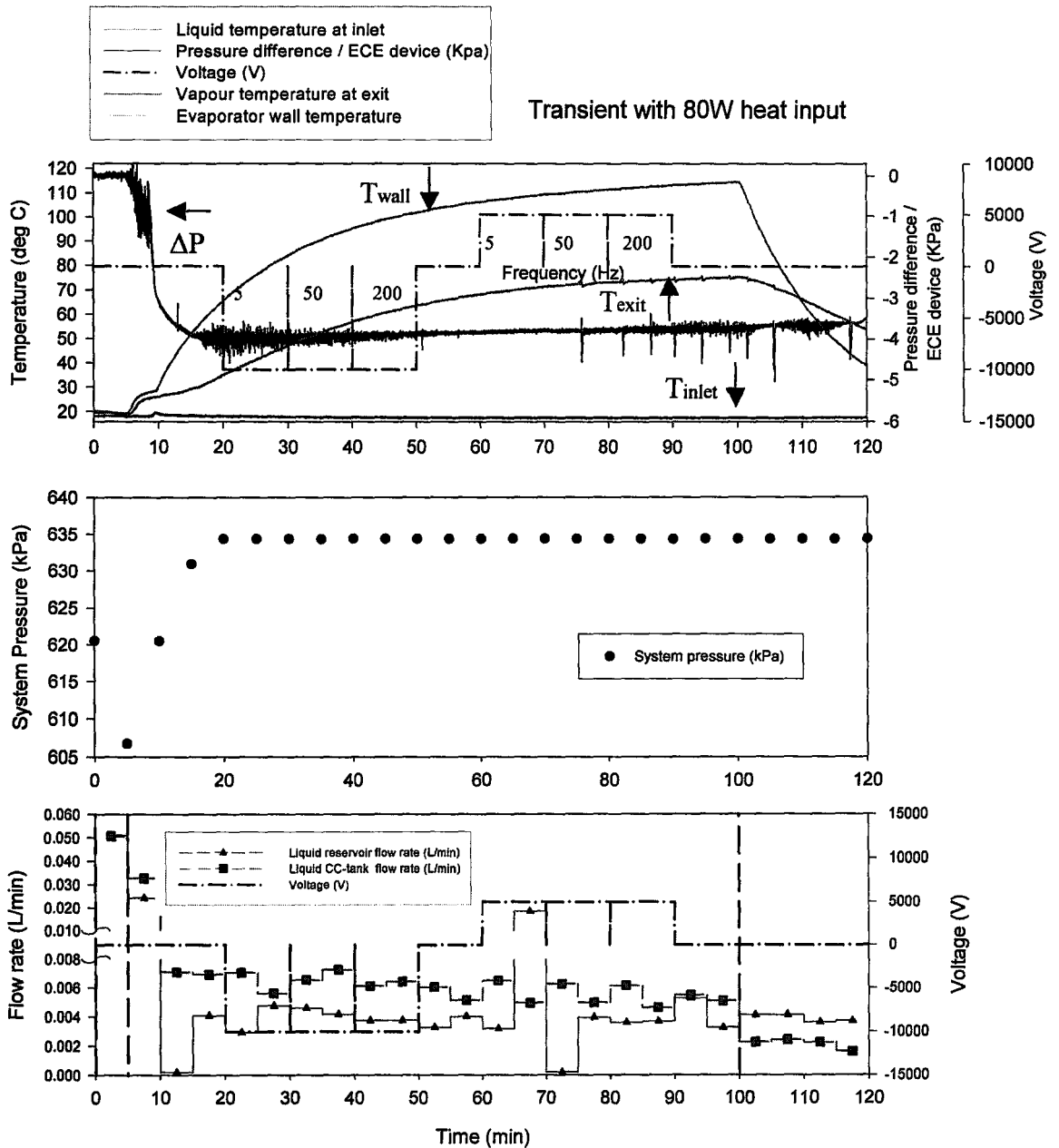


Figure A.17: Transient behaviour of liquid, vapour, wall-temperature and pressure difference /ECE device for EHD-ECE , system pressure, liquid and liquid reservoir flow rates for water cooling on condensate collection tank for heat input=80W at applied pulse voltage

APPENDIX B

Current-voltage characteristics

The dc voltage was measured at the electrode before the reactor and the current was measured at the ground section of the evaporator. The current-voltage test for negative dc voltage is shown in Figure B.1. Current of $3\mu\text{A}$ is measured at an applied voltage of -11kV . Therefore a maximum of -10kV is applied since the occurrence of breakdown or conduction current can deteriorate Freon. The same principle is used for the positive applied dc voltage as shown in Figure B.2 where current is measured at 6kV , and hence a maximum of 5kV is used in the experiment.

The pulse voltage was measured at the input of the reactor as the same way as the dc voltage case; however the pulse current was measure at this same point before the reactor. A typical pulse voltage waveform is shown in Figure B.3 for a 50Hz frequency and the corresponding pulse current is shown in Figure B.4. The product of this waveform is the power waveform as shown in Figure B.5. The power waveform shows reflection in the power and therefore it is necessary to analyze the pulse current waveform (Figure B.4) to measure the actual current across the electrode. The area under the current waveform gives a value of $I = 0.14\mu\text{A}$ is actually being applied to the reactor, which is an insignificant amount of current, compared with the large initial rise. Therefore it is assumed that no current is measured across the electrodes.

Unfortunately matching the impedance of the CE is difficult since the capacitance if the design is unknown and difficult to measure. The capacitance needs to be measured

in the working conditions in order to match the impedance, and this is difficult due to the presence of high voltage. Therefore it is necessary to experiment with different capacitor matching and analyze how the efficiency of the CE reacts. The main objective is to reduce feedback from the load as this will reduce efficiency as has been discussed in chapter 4.

APPENDIX B

B.1: Current-voltage characteristics applied dc voltage.

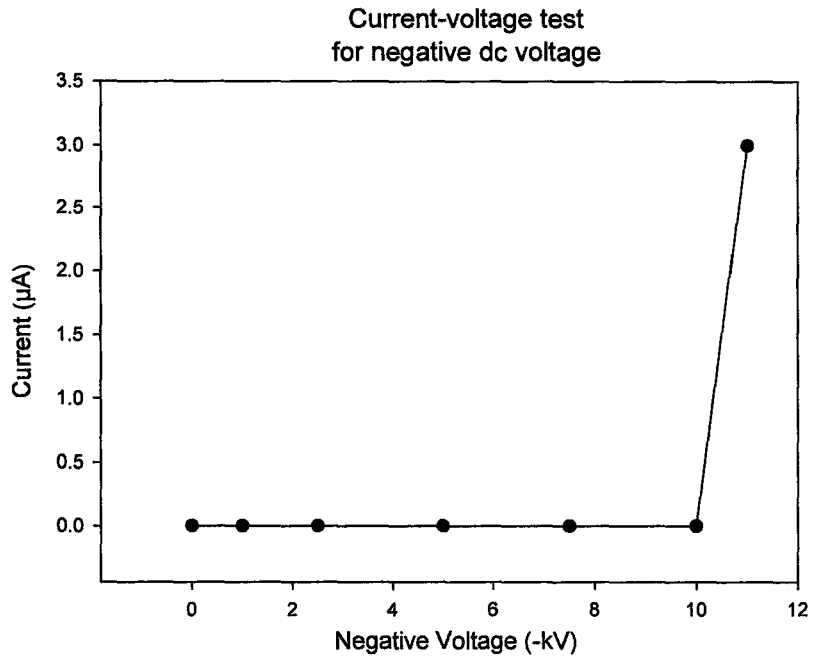


Figure B.1: Current-voltage characteristics with negative dc voltage.

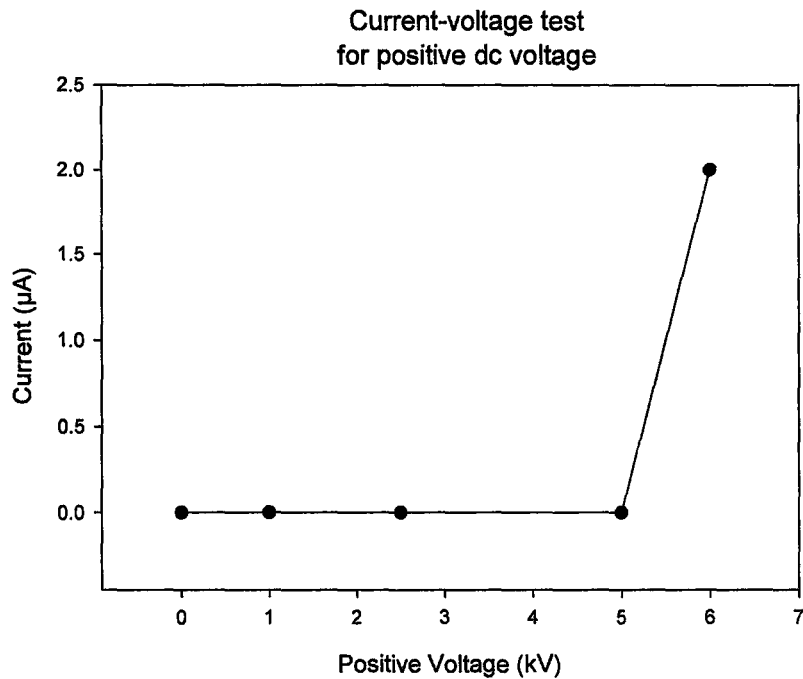


Figure B.2: Current-voltage characteristics with positive dc voltage.

B.2: Typical pulse waveform for EHD-ECE

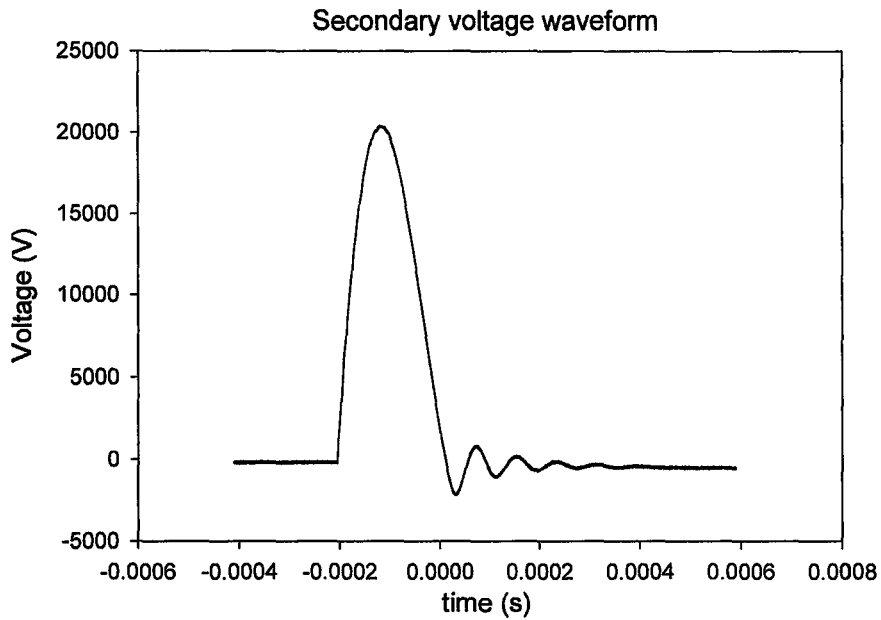


Figure B3: Typical secondary voltage waveform for 50Hz applied for EHD-ECE.

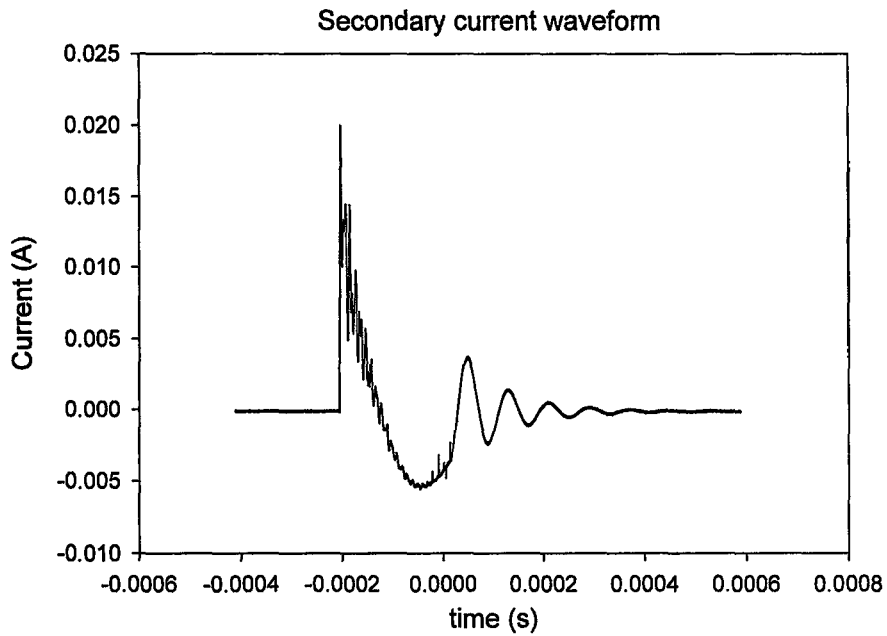


Figure B4: Typical secondary current waveform for 50Hz applied for EHD-ECE.

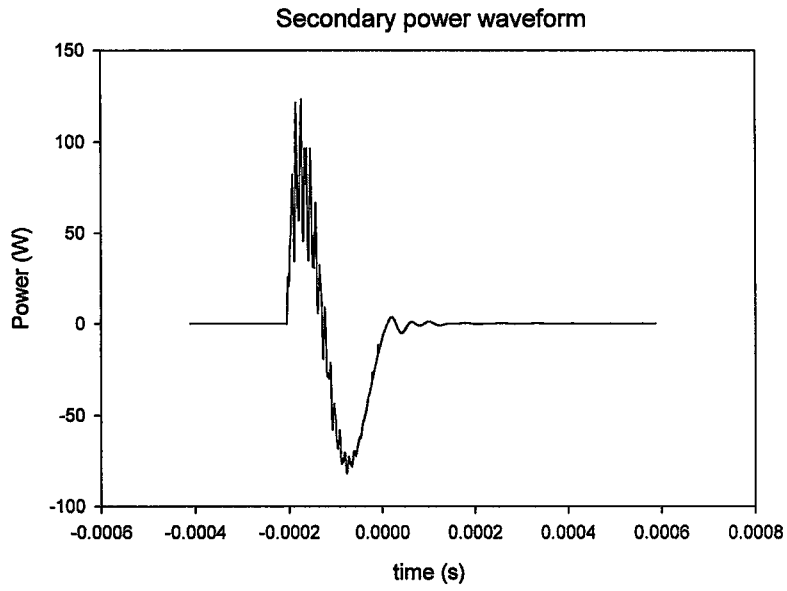


Figure B5: Typical secondary power waveform for 50Hz applied for EHD-ECE..

APPENDIX C

Modelling of electric field inside the CE and evaluation of dimensionless parameters

In this section, the two dimensional electric field distribution inside EHD-CE is calculated by COMSOL 3.2 which uses the finite element method to calculate the electric field strength inside the capillary evaporator for different regions as shown by the cross sectional view in Figure C1. The electrode is located in the center and has a potential of 5kV for dc voltage as shown by Figure C1, where a potential distribution of 20kV for pulse voltage is not shown. The fluid around the electrode is the liquid refrigerant of $\epsilon_l = 9.5$ and has a Polyethylene wick of $\epsilon_w = 4$ which surround it. The outside body is grounded aluminum housing with the vapour grooves as shown. For both cases of dc and pulse voltage the wick is assumed fully wetted and two cases are shown, one with no vapour bubble present at the fin-wick interface and another with a vapour bubble at the interface.

The analytical calculation of electric field distribution is based on the Poisson's equation:

$$\nabla \cdot E = \frac{1}{\epsilon} \rho_{ie} \quad \text{C.1}$$

where the electric field vector is defined as:

$$E = -\nabla V \quad \text{C.2}$$

Combining equations C.1 and C.2 fields:

$$\nabla \cdot \nabla V = \nabla^2 V = -\frac{1}{\epsilon} \rho_{ie} \quad \text{C.3}$$

For the fluid under consideration, HFC-134a, it is reasonable to suggest there is no net space charge and there is insufficient time for a surface charge to establish on the liquid-vapour interface. Hence, the right side of equation C.3 is negligible and the result is the Laplace's equation as follows:

$$\nabla^2 V = 0 \quad \text{C.4}$$

The boundary conditions at an interface between dielectric materials are required and may be determined by considering a plane boundary between regions of different dielectric constants ϵ_1 and ϵ_2 . These interfacial boundary conditions are:

- The normal component of the electric displacement vector, \mathbf{D} , is the same on each side of the boundary.

$$\begin{aligned} D_{n1} &= D_{n2} \\ \epsilon_1 E_{n1} &= \epsilon_2 E_{n2} \end{aligned} \quad \text{C.5}$$

- The component of the electric field, \mathbf{E} , tangent to the boundary is the same on each side of the boundary.

$$E_{t1} = E_{t2} \quad \text{C.6}$$

Due to the symmetry of the evaporator, it is assumed that the electric field intersects the interface normally at all radial positions. By applying this principle and specifying the different dielectric constants of the liquid, wick, and vapour, the electrical potential and radial electric field distribution were calculated.

In order to understand the physics of what is occurring inside the CE, the dimensionless values discussed in chapter 3 will be calculated in this section. In order to calculate the desired dimensionless values, the electric field inside the CE will be modelled using COMSOL 3.2. Figure C1 shows the cross sectional view of the electrical potential distributed inside CE. The electrode is located at the center and has a potential of 5kV, surrounding the electrode is liquid refrigerant with dielectric constant $\epsilon_l = 9.5$. This is the same model used for the pulse voltage of 20kV and therefore not shown. The wick surrounds the liquid and makes contact with the fins of the ground metal. The dielectric constant of the wick, assumed to be fully wetted is $\epsilon_w = 13.5$, which is the sum of the wicks dielectric constant and the liquid refrigerant. The occurrence of vapour bubble at the fin-wick interface is shown in the direction A. Three directions of A, B and C are shown and electric field strength will be calculated radially across the different materials with corresponding dielectric constants. Direction A starts at the electrode, the electric field strength is modeled radial across the liquid refrigerant, wetted wick, vapour and then grounded. Direction B starts at the electrode, radial across liquid refrigerant, wetted wick, vapour channel then grounded. Direction C again starts at the electrode, then the liquid refrigerant, wetted wick and then ground.

The radial electric field distribution is shown in figure C2 for direction A. The electric field starts with the highest value at the electrode, where a logarithmic decrease as it is distributed radial across the CE. Special interest is given to the change in material, resulting in change of dielectric constants and the reason for the change in the electric field distribution as shown in C2. At the liquid-wick interface, the electric field decreases

due to the addition of the wicks dielectric constant. The electric field increases at vapour interface since the dielectric constant is reduced. After the vapour bubble, the electric field goes to zero due to grounding the outside metal.

Figure C3 shows the electric field distribution in the direction of B. The electric field reduces radially again and reduces once more due to the wetted wick, then increases at the wick vapour channel interface.

Figure C4 shows the electric field strength in direction of C. The electric field is reduced at the wick-liquid interface and is then grounded at the metal.

Due to the geometry of the aluminum body and the presence of the fins, the electrical potential is not distributed evenly in the radial direction. Therefore there is some gradient effect present where the stronger electric field is presented in direction B since ground is further away.

Based on these jump conditions of the electric field, the dimensionless values are calculated for the different interfaces for both dc and pulse voltage as shown in Table C1.

The EHD number, Masuda number and the Electrostriction number as discussed in chapter 3 are calculated for the liquid phase, gas-liquid interface and the gas phase for both dc and pulse voltage. The Grashof number and the capillary force is also calculated where the capillary force is for wick pore sizes of $20\mu\text{m}$ and assumed that the meniscus is concave as shown by Wulz and Mayinge (1993) as $\theta \approx 30^\circ - 45^\circ$.

Due to the absence of current across the electrodes, the Ehd number is zero and the electrophoretic term is not a factor. Analyzing the dimension numbers for the liquid,

gas and gas-liquid interface, the largest value is the Masuda number in the gas-liquid interface for both dc and pulse voltage. This suggests that the dielectrophoretic term acting on the vapour bubble will have the largest external force occurring and is the dominating term in the force equation discussed in Chapter 3. This external force impacting on the vapour bubble may be the reason for the flow enhancement since the removal of this vapour from the wick-fin interface may allow a higher evaporation rate. Since the Ehd number is insignificant in our work, and then it can be assumed that polarity should not be a factor since both the dielectrophoretic and the electrostrictive force contain the electric field squared. This is supported by enhancement percentage, since there is not a significant difference due to polarity. However as discussed in Chapter 5, the magnitude of the voltage matters as can be seen from the experimental results and now can be supported by the present modeling. The larger the voltage applied results in a greater electric field strength and therefore larger dimensionless values as demonstrated by Table C1 comparing 5kV dc to 20kV pulse voltage. The slight influence of the positive and negative applied voltage polarity on the EHD enhanced flow rate can be explained by the temperature environment differences for each experiment where the Electrostriction number was influenced.

APPENDIX C

C.1: Modelling of electric field inside the CE and evaluation of dimensionless parameters.

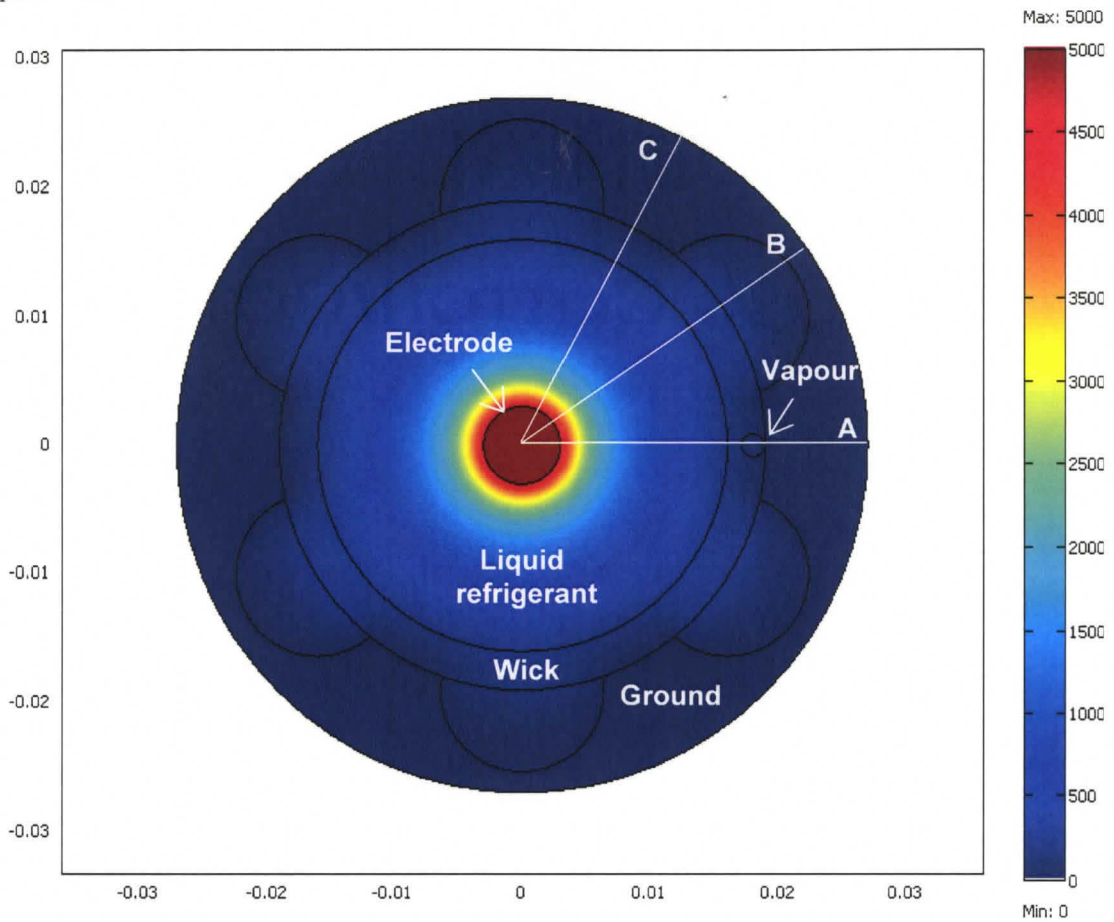


Figure C1: Cross section of evaporator with electrical potential distribution of 5kV.

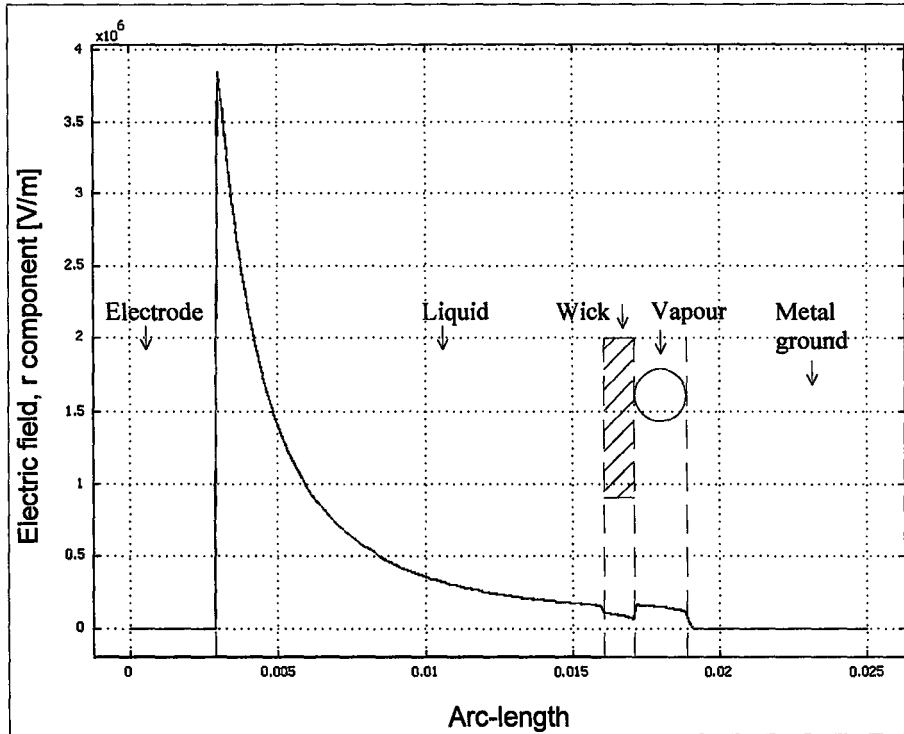


Figure C2: Electric field value in radial component in direction A with vapour.

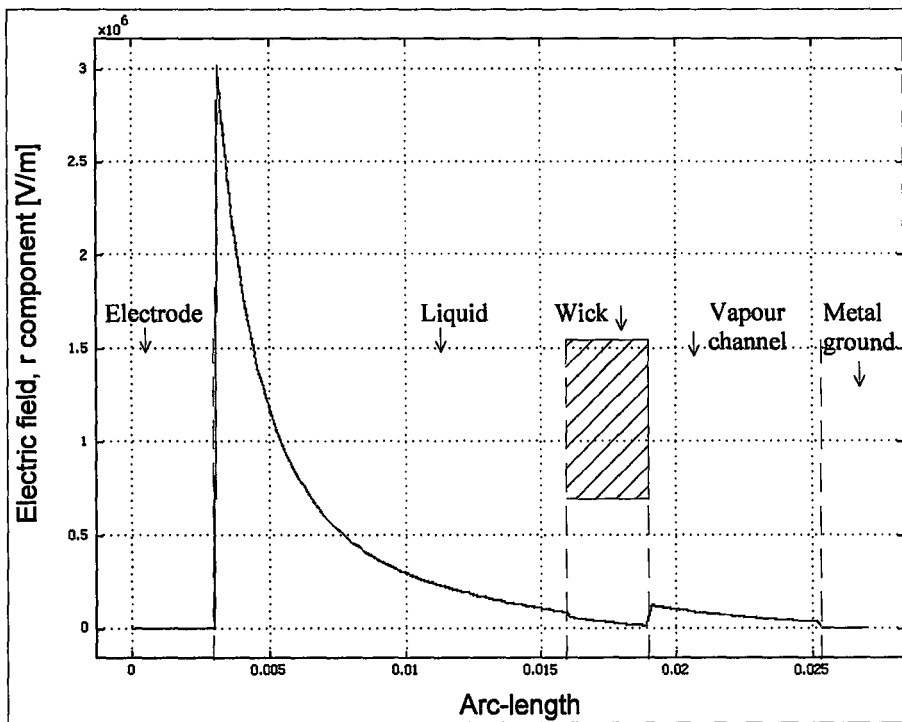


Figure C3: Electric field value in radial component in direction B.

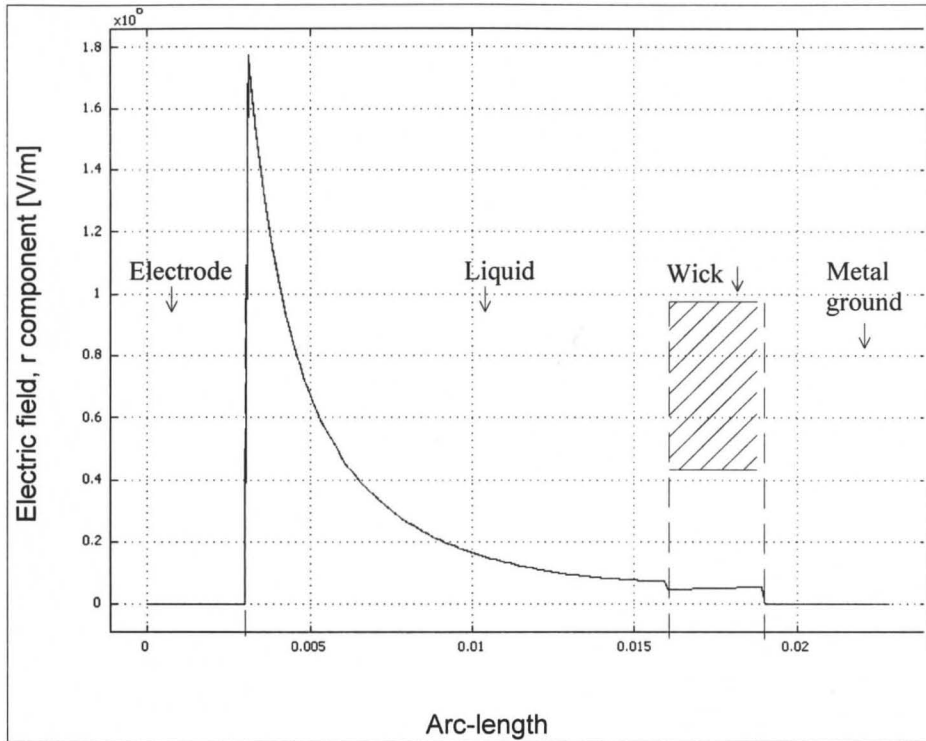


Figure C4: Electric field value in radial component in direction C.

Table C1: Typical dimensionless numbers.

Dimensionless numbers		Dc voltage $V_p=5kV$	Pulse voltage $V_{max}=20kV$
Liquid phase	E_{hd_l}	0	0
	Md_l	4.13×10^1	7.70×10^2
	Es_l	6.58×10^1	1.30×10^3
Gas-liquid interface	Md_i	4.73×10^3	7.57×10^4
Gas phase	E_{hd_g}	0	0
	Md_g	3.22×10^0	5.16×10^3
	Es_g	3.80×10^{-1}	5.74×10^2
Natural convection	Gr_g	1.28×10^6	1.16×10^6
Capillary force	B_o	$5.26 \times 10^1 - 3.96 \times 10^1$	$5.26 \times 10^1 - 3.96 \times 10^1$